Fatigue Loading and Design Methodology for High-Mast Lighting Towers

DETAILS

130 pages | 8.5 x 11 | PAPERBACK
ISBN 978-0-309-21403-2 | DOI 10.17226/22792

AUTHORS

Connor, Robert J.; Collicott, Steven H.; DeSchepper, Allen M.; Sherman, Ryan J.; and Ocampo, Jaime A.

NATIONAL COOPERATIVE HIGHWAY RESEARCH PROGRAM

NCHRP REPORT 718

Fatigue Loading and Design Methodology for High-Mast Lighting Towers

Robert J. Connor
Steven H. Collicott
Allen M. DeSchepper
Ryan J. Sherman
Jaime A. Ocampo
PURDUE UNIVERSITY
West Lafayette, IN

Subscriber Categories
Highways • Bridges and Other Structures

Research sponsored by the American Association of State Highway and Transportation Officials
in cooperation with the Federal Highway Administration

TRANSPORTATION RESEARCH BOARD

WASHINGTON, D.C.
2012
www.TRB.org

NATIONAL COOPERATIVE HIGHWAY RESEARCH PROGRAM

Systematic, well-designed research provides the most effective approach to the solution of many problems facing highway administrators and engineers. Often, highway problems are of local interest and can best be studied by highway departments individually or in cooperation with their state universities and others. However, the accelerating growth of highway transportation develops increasingly complex problems of wide interest to highway authorities. These problems are best studied through a coordinated program of cooperative research.

In recognition of these needs, the highway administrators of the American Association of State Highway and Transportation Officials initiated in 1962 an objective national highway research program employing modern scientific techniques. This program is supported on a continuing basis by funds from participating member states of the Association and it receives the full cooperation and support of the Federal Highway Administration, United States Department of Transportation.

The Transportation Research Board of the National Academies was requested by the Association to administer the research program because of the Board's recognized objectivity and understanding of modern research practices. The Board is uniquely suited for this purpose as it maintains an extensive committee structure from which authorities on any highway transportation subject may be drawn; it possesses avenues of communications and cooperation with federal, state and local governmental agencies, universities, and industry; its relationship to the National Research Council is an insurance of objectivity; it maintains a full-time research correlation staff of specialists in highway transportation matters to bring the findings of research directly to those who are in a position to use them.

The program is developed on the basis of research needs identified by chief administrators of the highway and transportation departments and by committees of AASHTO. Each year, specific areas of research needs to be included in the program are proposed to the National Research Council and the Board by the American Association of State Highway and Transportation Officials. Research projects to fulfill these needs are defined by the Board, and qualified research agencies are selected from those that have submitted proposals. Administration and surveillance of research contracts are the responsibilities of the National Research Council and the Transportation Research Board.

The needs for highway research are many, and the National Cooperative Highway Research Program can make significant contributions to the solution of highway transportation problems of mutual concern to many responsible groups. The program, however, is intended to complement rather than to substitute for or duplicate other highway research programs.

NCHRP REPORT 718

Project 10-74
ISSN 0077-5614
ISBN 978-0-309-21403-2
Library of Congress Control Number 2012936822

COPYRIGHT INFORMATION

NOTICE

The project that is the subject of this report was a part of the National Cooperative Highway Research Program, conducted by the Transportation Research Board with the approval of the Governing Board of the National Research Council.

The members of the technical panel selected to monitor this project and to review this report were chosen for their special competencies and with regard for appropriate balance. The report was reviewed by the technical panel and accepted for publication according to procedures established and overseen by the Transportation Research Board and approved by the Governing Board of the National Research Council.

The opinions and conclusions expressed or implied in this report are those of the researchers who performed the research and are not necessarily those of the Transportation Research Board, the National Research Council, or the program sponsors.

The Transportation Research Board of the National Academies, the National Research Council, and the sponsors of the National Cooperative Highway Research Program do not endorse products or manufacturers. Trade or manufacturers' names appear herein solely because they are considered essential to the object of the report.

Published reports of the

NATIONAL COOPERATIVE HIGHWAY RESEARCH PROGRAM

are available from:

Transportation Research Board
Business Office
500 Fifth Street, NW
Washington, DC 20001

and can be ordered through the Internet at:

http://www.national-academies.org/trb/bookstore

Printed in the United States of America

THE NATIONAL ACADEMIES

Advisers to the Nation on Science, Engineering, and Medicine

The **National Academy of Sciences** is a private, nonprofit, self-perpetuating society of distinguished scholars engaged in scientific and engineering research, dedicated to the furtherance of science and technology and to their use for the general welfare. On the authority of the charter granted to it by the Congress in 1863, the Academy has a mandate that requires it to advise the federal government on scientific and technical matters. Dr. Ralph J. Cicerone is president of the National Academy of Sciences.

The **National Academy of Engineering** was established in 1964, under the charter of the National Academy of Sciences, as a parallel organization of outstanding engineers. It is autonomous in its administration and in the selection of its members, sharing with the National Academy of Sciences the responsibility for advising the federal government. The National Academy of Engineering also sponsors engineering programs aimed at meeting national needs, encourages education and research, and recognizes the superior achievements of engineers. Dr. Charles M. Vest is president of the National Academy of Engineering.

The **Institute of Medicine** was established in 1970 by the National Academy of Sciences to secure the services of eminent members of appropriate professions in the examination of policy matters pertaining to the health of the public. The Institute acts under the responsibility given to the National Academy of Sciences by its congressional charter to be an adviser to the federal government and, on its own initiative, to identify issues of medical care, research, and education. Dr. Harvey V. Fineberg is president of the Institute of Medicine.

The **National Research Council** was organized by the National Academy of Sciences in 1916 to associate the broad community of science and technology with the Academy's purposes of furthering knowledge and advising the federal government. Functioning in accordance with general policies determined by the Academy, the Council has become the principal operating agency of both the National Academy of Sciences and the National Academy of Engineering in providing services to the government, the public, and the scientific and engineering communities. The Council is administered jointly by both Academies and the Institute of Medicine. Dr. Ralph J. Cicerone and Dr. Charles M. Vest are chair and vice chair, respectively, of the National Research Council.

The **Transportation Research Board** is one of six major divisions of the National Research Council. The mission of the Transportation Research Board is to provide leadership in transportation innovation and progress through research and information exchange, conducted within a setting that is objective, interdisciplinary, and multimodal. The Board's varied activities annually engage about 7,000 engineers, scientists, and other transportation researchers and practitioners from the public and private sectors and academia, all of whom contribute their expertise in the public interest. The program is supported by state transportation departments, federal agencies including the component administrations of the U.S. Department of Transportation, and other organizations and individuals interested in the development of transportation. **www.TRB.org**

www.national-academies.org

COOPERATIVE RESEARCH PROGRAMS

CRP STAFF FOR NCHRP REPORT 718

Christopher W. Jenks, *Director, Cooperative Research Programs*
Crawford F. Jencks, *Deputy Director, Cooperative Research Programs*
Waseem Dekelbab, *Senior Program Officer*
Danna Powell, *Senior Program Assistant*
Eileen P. Delaney, *Director of Publications*
Hilary Freer, *Senior Editor*

NCHRP PROJECT 10-74 PANEL

Field of Materials and Construction—Area of Specifications, Procedures, and Practices

Gregg C. Fredrick, *Wyoming DOT, Cheyenne, WY (Chair)*
Ahmad Abu-Hawash, *Iowa DOT, Ames, IA*
Fouad H. Fouad, *University of Alabama – Birmingham, Birmingham, AL*
Carl J. Macchietto, *Valmont Industries, Inc., Valley, NE*
Christopher E. Meyer, *Kansas DOT, Topeka, KS*
Justin M. Ocel, *FHWA, McLean, VA*
Andre V. Pavlov, *Florida DOT, Tallahassee, FL*
Bryan Spangler, *Michael Baker Jr. Inc., Harrisburg, PA*
Scott J. Walton, *Lower Colorado River Authority, Austin, TX*
Gary Moss, *FHWA Liaison*
Stephen F. Maher, *TRB Liaison*

AUTHOR ACKNOWLEDGMENTS

The research documented in this report was performed under NCHRP Project 10-74 by the School of Civil and Environmental Engineering at Purdue University in West Lafayette, Indiana. Purdue University is the prime contractor for this study with Dr. Robert J. Connor, associate professor of civil engineering at Purdue, as the project director and principal investigator. The co-principal investigator of this report is Dr. Steven H. Collicott from the School of Aeronautics and Astronautics at Purdue University.

The other authors of this report are Allen M. DeSchepper, research assistant at the School of Civil Engineering at Purdue University, Ryan J. Sherman, research engineer at the Bowen Laboratory for Large-Scale Civil Engineering Research at Purdue University, and Jaime A. Ocampo, research assistant at the School of Aeronautics and Astronautics at Purdue University. Special thanks are extended to Joe Mueller, field and lab engineering technician at the Bowen Laboratory, for his assistance in implementing the field monitoring program.

FOREWORD

By Waseem Dekelbab
Staff Officer
Transportation Research Board

This report provides criteria for the fatigue design of high-mast lighting towers (HMLTs). The report also includes a series of proposed revisions with associated commentary to the fatigue design provisions of the *AASHTO Standard Specifications for Structural Supports for Highway Signs, Luminaires, and Traffic Signals*. In addition, to ensure the fatigue design provisions are properly implemented into practice, design examples are also provided. The material in this report will be of immediate interest to highway design engineers.

Failures of high-mast lighting towers (HMLTs) in several states have raised questions as to the robustness and safety of the existing inventory of these structures. Fatigue failures have occurred at the base plate-to-column weld, handhole detail, and anchor rods. Several of the failed poles had been in service for less than 5 years. Based on field observations and forensic analysis of high-mast lighting poles, it is believed that wind-induced vibrations have a significant influence on the fatigue life. Neither the magnitude of the loads or the frequency of the application is understood. The current AASHTO specification does not adequately address these topics.

Research was performed under NCHRP Project 10-74 by Dr. Robert Connor, the School of Civil Engineering at Purdue University in West Lafayette, IN. The objectives of NCHRP Project 10-74 were to develop (1) loading and analysis criteria for use in the fatigue design of high-mast lighting towers, (2) a design method and proposed specifications for high-mast lighting towers, and (3) design examples. These research objectives were achieved by laboratory testing to investigate the effects of wind gusts (i.e., buffeting), vortex shedding, and associated dynamic oscillations; and a long-term field monitoring study gathered wind and strain gage data from eleven different HMLTs over the course of 2 years. Fourteen additional HMLTs were tested to determine their dynamic properties. Additionally, wind tunnel tests were completed to examine flow separation and wake characteristics of various multi-sided, tapered, tube geometries.

A number of deliverables are provided as appendices. Only Appendix A—HMLT Fatigue Design Examples and Appendix B—Proposed Specification and Commentary are published herein. Other appendices are not published but are available on the TRB website and can be found by searching on the title of the report. These appendices are titled as follows:

- APPENDIX C—Stress Range Histogram Data and Regression
- APPENDIX D—Wind Rosettes for Percent Occurrence and Mean Wind Speed
- APPENDIX E—Site Specific Instrumentation Plans
- APPENDIX F—Across Wind Excitation Algorithm
- APPENDIX G— HMLT Modal Frequency Algorithm
- APPENDIX H—HMLT Fatigue Life Evaluation
- APPENDIX I—Aerodynamic Pressure and Hotwire Data

CONTENTS

1 Summary

2 **Chapter 1** Background
2 1.1 Problem Statement
2 1.2 Objectives
3 1.3 Notes and Nomenclature

4 **Chapter 2** Research Approach
4 2.1 Field Monitoring Program
10 2.2 Aerodynamic Testing Program
15 2.3 Factors Affecting Fatigue Loading of HMLTs
28 2.4 Fatigue Wind Load Methodology

34 **Chapter 3** Findings and Applications
34 3.1 Results of Field Tests
47 3.2 Results of Aerodynamic Tests
56 3.3 Development of Proposed Specification
64 3.4 Large-Amplitude Oscillation
65 3.5 Fatigue Life Evaluation of Existing HMLTs

70 **Chapter 4** Conclusions and Recommendations
70 4.1 Conclusions
71 4.2 Suggested Research

72 References

A-1 **Appendix A** HMLT Fatigue Design Examples

B-1 **Appendix B** Proposed Specification and Commentary

Note: Many of the photographs, figures, and tables in this report have been converted from color to grayscale for printing. The electronic version of the report (posted on the Web at www.trb.org) retains the color versions.

SUMMARY

Fatigue Loading and Design Methodology for High-Mast Lighting Towers

Recent failures of high-mast lighting towers (HMLTs) have raised questions about the robustness of the existing inventory of these structures. Safety of the motoring public is an obvious concern as many of the collapsed structures have fallen on, or near, the adjacent roadway. Fatigue failures have occurred at the baseplate-to-column weld, handhole detail, and anchor rods, with several of the failed structures being in service for less than 5 years. The goal of NCHRP Project 10-74 is to increase the reliability of HMLTs through investigation of wind-induced loads, resulting in the development of rational design criteria for fatigue design of HMLTs.

Long-term field monitoring was performed to evaluate the in-service response of HMLTs; specifically, the magnitude and frequency of wind-induced loads experienced by these structures. Data were collected from 11 HMLTs over the course of 2 years. Wind speed data and stress-range histogram data were compiled for each HMLT, forming the basis for the proposed fatigue design loads. The concept of a fatigue-limit-state load for infinite life design was investigated, and found to be appropriate. Extrapolating the histogram data for a typical 50-year lifetime shows the total number of load cycles accumulated will exceed the limiting number of cycles at the constant-amplitude fatigue limit for the most common HMLT fatigue details. In addition, the compiled stress-range histogram data do not differentiate between loads from wind gusts and vortex shedding; therefore, the concept of the combined wind effect is introduced. Combined wind effect considers both gusting and vortex shedding effects together, eliminating the need for separate computations for fatigue design loads.

The proposed fatigue design load incorporates the fatigue-limit-state load with new importance categories that consider consequence of failure. The fatigue-limit-state load corresponds to a static pressure-range load cycle with a 1:10,000 probability, the established endurance limit for steel. This concept is similar to the fatigue truck used for the Fatigue I limit state in the AASHTO LRFD Bridge Design Specifications, which is used for infinite fatigue life of bridges. A reasonable relationship between mean wind speed and fatigue load also is developed to increase the reliability of structures exposed to sustained wind speeds above the national average. The proposed importance categories intend to increase the reliability of structures whose failure poses a direct risk to the motoring public. In short, the recommended static-pressure range values for the fatigue design of HMLTs, in order of increasing reliability, are 5.8, 6.5, and 7.2 psf.

Other relevant findings presented in this report include: effects of vibration mitigation, which can significantly increase life or decrease effective load; dynamic properties of HMLTs, which may be useful for in-depth analysis; aerodynamic properties of the flow around multi-sided sections; and a proposed method for fatigue life evaluation of HMLTs.

CHAPTER 1

Background

1.1 Problem Statement

Although not often recognized as significant structures by the motoring public, ancillary highway structures, such as high-mast lighting towers (HMLTs), are important components of an efficient highway system. During extreme events, HMLTs greatly assist in ensuring safe travel for the public, which makes the robust performance of these structures over the long term critical for the smooth operation of traffic. Also, considering most HMLTs are located directly adjacent to high-volume highways, the impact a collapse presents to the safety of motorists is clear. Unfortunately, recent failures of these structures have raised questions as to the robustness and safety of the existing HMLT inventory.

In the majority of cases, failure has been the result of load-induced fatigue. Fatigue cracking and total collapse of HMLTs has occurred. The cracking observed is generally found at the baseplate-to-column weld, handhole detail, and anchor rods, although cracking of the anchor rods was found to be less prevalent. Field observations and forensic studies of the failed HMLTs have indicated wind-induced vibration as a significant factor in the fatigue life of these structures. Natural wind can produce significant stress cycles due to dynamic loads from wind gusts. More complex aeroelastic phenomena such as vortex shedding also are known to produce fatigue damage. Since neither the magnitude nor the frequency of application of the loads that induce fatigue damage in HMLTs was clearly understood, NCHRP Project 10-74 was initiated to define a fatigue loading for the safe design of these structures.

1.2 Objectives

The research program described herein was directed toward developing realistic and practical load models to be used for the fatigue design of HMLTs. Long-term field monitoring was performed to evaluate the magnitude and frequency of the loads experienced by these structures, as well as in-service response. Additionally, wind tunnel and dynamic field tests were combined to better understand the aerodynamic characteristics inherent to various HMLT sizes and shapes. Combining the magnitude and frequency of the loads with the associated aerodynamic properties for a given pole was then used to develop a realistic and rational load model for the fatigue design of HMLTs.

This report presents results from field, laboratory, and analytical studies that have been used to develop rational criteria to be used during the fatigue design of HMLTs. Additionally, to ensure the fatigue loading is properly implemented into practice, a design methodology and specification for inclusion into the AASHTO Standard Specifications for Structural Supports for Highway Signs, Luminaires, and Traffic Signals with associated commentary also was developed.

In summary, the primary objectives of NCHRP Project 10-74 were to use data collected through field testing, laboratory wind tunnel testing, and analytical studies to

1. Develop loading and analysis criteria for use in the fatigue design of HMLTs.
2. Develop a design methodology and specifications with associated commentary for HMLTs.
3. Prepare recommended revisions to the existing AASHTO Standard Specifications for Structural Supports for Highway Signs, Luminaries, and Traffic Signals.

The research team included Robert J. Connor from the School of Civil Engineering at Purdue University and Steven H. Collicott from the School of Aeronautics and Astronautics at Purdue University. Purdue University is the primary contractor with Dr. Connor as the principal investigator responsible for the project and Dr. Collicott as the co-principal investigator accountable for the wind tunnel testing portion of the study. Other members of the research team included Allen M. DeSchepper, research assistant at the School of Civil Engineering at Purdue University, Ryan J. Sherman, research engineer at the Bowen Laboratory for Large-Scale Civil Engineering Research at Purdue University, and Jaime A. Ocampo, research assistant at the School of Aeronautics and Astronautics at Purdue University.

1.3 Notes and Nomenclature

Throughout this report, "AASHTO Signs" is used to refer to the Standard Specifications for Structural Supports for Highway Signs, Luminaires and Traffic Signals (2009). Where the bridge code is referenced, it is referred to as "AASHTO LRFD Bridge Design Specifications," or simply "AASHTO Bridge Specifications," or "AASHTO LRFD." Furthermore, the writing in this report is generally consistent with the terms and nomenclature used in the AASHTO Standard Specifications for Structural Supports for Highway Signs, Luminaires and Traffic Signals. For example, the term *constant-amplitude fatigue limit* (CAFL) is used instead of *constant-amplitude fatigue threshold* (CAFT), which is used in the AASHTO Bridge Specifications. In addition, "HMLT" is used to refer to the supporting structure and luminaire collectively. The tapered, tubular, steel supporting structure is generally called the pole.

CHAPTER 2

Research Approach

2.1 Field Monitoring Program

An extensive field monitoring program was implemented to determine the in-service response of HMLTs. Prior to the research conducted herein, loads provided in the AASHTO Standard Specifications for Structural Supports for Highway Signs, Luminaires and Traffic Signals (2009), also referred to as AASHTO Signs, were based on results from *NCHRP Report 412,* which examined a wide range of support structures and a variety of wind loading phenomena. NCHRP Report 412 modeled the response of support structures using spectral analysis to simulate natural wind gusts and modal analysis to simulate vortex shedding (Kaczinski et al., 1998). The current study is fundamentally different in approach by using field-measured experimental data and focusing only on HMLTs.

Eleven HMLTs at eight different sites were included in a long-term field monitoring program to establish the in-service response of these structures. Further, data from two other HMLT monitoring programs in the state of Iowa also were used to support the findings from this study.

To estimate the response over the lifetime of the structures, the duration of monitoring lasted up to 2 years. Height of the HMLTs varied from 100 feet to 160 feet, which represents the majority of the general population. The taper rate of the supporting pole structures was approximately 0.14 inches per foot. (Previous editions of AASHTO Signs assumed this taper rate to be the minimum associated with disrupting the formation of organized vortices and thus preventing the vortex shedding lock-in effect from occurring.) The cross section of all monitored poles was multi-sided with the exception of one circular cross section. The multi-sided poles were 12-sided or 16-sided, dodecagonal or hexdecagonal, respectively. These are the most common cross sections that fabricators use for these types of structures.

In conjunction with long-term monitoring, 14 additional HMLTs were tested to determine their dynamic properties. A procedure called "pluck testing" was used to excite the HMLTs dynamically. These HMLTs had similar dimensional and geometric properties as the ones selected for long-term monitoring. Dynamic data obtained by plucking a series of poles during separate studies conducted by the authors for the Iowa DOT also were reviewed and incorporated.

2.1.1 Setup, Instrumentation, and Testing

2.1.1.1 Setup for Long-Term Monitoring

Instrumentation for long-term monitoring consisted of two types of sensors—strain gages to monitor the load effect, and an anemometer to monitor the wind effect acting on the HMLT. Each long-term setup included a data collection system, a wireless cellular modem for remote communication, and an independent power supply. Data for pluck tests were collected using similar data collection equipment. Appendix E (available on the TRB website) contains instrumentation

plans for each of the HMLTs monitored in this study. All strain gages used were Measurements Group Model LWK-06-W250B-350 excited at 10 volts. On-site data collection was accomplished using a 16-bit Campbell Scientific CR9000 Data Logger. On-board analog and digital filtering was performed using the CR9000's 9052 analog input cards. Sample rates varied between 100 Hz and 250 Hz. For long-term monitoring, a CR5000 16-bit data logger was used due to its low cost and low power draw. Sample rates varied during the long-term monitoring depending on the data collected, but were between 20 Hz and 50 Hz. The anemometer was produced by RM Young and was a Model 5103.

Strain gages were generally placed at two locations on the pole. The first set of strain gages was located at a minimum of 1.5 times the diameter of the pole above the handhole detail, typically about 6 feet above the baseplate. These strain gages recorded the nominal stress-range in the pole and were placed a sufficient distance above the handhole to avoid local stress concentration effects. These strain gages were equally spaced around the perimeter of the pole to associate the response of the HMLT with a particular wind direction. The second set of strain gages was located immediately above the baseplate to tube wall connection detail or adjacent to the handhole. The intent of these strain gages was to capture local stress effects at the primary fatigue detail(s) of the HMLT and this was for general information only. Hence, the data from these gages were not used to analyze the applied wind load effect because they were influenced by local effects. Since the global response of the pole was of interest, the "nominal" gages were used to determine the applied wind load. Thus, the detail-specific strain gages were omitted from a couple sites installed later in the long-term monitoring program. The typical instrumentation setup showing strain gage placement is illustrated in Figure 2.1.

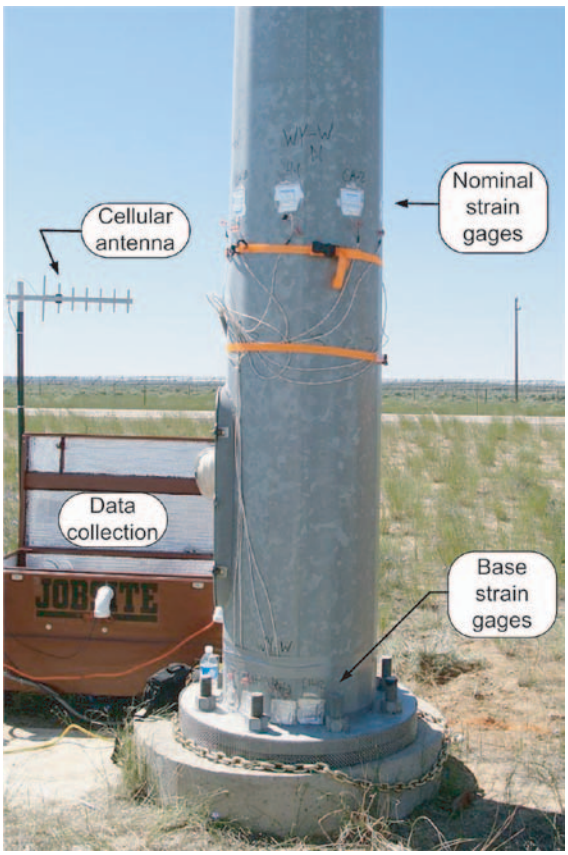

Figure 2.1. Strain gage placement and data collection system.

6 Fatigue Loading and Design Methodology for High-Mast Lighting Towers

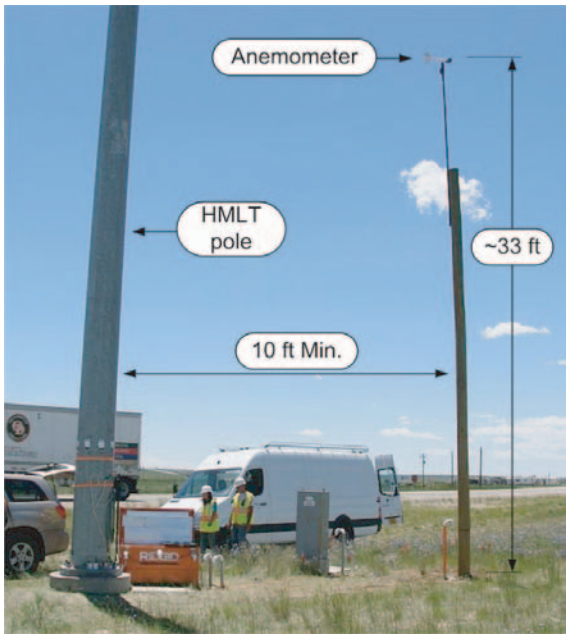

Figure 2.2. Anemometer placement.

The term "channel" is sometimes used in this report to refer to the data, or signal, recorded from a specific strain gage. This is done to be consistent with labeling practices in the field.

An anemometer was installed near each HMLT to capture wind speed and direction. Anemometers were placed approximately 33 feet (10 meters) above the ground, which is the standard for wind measuring instruments and is also the reference height for wind load computation used by ASCE and AASHTO. Generally, the anemometers were installed on a separate timber pole provided by the sponsoring agency. If a sponsoring agency could not provide a separate pole, the anemometer was attached to the HMLT using a bracket. However, a separate pole was preferred to avoid any influence of the HMLT on the airflow around the measuring instrument. When a separate pole was used, it was placed at least 10 feet away from the HMLT. The typical instrumentation setup showing the placement of the anemometer is illustrated in Figure 2.2.

2.1.1.2 Pluck Test Setup

The setup for pluck testing consisted of a cable and a "come-along" winch. One end was attached to the pole at a point approximately 30 feet from the ground, and the other end was attached to a stationary object, usually a truck hitch. A static load was applied to the structure using the come-along and then quickly released, exciting the structure much like a string is plucked on a musical instrument. A load cell was placed in-line with the cable and the load recorded with the strain data. Instrumentation for pluck testing consisted of two accelerometers placed parallel and orthogonal to the direction of the applied load. Accelerometers were manufactured by PCB Piezotronics, Inc., Model 3711D3FA3G. The action of plucking excites the pole into oscillation and data are recorded until the pole has damped out. The raw data collected from pluck tests are short-term; data collected from each pluck usually lasted less than 3 minutes.

2.1.2 Data Collection

Field-test data were collected, sorted, and stored for analysis as five different types: pluck test data, stress-range histogram data, wind data, ambient data, and triggered data. Pluck test data

were collected immediately on-site while the researchers were present. The remaining four types correspond to long-term monitoring and were collected remotely. Their description, collection method, and relevance are discussed below.

2.1.2.1 Pluck Test Data

Data from pluck tests were recorded from accelerometers, strain gages, or both, depending on whether the HMLT was set up for long-term monitoring or only for dynamic testing. Accelerometers were mounted both longitudinal and transverse to the plucking direction. Typically, each tower was plucked between two and four times so data could be compared for consistency and repeatability. In total, 25 HMLTs were pluck tested for dynamic properties (11 long-term monitored HMLTs and 14 other HMLTs). The data collected from both the accelerometers and strain gages were used to determine the natural frequencies and damping ratios of a given pole, and both types of data were analyzed using similar methods. Modal frequencies were extracted using either a cycle counting method or Fast Fourier Transform (FFT). Damping ratios were extracted using the log-decrement method.

2.1.2.2 Stress-Range Histogram Data

In fatigue analysis, stress-range (S_R) and cycle count (N) data provide the foundation for quantifying damage and can be collectively represented in a histogram. Stress-range histograms are derived from time-history data. However, the time-history data are not necessarily stored; the data logger continually buffers and processes the time-history data. From the processed time-history data, the histogram is made using a cycle counting method. Then, at defined intervals, the stress-range histogram data are saved to a file, and the buffer is reset. Storing all the time-history data would rapidly fill the data logger memory and be nearly impossible to transmit back to the data server using a cellular modem. This preprocessing saves significant research time and effort; the histogram data are much more compressed. The interval for this project was set to 10 minutes, which had been shown to be acceptable based on the research team's experience.

Cycle counting is the process through which stress time-history data are broken down into individual stress cycles and sorted into groups of similar magnitude. The cycle counting method used to create the stress-range histograms in this study was the rainflow counting method. Rainflow cycle counting is commonly used in fatigue analysis and is a listed procedure in ASTM Standard E 1049. The algorithm for rainflow counting is relatively simple and easily programmed into the data logger. Throughout this report, the term rainflow data is synonymous with stress-range histogram data. The process through which stress-range histogram data are collected and stored is shown in Figure 2.3.

2.1.2.3 Wind Data

Stochastic wind data were continuously recorded over the duration of the study. Three values for wind speed were recorded at 10-minute intervals—average speed, maximum recorded speed, and a sampled speed. Average direction and a sampled direction also were recorded for the same interval. These data are used to calculate the mean wind speed at each HMLT and to account for variability in the proposed fatigue loads. The stochastic data also are compiled in Appendix D (available on the TRB website) as directional rosettes for percent occurrence and mean wind speed. These rosettes were useful in evaluating the HMLT response with regard to wind direction.

In addition to the stochastic wind data, wind speed and direction were recorded in a continuous time-history for use with both the ambient and triggered data.

2.1.2.4 Ambient Data

Ambient data refers to recording both strain gage data and wind data in a continuous time-history in order to monitor ambient vibration, which is random vibration of an HMLT

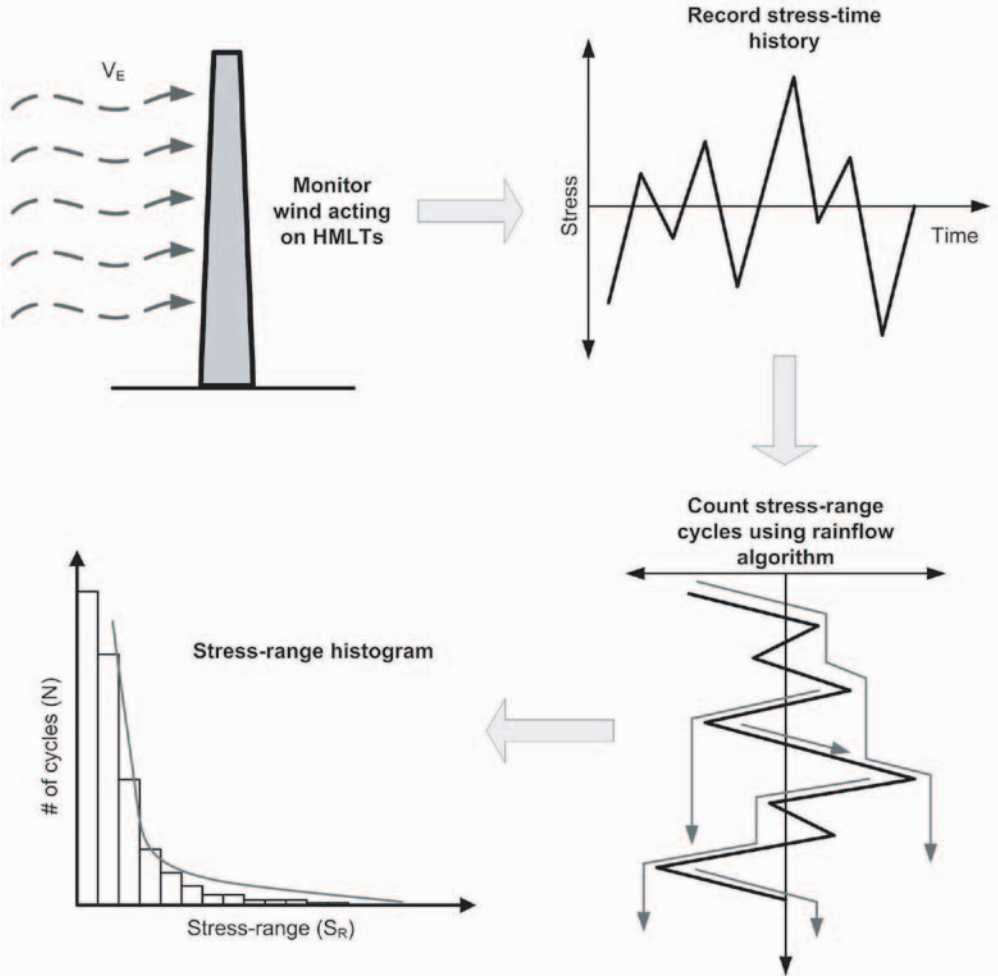

Figure 2.3. Stress-range histogram data collection.

excited by natural wind. Data of this type were recorded for each of the poles included in the long-term monitoring program. Ambient data were recorded for two different purposes—to determine dynamic properties based on wind excitation and to monitor across-wind excitation due to vortex-induced vibration. Data collected to study dynamic properties were completely random, whereas data collected to study across-wind excitation occurred during periods of low wind speed, typically between 2 and 14 miles per hour. Due to restrictions in computer memory and remote data retrieval, ambient data collection was limited to a few days every month until a sufficient amount of data were obtained.

2.1.2.5 Triggered Data

Triggered data refers to strain gage data and wind data recorded in a continuous time-history for periods of high wind speed. When the monitored wind speed reached a pivotal value, data collection was "triggered" to record. These triggers were typically set somewhere between 20 and 60 mph and stored in separate files accordingly. At sites with greater wind activity, the triggers were modified to record at higher wind speeds to keep the amount of data manageable. At sites with lesser wind activity, the triggers were set at lower wind speeds to ensure that a reasonable amount of data was collected. These data were used to monitor the response of the HMLTs during periods of high-velocity buffeting and to verify high stress-range cycles in the stress-range histogram data.

2.1.3 Overview of Sites

Several parameters were used to select specific locations for the field monitoring program. These parameters include historical data, agency survey data, and wind power generation data. Historical data were consulted to identify states that experienced cracking and collapse of HMLTs and to determine if these states were located in regions with high yearly mean wind velocity. The states also were surveyed to learn about the existing inventory, find any new instances of cracking or collapse, and to identify agencies willing to participate in the field monitoring program. Agency support was imperative for the success of the study. Supporting state agencies provided unique knowledge of site conditions and structure inventory, support during equipment installation, and assistance with maintenance during the monitoring period. Wind power generation data also were useful in pinpointing locations with consistent, high wind speeds. Areas with consistent wind speeds conducive to power generation also are susceptible to aeroelastic phenomena such as vortex-induced vibration.

A map showing the locations of the HMLTs selected for long-term monitoring is presented in Figure 2.4. Additionally, Table 2.1 provides a summary of the locations of all HMLTs in the field monitoring program, along with basic structure geometry.

Another critical factor for collecting data used to determine proposed fatigue loads was monitoring duration. A considerable amount of data is required to extrapolate a lifetime loading spectrum, especially for a random system such as wind loading; therefore, an initial goal of 18 to 24 months was set. Based on the research budget, eight HMLTs at six different sites were initially selected and installed during the spring and summer of 2009. These were located in California, North Dakota, Oklahoma, Pennsylvania, South Dakota, and Wyoming. Although the researchers were prepared for maintenance issues with sensors and data acquisition systems, of the eight HMLTs, the two in Oklahoma had to be abandoned after approximately 16 months.

Figure 2.4. Map of long-term monitoring HMLTs.

10 Fatigue Loading and Design Methodology for High-Mast Lighting Towers

Table 2.1. HMLT summary.

Long-Term Monitored HMLTs				
ID	**LOCATION**	**HT (ft)**	**# SIDES**	**DIA. (in)**
CA	Barstow, CA - I-15 & L St.	100	16	19.5
IA-N	Clear Lake, IA - I-35 & US-18 (North)	148	12	28.5
IA-S	Clear Lake, IA - I-35 & US-18 (South)	148	12	28.5
KS	Hays, KS - I-70 & Toulon Ave.	100	12	18
ND	Bismarck, ND - I-90, MP 156 WB	160	12	29
OK-NE	Henryetta, OK - I-40 & US-75 (Northeast)	130	16	22
OK-SW	Henryetta, OK - I-40 & US-75 (Southwest)	120	16	21.5
PA	Erie, PA - I-90 & I-79	110	R	21.5
SD	Rapid City, SD - US-16 & SD-44	150	16	26
WY-CJE	Creston Junction, WY - I-80 & WY789 (East)	120	16	24
WY-CJW	Creston Junction, WY - I-80 & WY789 (West)	120	16	24
Additional Plucked HMLTs				
ID	**LOCATION**	**HT (ft)**	**# SIDES**	**DIA. (in)**
ND-83	Bismarck, ND - I-94 & State St.	140	n/a	25
ND-94	Bismarck, ND - I-90, MP 156 WB	140	16	25
ND-EXP	Bismarck, ND - I-94 & Expy.	140	n/a	24
ND-MEM	Bismarck, ND – I-94 & Memorial	n/a	16	18
ND-SUN	Bismarck, ND - I-94 & Sunset Dr.	140	12	30
OK-E	Henryetta, OK - I-40 & US-75	120	12	22
OK-SE	Henryetta, OK - I-40 & US-75	130	16	22
PA-AD	Erie, PA - I-90 & I-79	110	R	18
SD-1E	Spearfish, SD - I-90, MP1 EB	120	16	21
SD-1W	Spearfish, SD - I-90, MP1 WB	120	16	21
SD-42E	Sturgis, SD - I-90, MP42 EB	100	16	19
SD-42W	Sturgis, SD - I-90, MP42 WB	80	16	17
WY-219E	Sinclair, WY - I-80, MP 219 EB	80	18	18
WY-219W	Sinclair, WY - I-80, MP 219 WB	120	18	26
WY-228W	Rawlins, WY - I-80, MP 228 WB	120	16	26

Notes: R – round (circular) pole
n/a – data not available

Preliminary data from the Pennsylvania HMLT indicated little wind activity, most likely related to local topographical effects. To better utilize the equipment and remaining time available, the site was relocated to Kansas in December 2009. In the spring of 2010, a review of the research budget showed that an additional site could be added to the program at no additional cost; thus, instrumentation was added to an HMLT in Iowa. The last HMLT was added after retrieving equipment from the Oklahoma site, and was installed on a second HMLT at the Iowa site. Table 2.2 lists the collection periods for each of the HMLTs. Data collection was not necessarily continuous over any period due to occasional equipment failure or power outages, as well as when changes to the logger programming were required.

2.2 Aerodynamic Testing Program

The aerodynamic testing was separated into two parts. The first was a computational fluid dynamics (CFD) study and the second, which was the bulk of the aerodynamic testing program, was done experimentally. Both of these approaches were implemented to study the pressure and

Table 2.2. Long-term data collection periods.

ID	START	END
OK-NE	April 10, 2009	Sept. 4, 2010
OK-SW	April 10, 2009	Sept. 14, 2010
PA	May 30, 2009	Nov. 10, 2009
ND	June 9, 2009	June 8, 2011
SD	June 18, 2009	May 24, 2011
WY-CJE	July 4, 2009	June 6, 2011
WY-CJW	July 4, 2009	June 6, 2011
CA	July 21, 2009	June 15, 2011
KS	Dec. 3, 2009	June 6, 2011
IA-N	July 14, 2010	June 9, 2011
IA-S	Dec. 22, 2010	June 9, 2011

velocity fields around the model. There are marked differences between both approaches. The CFD yields more points and helps visualize the flow; locations with low pressure or high velocity can be easily identified. For the experimental work, the velocity or pressure is only probed at points of interest. Using these results, the CFD models can be calibrated.

Pressure and velocity fields are examined at the surface and near wake of three types of tapered models (8-, 12-, and 16-sided models). By studying these two fields, the associated forces that act on the HMLT pole can be inferred and applied to the design of future HMLTs.

2.2.1 Wind Tunnel Testing

The wind tunnel testing section includes a view of the experiment setup and rationale for the different instruments and hardware used.

2.2.1.1 Oscillation Forcing Rig

The oscillation forcing rig was constructed to replicate the oscillatory movement of the HMLTs. The natural wind-forced movement in the wind tunnel is high frequency (16 Hz) but very low amplitude (<1 mm). It is hard to detect by eye but shows up on the hot-wire signals. The setup is constructed out of steel and aluminum. The base is made out of steel I-beams and square aluminum extrusions and has two steel ½-inch diameter rods that hold springs and linear bearings. The linear bearings are attached to a bar that holds an aluminum airfoil extrusion that holds the model mount. The model mount is made out of copper and has tapped bolt holes with 31 degrees between each hole (i.e., 0, 31, 62, 93, etc.). The model has holes every 30 degrees, so when the model is rotated 1 degree, one of the model holes lines up with the 31-degree mount hole. There are a total of three copper mounts that can be interchanged and each mount covers a different range. The first range covers degrees 0–10, the next covers 11–20 (starts at 11, then 42, 73, etc.), and the last covers 21–30 (starts at 21, then 52, 83, etc.). In this way, 30 degrees of travel is achieved in 1-degree increments. The models themselves are made of fiberglass foam-core, wood, and aluminum tubes to hold the model itself. A picture of the entire hardware setup can be seen in Figure 2.5.

2.2.1.2 Hot-Wire Anemometry

Hot-wire anemometry is the use of a very thin gold or tungsten wire (some being 30 times thinner than a human hair) to measure the wind speed at a certain probe point. A single hot wire can be used effectively to assess the wind velocity at a certain location. A hot wire works by keeping a constant temperature through a wire. As air flows past it, the wire cools and needs to draw more power to keep the wire at the same temperature. The hot wire is used as one of the resistances on

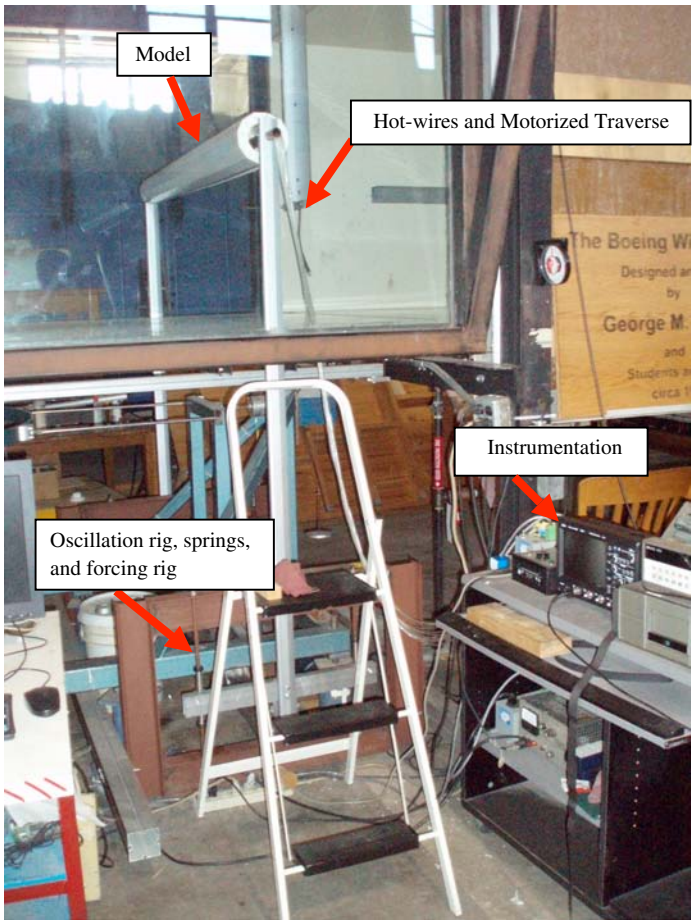

Figure 2.5. Wind tunnel instrumentation and hardware setup.

a Wheatstone Bridge such that as the hot wire requires more voltage, the change in voltage can be accurately measured using an oscilloscope or data acquisition card.

One hot-wire drawback is that it cannot tell which way the wind direction is moving, so flow in recirculation zones can be difficult to instrument. If two hot wires are placed in the same probe in perpendicular configuration, the device is then called an X-wire and it has a much more complicated setup and calibration procedure. However, an X-wire can be used for flow angularity, x-y flow direction (not downstream-upstream direction, however), and turbulence checks. In this report, single hot wires were used for all of the testing.

The hot wires were set at two different locations. The first was mounted on a moving motorized traverse that could be controlled through an RS-232 port and a LabView program. The second hot wire was set on a static stand and was used as a reference to check for shedding correlation between two different span-wise positions. Two different instrumentation setups were used, one early and one later. The early setup, as shown in Figure 2.6, used a Tektronix TDS50348 oscilloscope and a custom-made Bruhn electronics box. The second setup, as shown in Figure 2.7, used a LeCroy oscilloscope and an Intelligent Flow Analyzer (IFA) 100 for two hot wires used at the same time. No connection to the computer is necessary for data acquisition; the waveforms are captured and post-processed later to get the shedding frequency. The setup was changed for two reasons—the need to use two hot wires at the same time and the need for a more accurate pressure sensor.

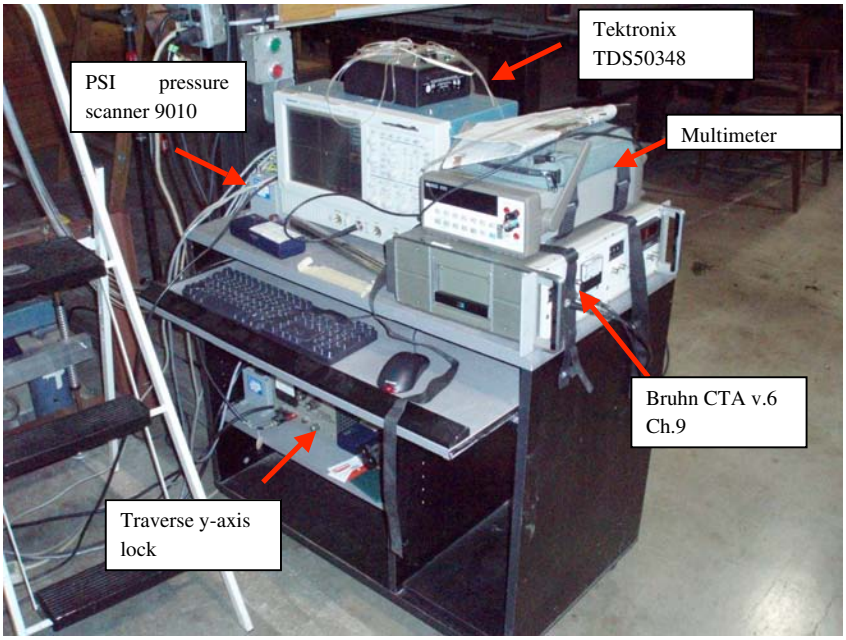

Figure 2.6. Early wind tunnel instrumentation setup.

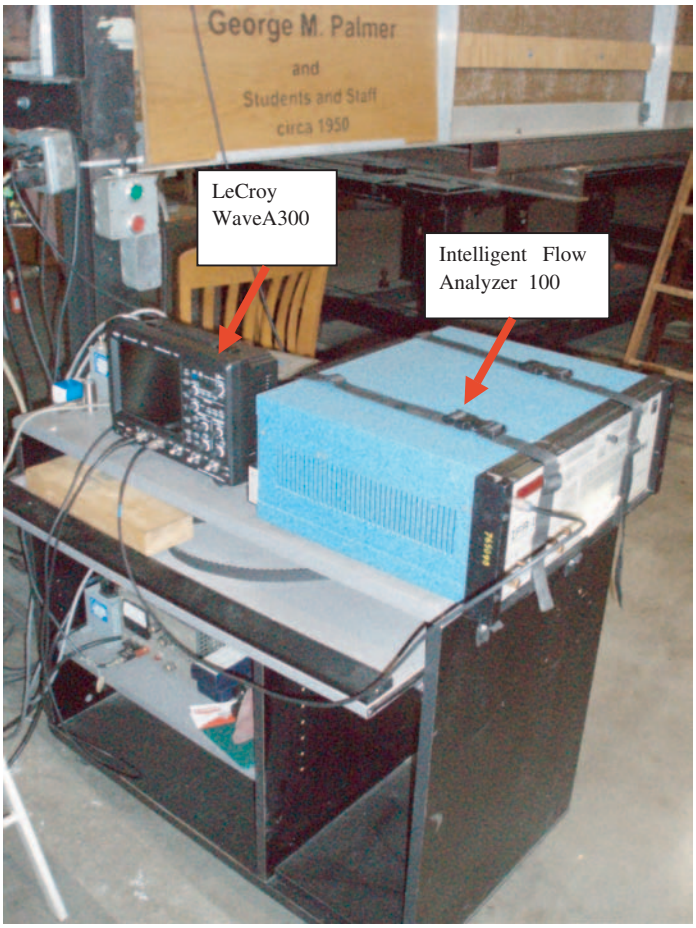

Figure 2.7. Later wind tunnel instrumentation setup.

14 Fatigue Loading and Design Methodology for High-Mast Lighting Towers

Figure 2.8. PSI-ESP 16HD pressure scanner (sensor).

2.2.1.3 Pressure Scanner

The other set of experimental data acquired used a pressure scanner. The early pressure scanner used was a Pressure Systems Inc. (PSI) 9010 that featured 20 inches of water (approximately ⅔ of a psi) and sampled at about 5 samples/channel/second with a total of 16 channels, of which 12 were used during testing. The pressure scanner was later changed to a PSI-ESP 16HD, as shown in Figure 2.8. This scanner has a sampling rate of 20,000 samples per second and a pressure range of 4 inches of water, providing much better resolution for testing.

The pressure scanner data aid in recreating the pressure fluctuations on the surface of the poles. From these pressure fluctuations, an empirical equation for the forces acting on the structure can be derived. Although the models are not a complete scaled model due to not being able to create an aeroelastically accurate wind tunnel replica, the current model can represent a section of the HMLT. The effects of the wind shedding vortex cells on tapered structures can be accurately studied this way.

2.2.1.4 Smoke Wand

The smoke wand was used as a check for the quantitative pressure and hot-wire data. It is composed of a pump, a kerosene tank filled with deodorized kerosene, a power supply, and a heating rod. The wand was placed upstream of the model, and the location of separation was identified. The smoke wand also was used to check where the separated shear layer would be located and the hot-wire probe was set at this location. Results from the smoke wand do not provide quantitative data, but they do provide qualitative information about the flow that can be correlated to the readings from the hot wire and pressure scanner.

2.2.2 Computational Fluid Dynamics

The computational fluid dynamics studies for this project focused on the pressures applied to the structure and were set to be a check against the experimental results. There were two pieces of software used—Cfdesign by Blue Ridge Numerics/Autodesk, and FLUENT from ANSYS.

2.2.2.1 FLUENT

The FLUENT CFD study was done during the design stage to look for potential trouble areas (separation, pressure fluctuations) to better assess pressure tap placement. As the testing started,

the smoke wand was used to check for the separation point, and the location was checked with the results obtained from the CFD velocity field.

2.2.2.2 Cfdesign

The Cfdesign study was done later in the experimentation process. This study was done as a check to see if it could reproduce the 3-D flow on a tapered structure. It was a new software program to experiment with, and was discontinued after some initial work so that it wouldn't detract from the experimental work already under way. The Cfdesign software had some problems with the taper—the software was smoothing it out—and did not seem to predict separation where the experiments showed.

2.3 Factors Affecting Fatigue Loading of HMLTs

2.3.1 Wind Characteristics—Buffeting and Vortex Shedding

Two types of wind-induced structural vibration have been identified as contributing to fatigue damage of HMLTs: buffeting due to wind gusts, and vortex shedding (Phares et al., 2007). Buffeting is the result of turbulence in the airstream upwind of the structure, which causes rapid changes in wind velocity. Whereas buffeting is characterized by behavior upwind of the structure and is associated with varying wind velocity, vortex shedding is characterized by behavior downwind of the structure and is associated with more consistent wind velocity. Vortex shedding, and associated vortex-induced vibration, occurs when alternating series of vortices are shed from the flow wake at a specific frequency, forming what is called the von Karman vortex street (Anderson, 2007; Liu, 1991). An example of the von Karman vortex street is shown in Figure 2.9.

2.3.1.1 Vortex Shedding

For a circular cylinder, the von Karman vortex street forms at a Reynolds number of about 40 (Edwards and Bingham, 1984). At this point, the vortex street is laminar and stable. As the Reynolds number increases to 300, the vortex street becomes turbulent; however, the shedding frequency remains regular. Here, the vortex shedding is turbulent yet coherent along a length of the cylinder. This type of vortex shedding originates from the flow becoming unstable; instead of having two attached vortices in the wake, the vortices are shed periodically. When each vortex is shed, it accelerates the flow on the opposite side of the pole while slowing the flow on the side that creates the vortex (Ruscheweyh, 1996). The accelerations, in turn, create alternating areas of low pressure that drive the wake structure back and forth creating periodic loads on the poles. These periodic loads are of great interest in the fatigue-tolerant design of HMLTs. The turbulent flow continues

Figure 2.9. Picture of von Karman vortex street (Anderson, 2007).

16 Fatigue Loading and Design Methodology for High-Mast Lighting Towers

up to Reynolds numbers of 3×10^5, where the wake becomes disorganized and vortex shedding becomes random. In terms of wind speed, vortex shedding of HMLTs can be expected to occur at wind velocities less than 30 mph as shown in Equation 2.1. Since vortex shedding is contingent upon steady flow upstream of the body, and natural wind is rarely steady at velocities of that magnitude, vortex shedding of HMLTs typically occurs at wind speeds even lower than 30 mph.

$$Given, R_e \cong \frac{9400vD}{ft \cdot mph}. \quad For\ D = 1\ ft, \quad v = \frac{3 \times 10^5 \left(ft \cdot mph \right)}{9400\left(1\ ft\right)} \approx 30\ mph$$

Equation 2.1: Reynolds number solved for velocity

One may wonder why there is such an interest in describing the wake when the loads on the poles are conceptualized by air pressure at the surface of the pole. It is important to note that there is some viscous, or "skin friction" drag, but on a blunt body such as a pole, the pressure drag dominates over the skin friction. The wake, or more specifically, the structure of the flow in the wake, is a result of the flow separation process, including any unsteadiness in the separation process. As such, the structure of the wake is an easily viewed symptom of the important aerodynamic events occurring at the surface of the pole. A highly periodic wake implies a highly periodic pressure loading on the pole. Therefore, the wake structure is critical for understanding the effects of vortex shedding.

Vortex shedding frequency can be estimated using the non-dimensionalized Strouhal relation. The Strouhal relation solved for the frequency at which vortex shedding will occur is shown in Equation 2.2.

$$f_s = \frac{SV}{D}$$

Equation 2.2: Strouhal relation (Kaczinski et al., 1998)

where S is the Strouhal number, V is the wind velocity, and D is the diameter of the pole.

The Strouhal number of a circular cylinder has been compiled extensively and equals 0.20 (Every et al., 1982). As the "roundness" of the section decreases so does the Strouhal number. For multi-sided sections typically used for HMLTs, the Strouhal number decreases to 0.18 to 0.15, and for square or rectangular sections the Strouhal number may be as low as 0.11.

Occasionally, the structure may resonate at the same frequency as the frequency of vortex shedding, creating an aeroelastic effect. This is where the structure deflects and alters the flow field with its back-and-forth rocking. Motion of this type can lock the vortex shedding into a resonant frequency of the structure. Resonate vibration is called "lock-in" and has been observed by a number of researchers (Burt and LeBlanc, 1974; Edwards and Bingham, 1984; Every et al., 1982; Krauthammer et al., 1987; Phares et al., 2007; Vickery et al., 1983). Vortex shedding at a lock-in condition is "fixed" at a certain frequency for a range of velocities as shown in Figure 2.10.

Locking-in to a range of velocities means that small fluctuations in wind speed or pole diameter do not alter the frequency of the vortex shedding and therefore results in continued resonance. If the lock-in or aeroelastic effect causes the amplitude of vibration to increase, then aeroelastic instability, or negative damping, occurs. Negative damping may have a considerable effect on the fatigue life of an HMLT by increasing the stress-range associated with each vortex shedding cycle.

Figure 2.10 assumes a constant cross section, meaning the Reynolds number only changes with velocity. However, with a tapered pole such as an HMLT, the Reynolds number varies with both diameter (i.e., position along the pole) and velocity. Therefore, diameter changes in a uniform wind also may be subject to vortex shedding lock-in, thereby creating a larger periodic loading

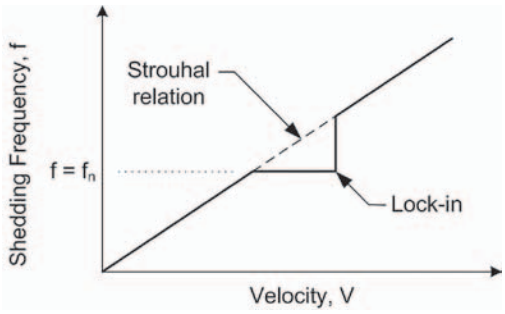

Figure 2.10. Lock-in phenomenon.

than without lock-in. The length of the pole over which lock-in occurs is also a matter of study since it is required to accurately predict the movement of the structure.

The behavior of HMLTs subject to vortex shedding is characterized by an across-wind response. The nature of alternating pressures in the wake causes the motion to be orthogonal to the direction of the wind. Based on the results of this study and the results of Connor and Hodgson (2006), this response is generally limited to the second mode of vibration and, to a lesser extent, the third mode.

2.3.1.2 Buffeting

Buffeting is the result of changes in wind velocity and direction. Buffeting does not have constant velocity and may result from free-stream turbulence due to meteorological phenomena or have instabilities from upstream obstacles such as vortex shedding with other bluff bodies or ground surface roughness. Buffeting inherently has a wide range of velocities that apply pressure to a structure and induce vibration. In other words, buffeting is not limited to high wind speeds, and can occur whenever turbulence exists in the wind stream. Vibrations due to buffeting have variable amplitudes contrary to the behavior of vortex shedding, which is more steady state.

Buffeting vibration is the vibration produced by turbulence or other disturbances of the flow not generated by the vibrating object itself (Liu, 1991). Unlike vortex shedding, buffeting is mostly aerodynamic in nature, that is, there is no aeroelastic response. Therefore, changing the stiffness or damping of a structure will not necessarily change the fatigue loading due to buffeting. Previous studies have shown such vibrations occur primarily in the first mode for HMLTs and are responsible for the upper-limit stress-range cycles; however, the upper-limit stress-range cycles may not significantly contribute to fatigue damage (Phares et al., 2007).

In addition to a response in the first modal frequency, the behavior of HMLTs subject to buffeting is characterized by an along-wind response. In other words, the motion of the HMLT excited by buffeting causes the structure to move parallel with the wind. This may be visualized in the traditional sense of wind pressure acting on the frontal area of the structure.

2.3.1.3 Combined Wind Effect

The current AASHTO Standard Specifications for Structural Supports for Highway Signs, Luminaires and Traffic Signals (2009) considers vortex shedding and buffeting as independent fatigue loads. However, these two load effects rarely act independently of each other. Both along-wind behavior, indicative of buffeting, and across-wind behavior, indicative of vortex shedding, can be observed acting together. It is difficult to separate the two effects using field-measured data. Where vortex shedding is effectively mitigated, a direct comparison of the two load effects is made; however, this approach is somewhat limited by the amount of data collected. A clearer picture

18 Fatigue Loading and Design Methodology for High-Mast Lighting Towers

forms when the entire wind loading spectrum is examined. For this reason, the proposed fatigue load effect (developed herein) is arrived at using a combined wind effect, which includes both buffeting and vortex shedding.

2.3.2 Dynamic Properties

2.3.2.1 Modal Frequencies

The following two methods were implemented to extract modal frequencies from field-measured data:

1. Cycle counting in the time domain and
2. Peak picking in the frequency domain.

Peak picking was performed first using pluck data and served as a quick way to extract the frequency values. These values were then verified using a cycle counting method. Modal frequency values were later computed to a greater degree of accuracy using ambient data, if available. In addition to examining field data, computational methods were examined for estimating modal frequencies. The computational methods include closed-form solutions such as those currently found in AASHTO Signs, a multiple degree-of-freedom eigenvalue solution using discretized beam elements, and finite element analysis.

To extract the natural frequencies from the acceleration and strain gage data obtained during pluck tests, a fast Fourier transform (FFT) was performed. An FFT is a mathematical algorithm that converts raw data recorded in the time domain to the frequency domain. Once the FFT has been executed, the natural frequencies can be determined by "peak picking." Simply, the peaks from the resulting FFT plot are recorded as the natural frequencies. Figure 2.11 shows sample accelerometer data from a pluck test. Note, for this research, only the first four modes of vibration were of interest. Typically, it was found that the accelerometers captured the higher frequencies better than the lower frequencies, whereas the strain gages better captured the lower frequencies. Data from the long-term poles include both accelerometer and strain gage data, while data from the other plucked poles consist solely of accelerometer data. Both accelerometer data and strain gage data, if available, were used to calculate natural frequencies and damping ratios.

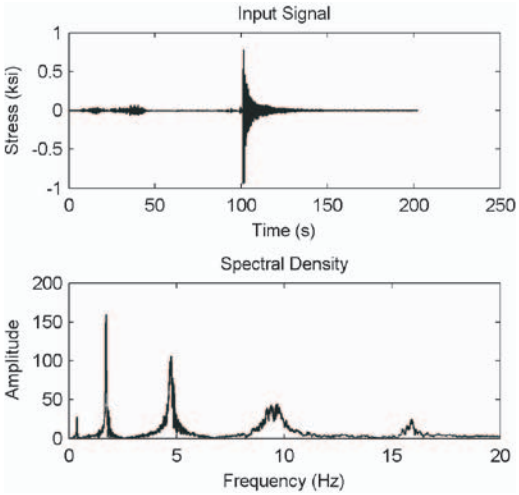

Figure 2.11. Sample pluck data—time domain and frequency domain.

After extracting the modal frequencies using the peak picking method, they were verified using cycle counting. The original time-domain signal was filtered using a relatively wide passband about the frequencies determined from peak picking. (This filtering process was essential for calculating damping ratios using the log-decrement method discussed in the following section.) Then, the number of cycles in the signal were counted and divided by the amount of time elapsed. This proved to be a simple and effective means of checking the initial values.

2.3.2.2 Damping Ratios

The following two methods were implemented to extract damping ratios from field-measured data:

1. Log-decrement in the time domain and
2. Half-power bandwidth in the frequency domain.

The half-power bandwidth method could only be used on the long-term monitored poles where ambient data could be collected. The log-decrement method was used on all poles using pluck test data.

Pluck test time-history data, or time-domain signals, are composed of sinusoidal components of each mode of vibration excited by the pluck test. To use the log-decrement method, the individual modes must be isolated from the others as well as any surrounding noise. This is done by subjecting the raw signal to a filter that removes frequencies outside of the modal frequency passbands, leaving a decay profile for the mode of interest. Knowing the modal frequencies obtained from the FFT and peak picking methods, passbands can be established for each mode. Examples of original and filtered pluck test signals are shown in Figure 2.12.

After the signals are filtered for each mode of interest, a mathematical algorithm isolates the positive and negative peaks and then scans the series of peaks for a period of steady decay. From

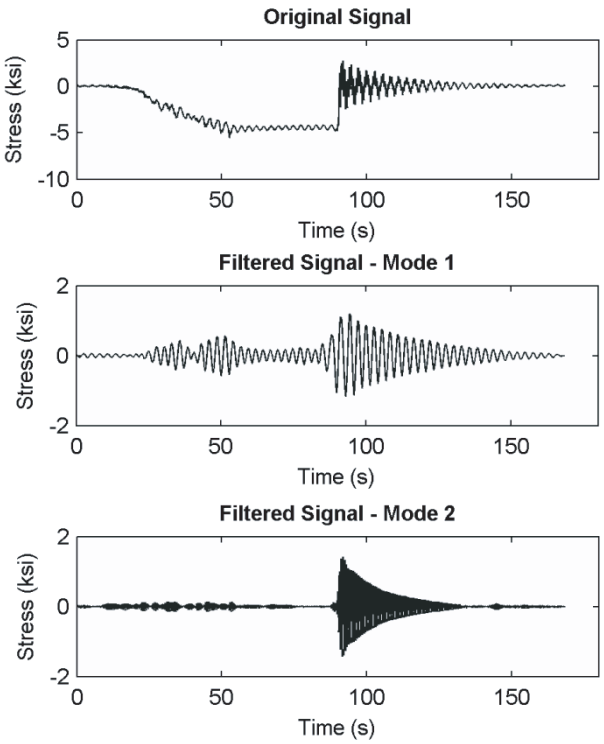

Figure 2.12. Signal filtering.

20 Fatigue Loading and Design Methodology for High-Mast Lighting Towers

this decay period, a graph of the natural log of the ratio of successive peaks versus number of cycles is plotted. The graph follows a liner relationship according to Equation 2.3.

$$\ln\left(\frac{v_1}{v_n}\right) = \delta n$$

Equation 2.3: Log-decrement

where v_1 is the initial peak value, v_n is the value of any successive peak, and n is the cycle number. The log decrement, δ, is equal to the slope of this line. To determine the slope, a best-fit line is applied to the plot using a linear least-squares regression, and Equation 2.3 may be rewritten in terms of relative peaks as shown in Equation 2.4.

$$\delta = \ln\left(\frac{v_n}{v_{n+1}}\right)$$

Equation 2.4: Log-decrement in terms of relative peaks

An example of a best-fit line using typical data collected during this research is shown in Figure 2.13. The damping ratio, ξ, can then be calculated using Equation 2.5.

$$\xi = \frac{\delta}{\sqrt{4\pi^2 + \delta^2}}$$

Equation 2.5: Damping ratio

Using ambient data, frequency response curves were created for each of the HMLTs. Damping ratios could then be calculated from the frequency response curves by the half-power bandwidth method. Frequency response curves are typically created by subjecting a given system to a forced vibration and measuring the response amplitude for a range of known forcing frequencies. The response amplitude can then be plotted against the forcing frequency to create a curve in the frequency domain. Damping ratios also can be obtained from ambient time-history data. For ambient data, the forced vibration is the result of random natural wind and the response is recorded as strain in the time domain. To create the frequency response curve, the ambient data must be converted to the frequency domain using an FFT. This was done by subdividing the ambient data into suites, passing each suite through an FFT, and averaging the suites together

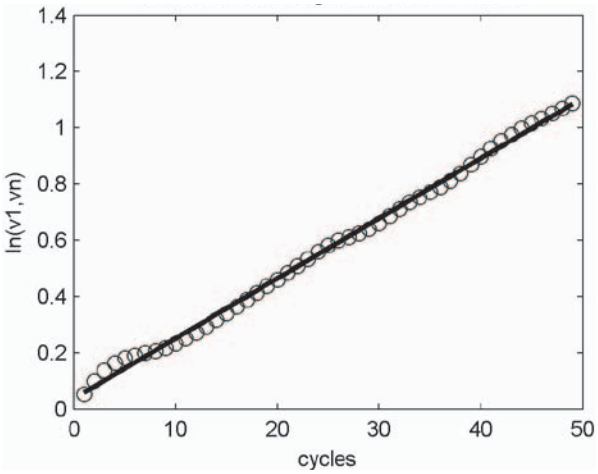

Figure 2.13. Best-fit line for log-decrement calculation (Mode 2).

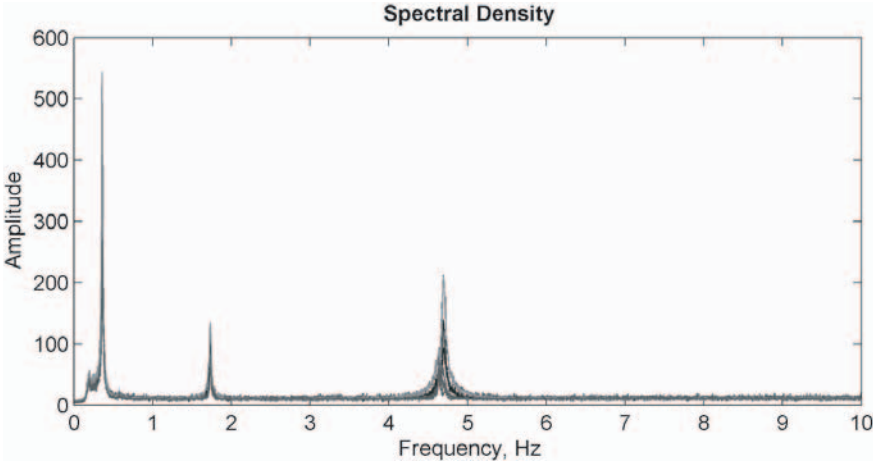

Figure 2.14. Example of frequency response curve from ambient data.

to create a high-resolution frequency response curve. An example of a curve generated from ambient data is shown in Figure 2.14.

Damping ratios were then calculated using the half-power bandwidth method. From the frequency response curve, a modal frequency is isolated and its peak value is established. Then half-power points are determined on either side of the peak where the curve equals the peak value divided by the root of 2. An illustration of the half-power points is given in Figure 2.15. Frequencies f_1 and f_2 at the half-power points then can be used to calculate the damping ratio using Equation 2.6.

$$\xi = \frac{f_2 - f_1}{f_1 + f_2}$$

Equation 2.6: Damping ratio using half-power bandwidth method

Modal frequencies also can be calculated using Equation 2.7.

$$f = \frac{f_1 + f_2}{2}$$

Equation 2.7: Modal frequency using half-power bandwidth method

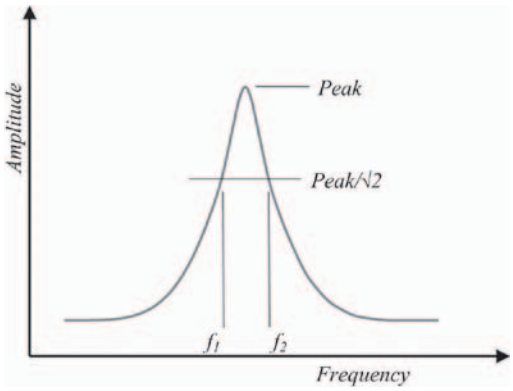

Figure 2.15. Definition of points for half-power bandwidth method.

Calculating modal frequencies using the response curve shown above results in a higher level of accuracy than if obtained using peak picking and pluck data. This is because the ambient data stream is much larger and a higher number of FFT points may be used, resulting in a higher resolution frequency spectrum. This method was used as an additional check of modal frequencies mentioned above.

It is well established that there are numerous methods to calculate the damping ratio of a given structure, and the two methods used above often yielded different results for the same structure, sometimes with considerable scatter. For instance, it is common for structures to respond differently to different types of dynamic excitation. Plucking excites the HMLT by displacement at a certain location along its height, while ambient excitation is due to natural effects such as wind gusts or vortex shedding. In addition to differences due to excitation, different sources of damping may affect the results. For example, aerodynamic or negative damping most likely was not present during pluck tests; the action of the test itself likely mitigated any response due to vortex shedding. Damping values calculated using the log-decrement method and pluck data refer to structural damping. In contrast, it is likely that aerodynamic damping was included in the ambient data collected. In summary, the damping values listed in this study most likely include contributions from both structural and aerodynamic damping, and scatter does exist.

The half-power method used in conjunction with ambient wind data is more consistent with the objectives of this study. Ambient excitation by wind is the *true* source of cyclic stress leading to fatigue damage. Plucking is a valuable tool for retrieving dynamic data since it can be done quickly and does not require any long-term equipment; however, it is not a natural source of excitation or fatigue stress to the HMLTs. The half-power bandwidth method is also the preferred method of computing damping ratios according to ASTM E756 (1998)—Standard Test Method for Measuring Vibration-Dampening Properties of Materials. The standard states that other computational methods may be used provided results are consistent with half-power bandwidth.

2.3.3 HMLT Geometry—Luminaire Area and Pole Cross Section

According to AASHTO Signs, the wind load effect applied to a support structure is a function of two basic parameters—projected area and static wind pressure. The projected area is the area of the structure projected on a vertical plane in any given direction and is directly proportional to wind load. Two separate elements exist for HMLTs where the frontal area must be considered—the pole and the luminaire. The area of the pole is relatively straightforward, but the area of the luminaire is somewhat subjective and is typically given in terms of an effective projected area (EPA). The static wind pressure is a modified form of the Bernoulli equation and is a function of wind velocity, drag coefficient, and other factors. Drag coefficient is of particular importance since it varies for different shapes and Reynolds numbers. The EPA of the luminaire is assumed to include the drag coefficient, so this is no concern to the designer when calculating loads on the luminaire; however, the drag coefficient must be considered for the pole.

The luminaires for the HMLTs monitored in this study vary dramatically. (For the remainder of this discussion, "luminaire" will refer to the group of lighting elements and their supporting upper-works, and the individual lighting elements will be referred to as "lights.") The number of lights varies from three at the Kansas site to nine at the South Dakota site. At all sites, the lights are distributed evenly around the pole, with South Dakota being unique in that the lights are arranged in three banks of three. Correspondence with HMLT manufacturers indicated that an EPA of 20 square feet was a reasonable average value for design. However, for the purposes

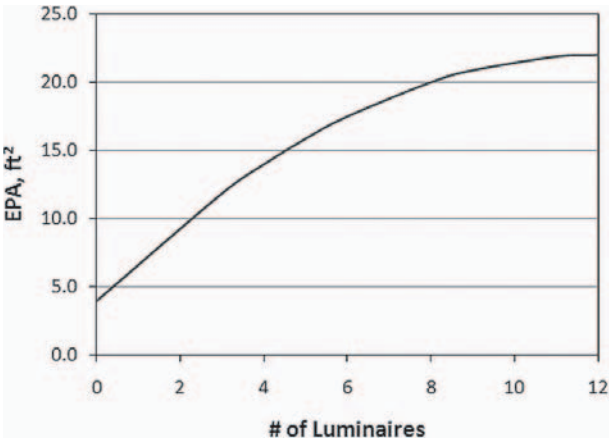

Figure 2.16. Estimated EPA of luminaires.

of establishing a wind load, it was decided to account for the variability. A mathematical model estimating the EPA of a luminaire based on the number of lights was created according to the following assumptions:

1. The upper bound EPA was 22 square feet corresponding to about 10 or 12 lights.
2. The lower bound EPA was 4 square feet accounting for the upper works without any lights attached.
3. The change in the EPA of the luminaire decreases with increasing number of lights due to the overlap in the projected area of individual elements. A parabolic curve was chosen to model this effect since no other data for modeling this effect could be found.

This method is conservative in relation to using a blanket value of 20 square feet since smaller EPAs result in larger static wind pressures. This is because the measured load effect must be maintained and a reduction in projected area needs to be balanced by increasing the applied static pressure. A plot of estimated EPA versus number of lights is shown in Figure 2.16, and the estimated EPA values used for analysis are listed in Table 2.3.

Table 3-6 in AASHTO Signs (2009) provides drag coefficients for members of varying shapes. With regard to circular, 16-sided, and 12-sided shapes—cylindrical, hexdecagonal, and

Table 2.3. Estimated EPA of luminaires for monitored sites.

ID	# LIGHTS	EST. EPA (ft^2)
KS	3	11.9
CA	4	14.0
ND	4	14.0
OK -NE	5	15.9
OK -SW	5	15.9
WY -CJE	6	17.5
WY -CJW	6	17.5
IA -N	8	20.0
IA -S	8	20.0
PA	8	20.0
SD	9	20.9

24 Fatigue Loading and Design Methodology for High-Mast Lighting Towers

dodecagonal respectively—the drag coefficient is known to vary with Reynolds number. This is reflected in the table; for a given dimension, the coefficients will reduce with greater wind velocity. To accurately determine the proposed fatigue load, this variation had to be considered. The three plots in Figure 2.17 illustrate the variation. These plots were arrived at using a velocity conversion factor of 1 for a 50-year recurrence interval and the most conservative values for corner radius. The diameter range considered bounds the typical sizes for a tapered HMLT pole.

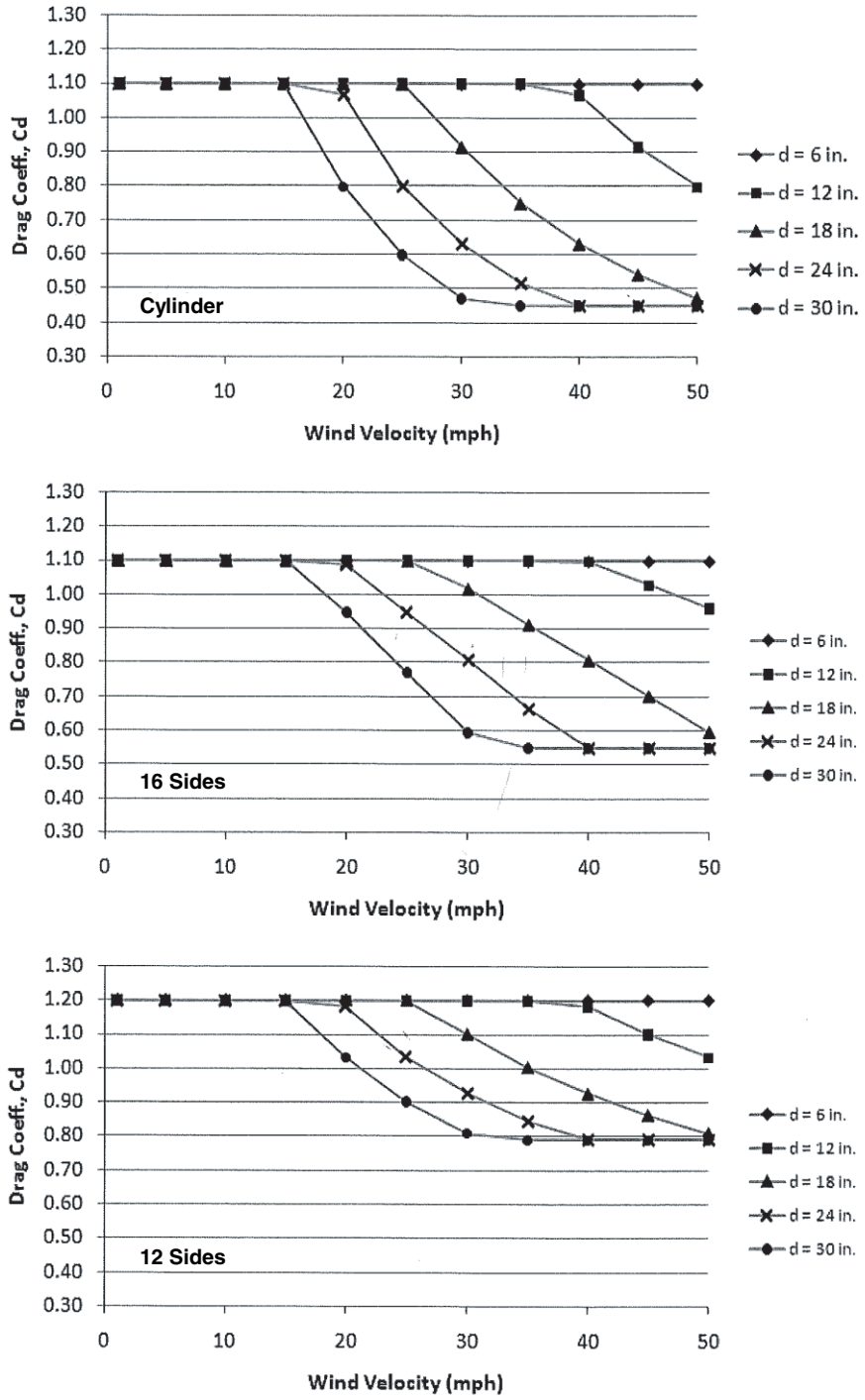

Figure 2.17. Variation of drag coefficient with regard to velocity, size, and shape.

For most of the wind velocities encountered in the wind-loading spectrum, the maximum value for drag coefficient could safely be assumed to be constant. Values of 1.1 were used to calculate wind loads for circular and 16-sided poles and a value of 1.2 was used for 12-sided poles. Furthermore, the current edition of AASHTO Signs (2009) states the location-specific yearly mean wind velocity shall be used to determine the drag coefficient, which is typically 11.2 mph, well below the break points shown in Figure 2.17.

2.3.4 Vortex Shedding Mitigation

Vortex shedding mitigation strategies have long been identified as a potential way to increase the fatigue life of existing structures as well as to improve the fatigue resistance for new structures. Many different strategies and devices exist that can alleviate the effects of vortex-induced vibration (Ahearn and Puckett, 2010). However, the focus of mitigation in this study was not on different strategies but on the response of an HMLT after a mitigation device was installed. Helical strakes were selected as the means of mitigation. In theory, the addition of strakes sufficiently disrupts the flow of steady wind around the pole, thereby preventing the formation of organized vortices that drive the structure to vibrate perpendicular to the flow of wind. Using rope, strakes were easily installed on the existing HMLTs by wrapping them around the exterior in a helical pattern. To do this, a maintenance worker would lower the luminaire, attach the ropes, lift the luminaire back onto position, and wrap the ropes "maypole" fashion. For luminaire maintenance, the strakes could simply be unwrapped prior to lowering the luminaire and rewrapped when completed.

2.3.4.1 Test Setup—WY-CJE and WY-CJW

The Creston Junction, Wyoming, site was specifically selected for the mitigation study since both HMLTs are identical and any experiment on one HMLT could easily be reproduced on the other. The initial setup was placed on the west HMLT and used a half-inch rope wrapped in a single helix with a frequency of about one wrap every 10 feet. The half-inch rope was arbitrarily chosen at the time of installation due to materials available at the local hardware store. About 90 days of data were collected for this configuration, and preliminary results showed a diminished number of accumulated stress cycles due to vortex shedding, but varied for different wind directions (further discussion of this result is provided in the next chapter). To achieve more uniform mitigation, a double rope strake was subsequently installed. The double-helix pattern created by the double stake provided greater coverage of the pole surface area by the strake, the frequency of the wrap being increased to one wrap every 5 feet. In addition to adopting the double-strake pattern, the size of the rope was increased to 1 inch, approximately one-tenth the average diameter of the pole. Previous research suggests one-tenth is a better ratio of strake-to-structure diameter for vortex shedding mitigation (Warpinski, 2006). The double strake was first installed on the west HMLT and then moved to the east HMLT in order to reproduce the results. An illustration of the two strake patterns is shown in Figure 2.18, and a summary of data collection periods with regard to stake pattern is listed in Table 2.4.

2.3.4.2 Test Setup—IA-N

The strake test setup at the Iowa site examined the placement of the strake along the length of the HMLT. Dynamic analysis indicated the majority of the oscillations due to vortex shedding occurred in the top one-third of the pole, near the upper antinodes of the second and third mode shapes. Observed behavior of HMLTs during vortex shedding events agreed with this hypothesis; oscillations appeared most pronounced in the upper portion of the pole. To experimentally verify if a strake is only required on the top third of an HMLT, the Iowa strake was installed in two separate segments. The two segments met at the first slip joint down from the luminaire. The top segment covered approximately the top third of the pole, while the bottom segment covered the remaining portion. After sufficient data were collected to confirm the full-length strake was

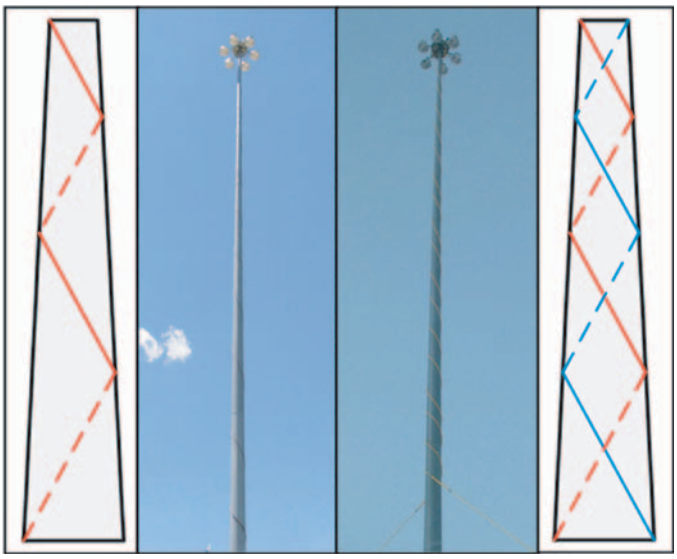

Figure 2.18. Single- and double-strake configurations.

successful in reducing the daily cycle count, the lower segment of rope was removed. The strake segments evaluated are illustrated in Figure 2.19.

Like the double strake installed at the Wyoming site, the Iowa strake consisted of a double wrap with one-inch rope. The frequency of wrapping for a single rope was about one revolution per eight feet making the wrap for the double strake about once every four feet. The upper segment used a high quality one-inch nylon rope, which was securely installed with hose clamps top and bottom to ensure it did not unwrap or come down in the wind. The lower segment used a one-inch polypropylene rope secured at the top with duct tape and at the bottom with a ratchet strap. The duct tape allowed easy removal of the lower segment once the data collection period ceased. A summary of data collection periods with regard to strake segment coverage is listed in Table 2.5.

2.3.4.3 Methods of Evaluating Mitigation

To evaluate the effectiveness of the strake test setups described above, two independent methods were used. First, stress-range histogram data were evaluated using traditional fatigue analysis. The effective constant-amplitude stress range, fatigue-limit-state stress range, and cycle frequencies were calculated for periods with and without strakes and compared. This provided a quantitative means of evaluating the fatigue effect. Second, the occurrences of across-wind excitation were noted for periods with and without strakes and compared. This provided a more qualitative means of evaluating the vortex shedding phenomena. The method used to determine across-wind excitation is included in Appendix F (available on the TRB website).

Table 2.4. Strake periods for Creston Junction, Wyoming, HMLTs.

PERIOD	WY-CJE	WY-CJW
July 4 – Oct. 6, 2009	N	S
Oct. 6, 2009 – Jan. 20, 2010	N	N
Jan. 20 – Apr. 15, 2010	N	D
Apr. 15, 2010 – Mar. 15, 2011	D	N
Mar. 15 – June 6, 2011	N	N

N—No strake
S—Single strake, ½" diameter
D—Double strake, 1" diameter

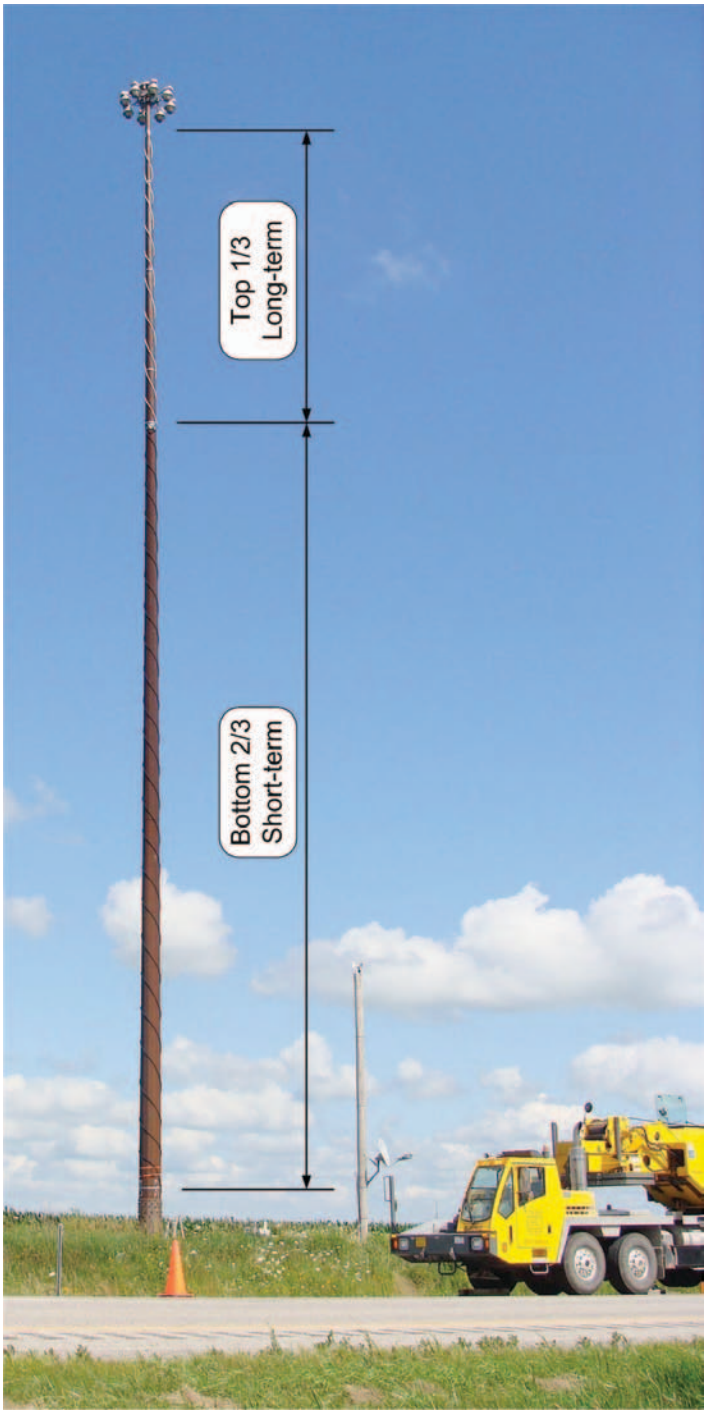

Figure 2.19. IA-N strake sections.

Table 2.5. Strake periods for IA-N HMLT.

PERIOD	COVERAGE
July 16 – Nov. 30, 2010	Full
Nov. 30, 2010 – June 9, 2011	Top Third

2.4 Fatigue Wind Load Methodology

To establish rational loads for fatigue design of HMLTs, the following methodology was developed to analyze collected data. This methodology proposes the creation of a "fatigue wind" similar to the fatigue truck used in the design of highway bridges. The following analogy explains the similarity: as trucks are used to define highway bridge live load, wind is used to define HMLT live load. Both truck loading and natural wind produce stress ranges that are variable in amplitude and difficult to characterize in both magnitude and frequency.

Whereas the AASHTO LRFD Bridge Design Specifications allow for either finite or infinite fatigue design life, this study focuses on the infinite life approach. The current AASHTO signs guidance (2009) state that estimating the lifetime loading histogram for such structures is "practically impossible" and an infinite life fatigue design approach is recommended. During this study, considerable data were collected to extrapolate a lifetime loading histogram for an HMLT, but the total number of cycles over the lifetime is large enough to render finite life design impractical. For example, if the lifetime cycles for a given HMLT exceed the number of cycles at the constant-amplitude fatigue limit (CAFL) for a Category E′ detail, infinite life design must be used. This is consistent with AASHTO LRFD Bridge Design Specifications, Section 6.6.1.2.3, where provisions for finite/infinite life design are given (AASHTO LRFD, 2010).

A flowchart illustrating the methodology used is shown in Figure 2.20. The flowchart may be divided into three basic steps:

1. **Stress-range histogram data:** Collect, edit, and verify stress-range cycle data in the form of stress-range histograms.
2. **Fatigue life:** Calculate effective constant-amplitude stress-range, cycle frequency, and fatigue-limit-state stress-range, and then determine appropriate fatigue life design—finite versus infinite.
3. **Fatigue load:** Calculate corresponding fatigue load effect in terms of moment range, static pressure range, and wind velocity range.

Each of these will be discussed in the following sections.

The purpose of the methodology is to show how the fatigue-limit-state load is determined and to show that infinite life design is most practical. Using the proposed fatigue-limit-state load, some existing HMLTs may be limited to finite life. Considering these circumstances, the extrapolated lifetime loading histogram can be used for finite fatigue life evaluation. Guidance is given later in the report for evaluation of HMLTs subject to finite life.

2.4.1 Stress-Range Histogram Data

The stress-range histogram data collected on-site were considered "raw" because the data required further reduction. Before analyzing the data to determine fatigue damage, they were verified and edited if necessary. For example, the buffered stress time-history recorded on-site may have included noise that was interpreted as stress cycles by the rainflow algorithm. Typical noise spikes manifested themselves as high stress-range cycles in the histogram; they might have been identified as outliers or counted with true values. Since higher stress ranges account for greater fatigue damage, these errors affected calculating both the effective constant-amplitude stress range (S_{Reff}) and the fatigue-limit-state stress range (S_{Rfls}), inflating the cumulative results. Due to the extremely large number of cycles experienced by the HMLTs over the long duration of monitoring, the impact of false cycles on the S_{Reff} calculation was likely negligible; however, the impact on the 1:10,000 S_{Rfls} calculation used for infinite life design could have yielded overly-conservative results. For this reason, a quality control plan was implemented verifying high stress-range cycles by searching through the trigger data for high cycle events and visually inspecting for

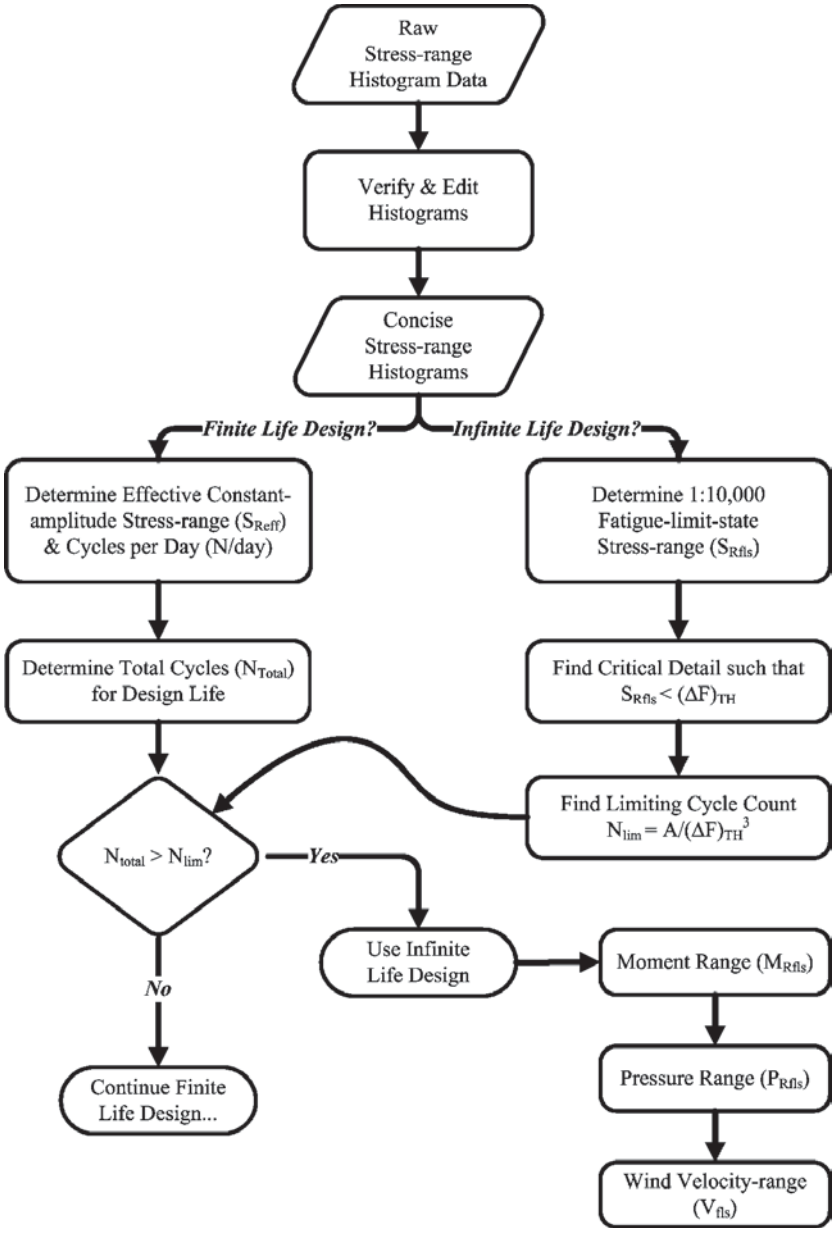

Figure 2.20. Methodology flowchart for development of fatigue wind load.

noise. Another common error found in the histogram data resulted from the zero routine used by the data logger. The strain gage readings drifted over time and were digitally reset to compensate. If the drift was larger than the natural stress cycle at the time of the reset, it was counted as an exceedingly large cycle.

Even though the trigger files were designed to minimize the amount of time-history data collected, they still resulted in large, cumbersome files containing data stored piecemeal over many months of the project. To aid in sorting through the trigger files to find the critical stress-range cycles, a computer routine was written. The routine broke the data into time intervals matching the rainflow routine, identified maximum stress-range cycles, and sorted them from highest to lowest. The top stress-range events were then printed on-screen so the user could verify them.

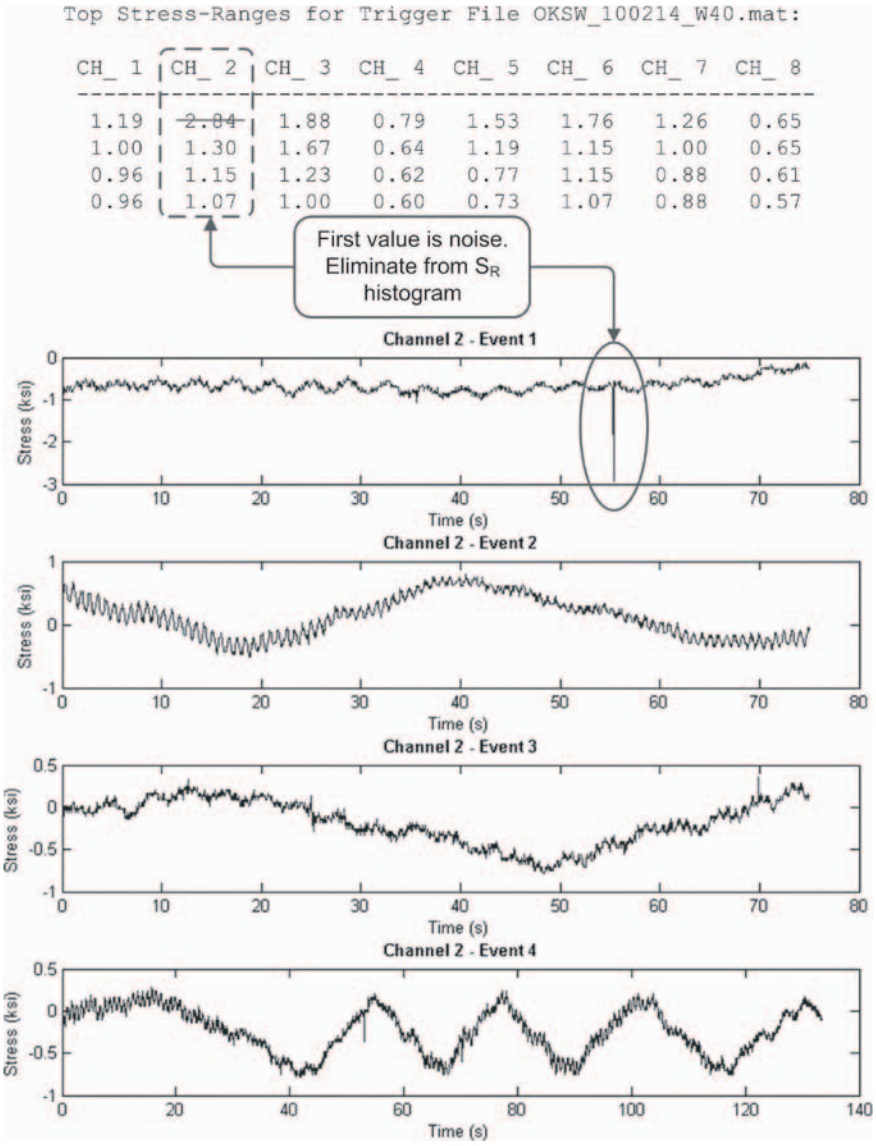

Figure 2.21. Verification of stress-range cycles.

If the user found an anomaly, it was eliminated from the stress-range histogram. This verification process is illustrated in Figure 2.21.

The data presented, and subsequent results, are based on selection of two strain gage data sets per HMLT. After a thorough review of the response of the HMLTs and characterization of the general behavior, two strain gages, one along-wind and one across-wind, were determined sufficient to represent the cumulative loading effects on a given HMLT. The prevailing wind direction was determined from the wind direction rosettes for percent occurrence. The nearest strain gages to the prevailing direction were termed along-wind and the nearest gages orthogonal to the prevailing direction were termed across-wind. In most instances, there were two strain gages to choose from for each direction—most gages being opposite of one another. In choosing between these two, the strain gage with a greater time length of data collection was chosen (some gages having failed over the duration of this study). If the time of collection was the same for both, the strain gage exhibiting the higher effective constant-amplitude stress was chosen. In other words, the other gages were found to provide redundant data and hence,

were not essential in the development of the loading. Throughout this report, data from the along-wind strain gages are noted with an "A" and data from across-wind strain gages are noted with an "X."

2.4.2 Fatigue Life

The current edition of AASHTO Signs recommends an infinite life approach since the number of wind load cycles expected over the life of a sign, signal, or luminaire support structure is unknown. This uncertainty makes infinite life the most practical approach because the number of cycles is not required for infinite life design. However, due to the HMLT failures prompting this study, the anticipated load effect and number of loading cycles during the life of the structure came into question. To prove infinite life design is sound, both load effect and number of cycles had to be examined. The load effect is quantified by the effective constant-amplitude stress-range (S_{Reff}) and the 1:10,000 fatigue-limit-state stress range (S_{Rfls}). The life of the structure is quantified by cycle counts (N). All three parameters are determined from the stress-range histogram.

For design purposes, the detail (and thus the limiting cycle count, N_{lim}) is determined by the design engineer and must provide adequate resistance against the fatigue-limit-state load effect. The task of this study is the opposite—experimentally determine a reliable fatigue-limit-state load effect and the corresponding total cycles for design life (N_{tot}) and then compare with the appropriate stress-life (S-N) curve.

2.4.2.1 Limiting Cycle Count

S_{Rfls} is the minimum stress-range that can be used for infinite life design and is found by statistical analysis. This concept is illustrated in Figure 2.22. In summary, a statistical distribution was fit to each data set, and the 1:10,000 stress range was extracted from the probability density function. The 1:10,000 return period is an established value commonly used in fatigue analysis and is the basis for the current AASHTO LRFD Bridge Design Specifications provision for infinite life. In other words, the Fatigue I load combination is the truck loading associated with this probability of occurrence (AASHTO LRFD, 2010). In order for infinite life to be valid, the fatigue resistance of a given detail must exceed S_{Rfls}. The fatigue resistance associated with the endurance limit of a detail is known as the constant-amplitude fatigue limit, or CAFL. CAFL values are determined from the stress-life (S-N) curves for different detail categories. The cycle count associated with the endurance limit is herein referred to as the limiting cycle count (N_{lim}). The CAFL and limiting cycle count for a Category D detail is illustrated in Figure 2.23.

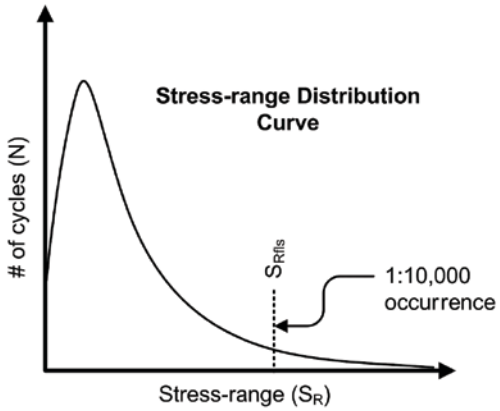

Figure 2.22. Fatigue-limit-state stress range.

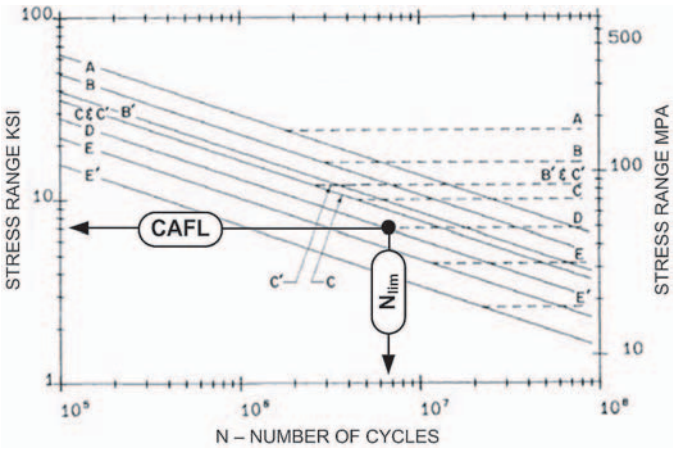

Figure 2.23. Stress-life curve illustrating N_{lim} (AASHTO LRFD, 2010).

2.4.2.2 Total Cycles for Design Life

S_{Reff} is an effective stress-range representing the effect of all the stress cycles in the variable-amplitude spectrum, and is calculated using Miner's Rule (Miner, 1945), which is shown in Equation 2.8.

$$S_{Reff} = \left(\frac{\sum N S_R^3}{\sum N} \right)^{1/3}$$

Equation 2.8: Miner's Rule

S_{Reff} along with the accumulated number of cycles (ΣN) are used to determine fatigue damage and remaining fatigue life in an existing structure. With regard to infinite fatigue life design, S_{Reff} and ΣN are used to estimate the total cycles for design life, N_{tot}. These values vary based on the level of truncation selected for the histogram. Truncation is an important step in determining a useful value of S_{Reff}, one that is neither too high nor too low for the type of detail considered. If N_{tot} is greater than N_{lim} for a given detail, then infinite fatigue life design should be used. If N_{tot} is less than N_{lim}, then finite fatigue life should be used.

2.4.3 Fatigue Load

After establishing stress range values—S_{Reff} and S_{Rfls}—for each of the HMLTs in the study, they needed to be converted to a normalized parameter applicable to any given HMLT structure. Unique to any structure, stress range depends on loading, geometry, and section properties. The normalized parameter, typically expressed as a load, can be applied to any structure to determine an appropriate fatigue stress range. For example, the fatigue truck used in the AASHTO Bridge Specifications can be applied to any bridge, regardless of type, span length, connections, etc. To do the same for HMLTs, the parameter needs to be expressed as a wind load, or more precisely, a pressure range or velocity range.

Converting stress range to wind velocity requires a series of calculations. The first step in this procedure is to convert the stress-range values to moment range using specific HMLT geometry and basic mechanics of materials. The next step is to convert the moment range to a normalized parameter using fluid equations for static pressure and velocity. Figure 2.24 shows the equations for converting moment range to static pressure and wind velocity. The design wind pressure is based on

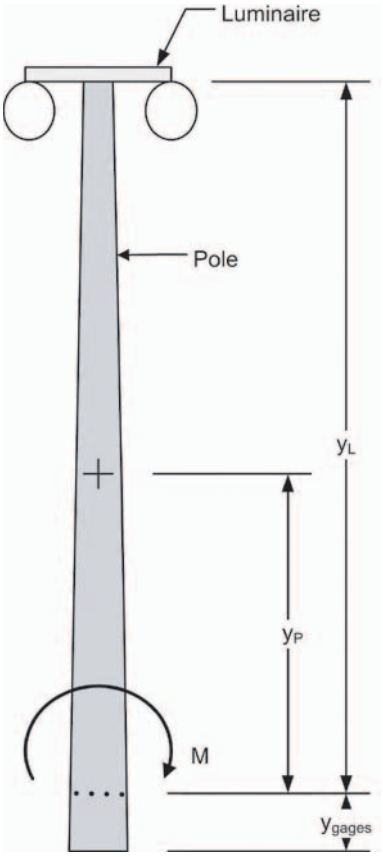

Design wind pressure:

Experimental wind pressure:

$$P_e = \frac{M}{C_d A_p y_p + EPA_L y_L} \quad (psf)$$

Setting the two equations equal, wind speed can be calculated from the applied moment using the equation,

$$V = \sqrt{\frac{M}{0.00256\left(C_d A_p y_p + EPA_L y_L\right)}} \quad (mph)$$

where:

EPA_L = Projected area of luminaire, equal to projected area times drag coefficient (ft^2)
A_p = Projected area of pole (ft^2)
C_d = AASHTO drag coefficient applied to pole
M = Applied moment (lb-ft)
V = Effective wind speed (mph)
y_{gages} = Height of strain gages (ft)
y_p = Distance to C.G. of pole (ft)
y_L = Distance to luminaire (ft)

Figure 2.24. Fatigue static pressure and wind velocity computation.

the fundamental wind pressure equation given in AASHTO Signs (2009). The height and exposure factor, K_z, is excluded due to variation in individual pole heights, and the gust effect factor, G, is excluded for use with lower wind speeds. The importance factor for HMLTs, as suggested by AASHTO Signs C11.6 (2009), is taken as unity. The experimental wind pressure is related to bending moment by basic statics. Note that the drag coefficient is included in the equation for experimental wind pressure instead of design wind pressure. As given in Table 3.6 of AASHTO Signs (2009), separate drag coefficients should be used for the pole and luminaire. Furthermore, the drag coefficient for the luminaire *attachment* is typically included in the EPA of the luminaire.

The wind load for the proposed specification is presented in terms of static pressure-range. The concept of velocity range is included to provide an intuitive feel for the proposed load since the velocity range may be compared to other design wind speeds. Pressure range was chosen for the specification due to its simplicity; velocity range would need to be converted to a static pressure-range in the design process anyway. The applied pressure range will yield the desired stress range, which is necessary for fatigue design. The same concept is utilized in the existing AASHTO Bridge Specifications (2010), except that the Fatigue I load combination is used instead of a static pressure range.

The fatigue-limit-state static pressure-range, P_{fls}, is the basis for the proposed methodology for infinite life design of HMLTs. It is determined from S_{Rfls} using the process shown above. The load in the proposed specification is termed *the combined wind effect* as described in an earlier section. It is a function of P_{fls}, drag coefficient, and importance category. The development of this load and associated findings are presented in the next chapter.

CHAPTER 3

Findings and Applications

3.1 Results of Field Tests

Results from field test data including dynamic properties, wind stochastic data, stress-range histogram data, and effects of mitigation are presented and discussed in the following sections.

3.1.1 Dynamic Properties of HMLTs

A summary of modal frequency and damping ratio values for the HMLTs studied in this report is provided in Table 3.1. The damping ratio values listed are a composite of the two calculation methods described in Chapter 2. For the HMLTs included in the long-term monitoring study, values for the first mode are an average of pluck data using the log-decrement method and ambient data using the half-power bandwidth method. Ambient data were given priority for the higher modes. Damping ratio values for HMLTs not included in the long-term monitoring study were calculated using only pluck data.

Modal frequency values are plotted in Figure 3.1 for all poles. The same data are presented in Figure 3.2 plotted against HMLT height. Note the tendency of the modal frequency values to decrease with increasing height, as expected.

Damping ratio values are plotted in Figure 3.3. Note the tendency of the damping ratios to *decrease* with increasing mode number. This decrease may be explained by the tendency of the HMLT to respond to different forms of excitation. For example, since Modes 2 and 3 are more likely to be excited by vortex shedding, the effects of aerodynamic damping would be expected to be more prevalent for these modes. This would be consistent with the observed behavior in the field (i.e., vortex shedding occurring in Modes 2 and 3).

Statistical analysis was used to determine confidence limits for damping ratios to be used for evaluation and design of HMLTs. In addition to the data presented in Table 3.1, damping ratio values from the report *Field Instrumentation, Testing, and Long-Term Monitoring of High-Mast Lighting Towers in the State of Iowa* (Connor and Hodgson, 2006) were included in the data set. Histograms and frequency distribution curves for Modes 1 through 3 are shown in Figure 3.4. Each figure includes a Weibull distribution scaled to fit the shape of the corresponding histogram. The Weibull distribution was chosen because of its application in a domain from zero to infinity and suitability in failure analysis.

Table 3.2 lists the damping ratios at the 50 percent, 80 percent, and 95 percent exceedance levels for each mode. For Mode 1, the damping ratio at 95 percent confidence equals 0.5 percent, a match with the damping ratio specified in the current edition of AASHTO Signs. The damping ratio at 80 percent confidence equals 0.8 percent, a reasonable match with the Canadian Specification (2006). Both are conservative with varying degrees of confidence. However, for Modes 2 and 3, the

Table 3.1. Modal frequency and damping ratio summary.

ID	FREQUENCY (Hz)				DAMPING RATIOS (%)			
	1st	2nd	3rd	4th	1st	2nd	3rd	4th
CA	0.37	1.73	4.72	9.45	1.3	0.4	0.4	-
IA-N	0.32	1.33	3.41	6.53	1.2	0.4	0.4	0.3
IA-S	0.35	1.41	3.26	6.24	1.6	1.0	0.5	-
KS	0.36	1.66	4.45	9.21	0.8	0.3	0.1	0.1
ND	0.31	1.28	3.15	5.94	1.3	0.5	0.2	-
ND (LL)	0.34	1.40	3.38	6.29	0.8	0.3	0.3	0.4
ND-8 3	0.30	1.12	2.98	5.84	1.5	0.4	0.1	0.4
ND-9 4	0.28	1.12	2.95	5.64	1.9	0.9	0.5	0.6
ND-EXP	0.25	1.09	2.91	5.54	2.2	0.6	0.4	0.7
ND-MEM	0.31	1.58	4.18	7.60	1.2	0.4	0.4	0.3
ND-SUN	0.31	1.34	3.36	6.40	1.4	0.4	0.6	0.7
OK-E	0.28	1.18	3.16	6.03	1.4	0.4	0.2	0.5
OK-NE	0.26	1.03	2.83	5.15	1.9	0.7	0.3	0.3
OK-SE	0.26	1.03	2.85	5.28	0.8	1.3	1.5	-
OK-SW	0.26	1.20	3.25	6.91	1.4	0.6	0.1	0.3
PA	0.39	1.68	4.60	9.37	1.2	1.1	-	-
PA-AD	0.38	1.93	4.77	9.52	0.6	2.3	1.7	1.1
SD	0.29	1.17	2.98	5.81	0.8	0.3	0.1	0.3
SD-1E	0.33	1.33	3.44	6.50	1.4	0.6	0.4	0.8
SD-1W	0.33	1.32	3.46	6.43	0.6	0.2	0.1	0.5
SD-42E	0.38	1.76	4.74	8.92	1.0	0.8	0.8	2.2
SD-42W	0.44	2.33	6.28	13.37	2.1	0.9	0.8	0.6
WY-219E	0.58	2.80	6.84	13.99	1.4	1.3	0.3	0.1
WY-219W	0.39	1.77	4.57	9.00	0.9	-	0.8	-
WY-228W	0.39	1.56	3.96	7.52	0.7	0.4	0.2	0.6
WY-CJE	0.35	1.50	3.85	7.54	1.2	0.6	0.1	0.2
WY-CJE(LL)	0.47	1.78	4.25	7.89	0.8	0.2	0.5	0.7
WY-CJW	0.35	1.53	3.89	7.56	1.1	0.6	0.1	0.4
WY-CJW(LL)	0.48	1.78	4.24	8.26	0.8	1.3	0.3	0.4

"LL" refers to pluck tests where the luminaire was lowered.

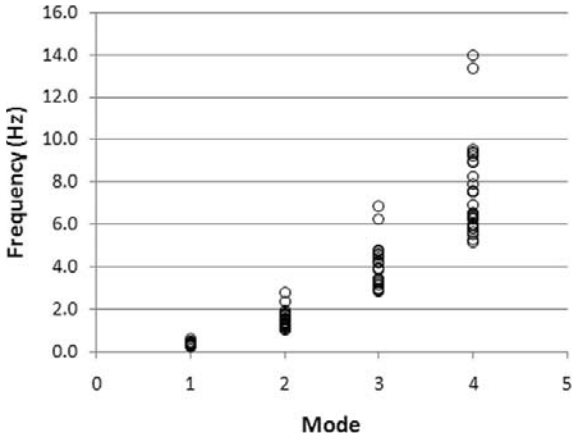

Figure 3.1. Modal frequency versus mode number.

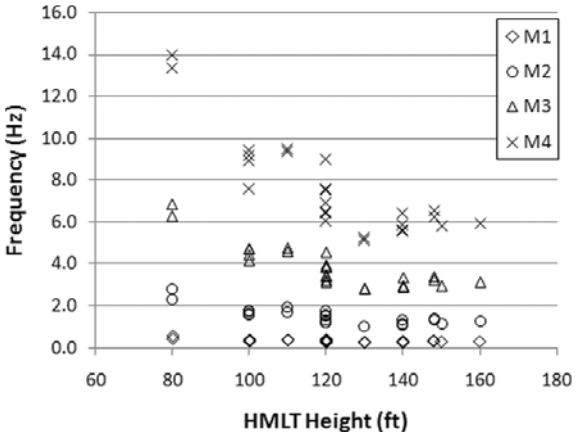

Figure 3.2. Modal frequency versus HMLT height.

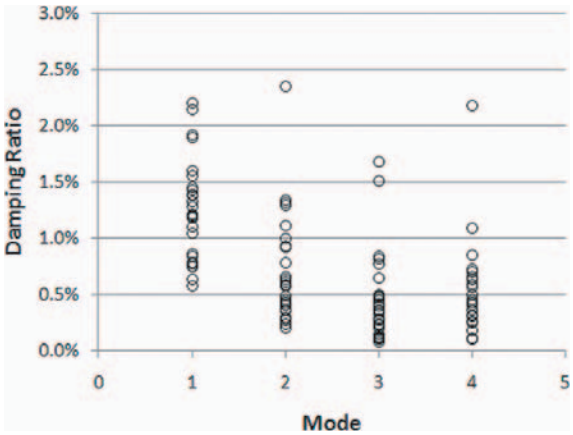

Figure 3.3. Damping ratio versus mode number.

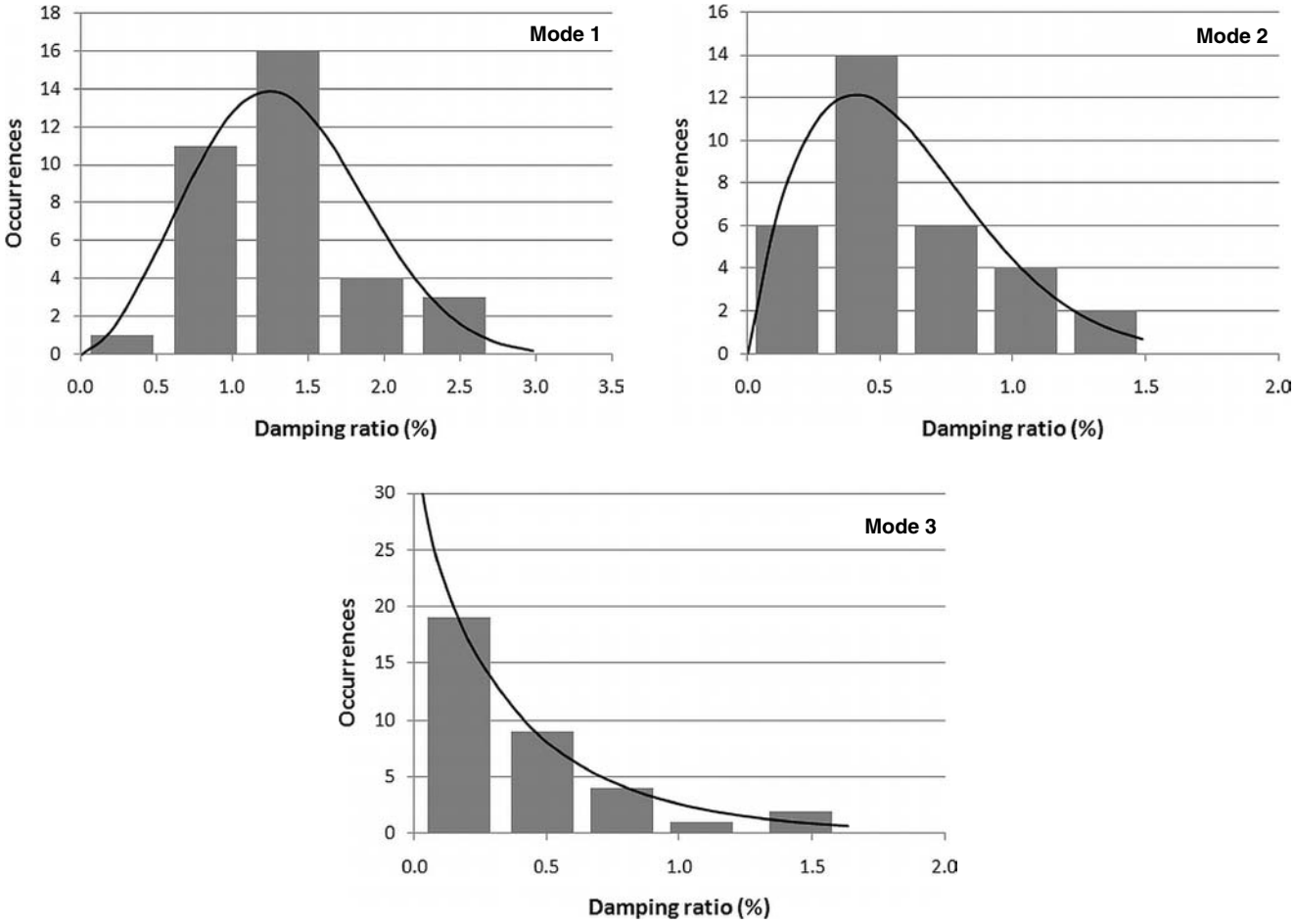

Figure 3.4. Frequency distribution of damping ratios.

Table 3.2. Damping ratios at selected confidence limits.

CONFIDENCE (% EXCEEDENCE)	MODE		
	1	2	3
50 (mean)	1.3%	0.6%	0.4%
80	0.8%	0.3%	0.1%
95	0.5%	0.1%	0.02%

damping ratios are significantly less. Since AASHTO Signs only assumes one mode of vibration, no comparison can be made for the higher modes. In summary, the data suggest that a lower bound estimate of the damping for each mode could be used for design if a method for calculating dynamic load effects is required. A similar conclusion was reached in the previously cited study by Connor and Hodgson (2006).

3.1.2 Wind Data

Mean wind speeds, peak 10-minute average wind speeds, and maximum recorded wind speeds for each site are given in Table 3.3. Data were collected using an anemometer at each site mounted near the standard 33-foot (10-meter) height. Average wind speed and maximum wind speed were recorded at 10-minute intervals for the duration of the study. The mean wind speed listed in the table is simply the mean value of all 10-minute averages recorded during the *entire* monitoring period for the given pole. The peak 10-minute wind speed average is the highest 10-minute average recorded and is indicative of the highest *sustained* wind speed. The maximum wind speed listed is the highest *instantaneous* wind speed sampled. All values in Table 3.3 are

Table 3.3. Measured wind speed data (mph).

ID	SPEED (mph)		
	MEAN	PEAK 10-MIN AVG	MAX
CA	8.7	37.8	55.4
IA-N	11.5	46.4	56.5
IA-S	10.3	38.3	53.4
KS	9.4	45.9	64.6
ND	6.7	34.0	55.4
OK-NE	6.8	31.4	53.3
OK-SW	8.8	41.8	65.5
PA	3.5	21.5	45.3
SD	7.8	37.0	60.0
CJE (FR)	12.8	40.9	78.0
CJE (MT)	14.3	49.2	63.8
CJW (FR)	14.0	45.9	64.6
CJW (MT)	12.4	40.8	60.4

FR—Cumulative data without strakes (free)

MT—Cumulative data with double strakes (mitigated)

38 Fatigue Loading and Design Methodology for High-Mast Lighting Towers

independent of wind direction; Appendix D (available on the TRB website) includes wind rosettes for percent occurrence and average wind direction. Mean wind speed data are used later in this report to establish the proposed fatigue wind load.

3.1.3 Stress-Range Histogram Data

Stress-range histogram data for most of the long-term monitored HMLTs are plotted together in Figure 3.5. Using the normalized parameters, static pressure-range and cycle frequency, a direct comparison of the data may be made. Cycle frequency is presented in terms of cycles per day by dividing the total number of cycles by the true monitoring period (i.e., excluding any time the data logger may not have been recording). All data plotted are for periods without rope strakes, or, in other words, unmitigated. Data for the IA-N HMLT are not included since a strake was present for the entire duration. A general trend of decreasing cycle frequency with increasing load effect can be seen. As expected, cycles of high magnitude stress range occur less often. Also apparent is the increase in variation of frequency with increasing load effect. This variation can be explained, in part, by observed variation in the wind speed.

Data for selected HMLTs are re-plotted in Figure 3.6 along with best-fit lines illustrating the increase in the frequency of higher load cycles with mean wind speed. For example, a load effect corresponding to a stress range of 4 psf occurred with a frequency of about once every hundred days at the Erie, Pennsylvania, HMLT (mean wind speed of 3.5 mph), while the same load effect occurred about a hundred times a day in Creston Junction, Wyoming (mean wind speed of 14.0 mph). Hence, the greater the mean wind speed, the greater the fatigue-limit-state load that would be expected.

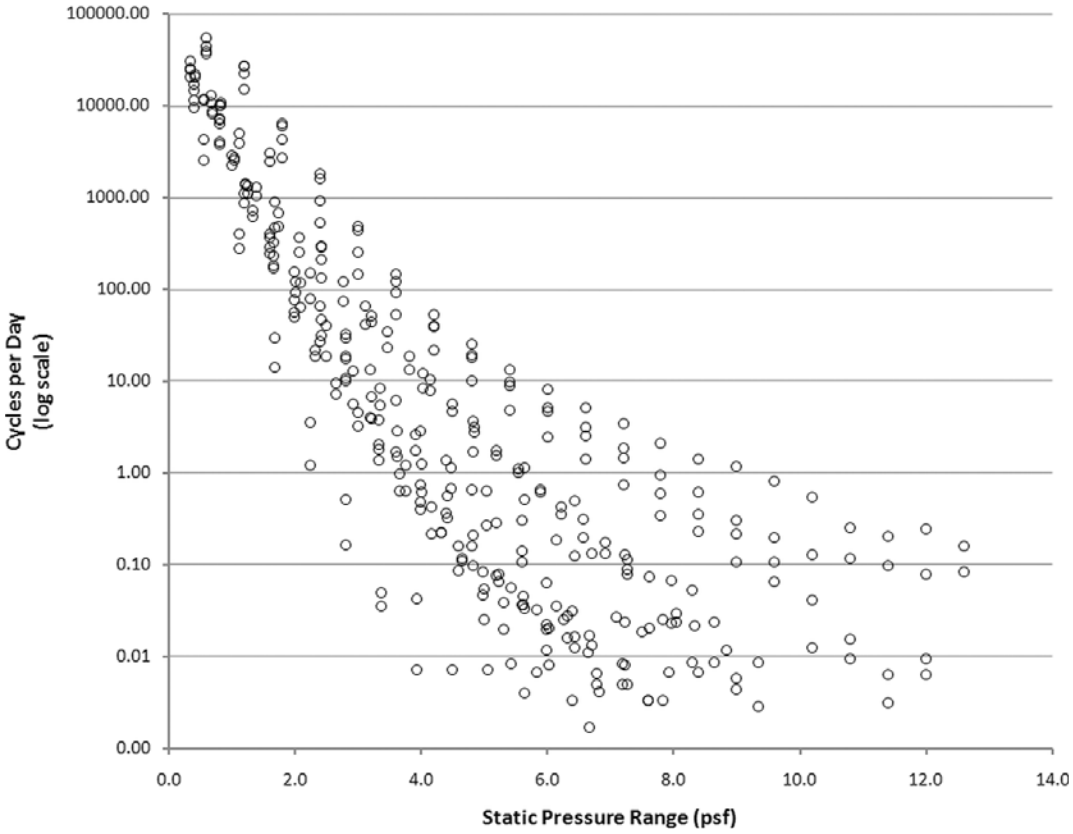

Figure 3.5. Normalized pressure-range histogram data for all sites.

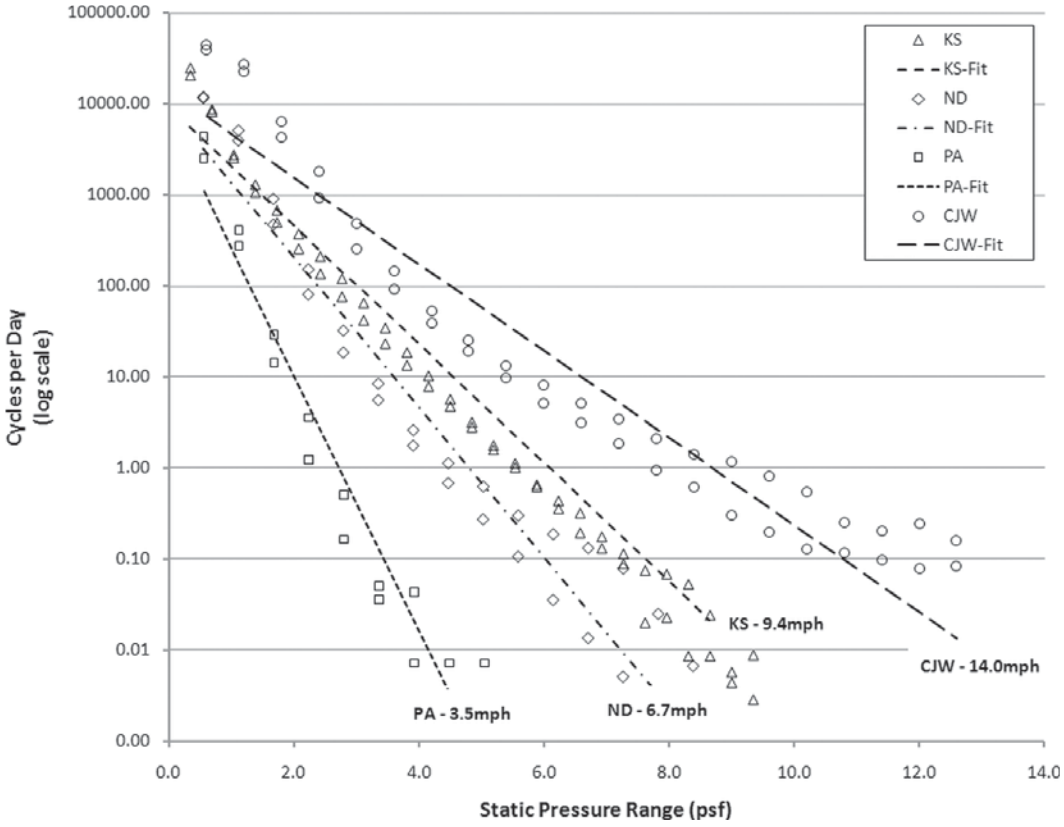

Figure 3.6. Pressure-range histogram data for selected sites illustrating variation due to wind speed.

Values for the fatigue-limit-state stress range, static pressure-range, and velocity-range are tabulated in Table 3.4 along with cycle counts. The histograms used to determine the fatigue-limit-state stress range were not truncated—in other words, all the data were considered in determining the best fit for the distribution. In addition, the upper-limit of all stress-range bins was used to return the most conservative result. For example, a bin counting all stress ranges between 3.0 ksi and 3.5 ksi would use 3.5 ksi to represent the bin during the distribution fit. This ensures all cycles contained in any given bin would be less than the stress range used to represent that bin, which is a conservative approach appropriate for design. The highlighted values for static pressure-range are used to formulate the proposed fatigue design load for *new* poles.

Note, in every case, the number of cycles per day for the across-wind direction exceeds those for the along-wind direction, which indicates the effect of vortex shedding due to the vibration at a higher mode. Also, note the significant reduction in cycle counts between the free and mitigated conditions for the Wyoming HMLTs. "Mitigated" is used to describe data collected while double strakes were placed on the pole. The unmitigated, or free, condition is noted in tables and figures as "FR", and the mitigated condition is noted as "MT".

Values for constant-amplitude effective stress range, static pressure-range, and velocity range are tabulated in Table 3.5 along with cycle counts. Values are presented for two different levels of truncation, one above 0.5 ksi and the other above 1.0 ksi. Truncating the lower bins of a histogram is common practice in a fatigue analysis. This is typically done so the effective stress range is not falsely "pulled down" by the high number of very small stress range cycles. The two truncation levels correspond to about one-third and one-half the constant-amplitude fatigue threshold for Category E′, respectively. The histograms used to determine the constant-amplitude effective

40 Fatigue Loading and Design Methodology for High-Mast Lighting Towers

Table 3.4. Summary of fatigue-limit-state data.

ID	STRAIN GAGE	S_{Rfls}	p_{fls}	V_{fls}	N_{tot}	Days	N/Day
		(ksi)	(psf)	(mph)			
CA-A	CH_3	5.76	4.60	42.4	9,214,499	602.3	15,300
CA-X	CH_5	4.51	3.60	37.5	9,962,977	602.3	16,543
IAN-A (MT)	CH_9	6.17	4.46	41.7	1,851,318	130.7	14,160
IAN-X (MT)	CH_12	5.21	3.76	38.3	2,321,984	130.7	17,760
IAS-A	CH_2	3.24	6.07	45.1	473,141	168.7	2,805
IAS-X	CH_1	2.87	5.36	42.4	585,046	168.7	3,468
KS-A	CH_2	7.17	4.96	44.0	15,125,738	457.3	33,079
KS-X	CH_6	7.73	5.34	45.7	13,549,087	345.5	39,217
ND-A	CH_1	3.54	3.96	39.3	9,592,205	593.8	16,154
ND-X	CH_5	3.87	4.32	41.1	10,713,385	593.8	18,043
OKNE-A	CH_3	4.58	3.68	37.9	5,599,228	242.4	23,096
OKNE-X	CH_5	4.19	3.36	36.3	6,331,421	242.4	26,116
OKSW-A	CH_8	4.45	2.87	33.5	9,979,764	251.9	39,613
OKSW-X	CH_6	4.61	2.97	34.1	17,245,973	360.8	47,798
PA-A	CH_6	2.32	2.60	31.9	394,474	139.3	2,833
PA-X	CH_1	2.23	2.50	31.3	669,765	139.3	4,809
SD-A	CH_6	3.40	2.83	33.3	18,971,633	593.2	31,979
SD-X	CH_8	3.74	3.12	34.9	20,623,451	593.2	34,764
CJE-A (FR)	CH_8	4.06	4.87	43.6	17,778,845	317.2	56,050
CJE-X (FR)	CH_6	4.68	5.61	46.8	28,777,530	317.2	90,725
CJE-A (MT)	CH_4	4.57	5.48	46.3	4,549,210	301.6	15,084
CJE-X (MT)	CH_6	4.67	5.60	46.8	5,992,470	301.6	19,869
CJW-A (FR)	CH_8	5.10	6.12	48.9	23,030,758	341.6	67,413
CJW-X (FR)	CH_6	5.45	6.54	50.5	27,628,271	341.6	80,870
CJW-A (MT)	CH_1	3.97	4.76	43.1	1,248,053	74.5	16,743
CJW-X (MT)	CH_3	3.95	4.73	43.0	1,320,528	74.5	17,715

A—Along-wind direction

X—Across-wind direction

FR—Cumulative data without strakes (free)

MT—Cumulative data with double strakes (mitigated)

stress-range are based on the average bin stress-range values. Average bin values are appropriate for evaluation because they are an approximation of the center of the bin. The highlighted values for static pressure-range are used to formulate the proposed fatigue evaluation load for *existing* poles.

Note that in terms of cycle counts, the effect of vortex shedding diminishes with increased truncation, indicating the cycles produced by vortex shedding are concentrated in the lower bins.

3.1.4 Vortex Shedding Mitigation

Results of the mitigation testing using various rope strake configurations are presented here along with a discussion of the load effect associated with the mitigation strategy.

Table 3.5. Summary of effective constant-amplitude fatigue data.

TRUNCATION LEVEL		> 0.5 ksi				> 1.0 ksi			
ID	STRAIN GAGE	S_{Reff} (ksi)	p_{eff} (psf)	V_{eff} (mph)	N/Day	S_{Reff} (ksi)	p_{eff} (psf)	V_{eff} (mph)	N/Day
CA-A	CH_3	1.28	1.02	20.0	5,820	1.80	1.44	23.7	1,793
CA-X	CH_5	1.12	0.89	18.7	5,016	1.63	1.30	22.6	1,234
IAN-A (MT)	CH_9	1.36	0.98	19.6	5,927	1.94	1.40	23.4	1,788
IAN-X (MT)	CH_12	1.19	0.86	18.3	7,173	1.70	1.23	21.9	2,016
IAS-A	CH_2	0.92	1.47	24.0	2,805	1.47	2.36	30.4	356
IAS-X	CH_1	0.87	1.40	23.4	3,468	1.41	2.26	29.7	350
KS-A	CH_2	1.55	1.07	20.5	12,730	2.12	1.46	23.9	4,622
KS-X	CH_6	1.64	1.13	21.1	14,359	2.20	1.52	24.4	5,593
ND-A	CH_1	0.92	1.02	20.0	4,547	1.46	1.64	25.3	579
ND-X	CH_5	0.97	1.08	20.5	6,170	1.46	1.63	25.3	1,100
OKNE-A	CH_3	1.11	0.89	18.6	8,294	1.64	1.31	22.7	1,942
OKNE-X	CH_5	1.04	0.83	18.0	8,872	1.55	1.25	22.1	1,845
OKSW-A	CH_8	1.08	0.70	16.5	13,997	1.61	1.04	20.1	3,165
OKSW-X	CH_6	1.05	0.68	16.3	16,832	1.55	1.00	19.7	3,856
PA-A	CH_6	0.81	0.91	18.8	294	1.35	1.51	24.3	16
PA-X	CH_1	0.83	0.94	19.1	441	1.36	1.52	24.4	33
SD-A	CH_6	0.93	0.77	17.4	11,515	1.51	1.26	22.2	1,453
SD-X	CH_8	0.98	0.82	17.9	12,750	1.60	1.33	22.8	1,827
CJE-A (FR)	CH_8	1.02	1.22	21.9	18,693	1.57	1.88	27.1	3,472
CJE-X (FR)	CH_6	1.08	1.29	22.4	35,437	1.58	1.90	27.2	8,254
CJE-A (MT)	CH_4	1.08	1.30	22.5	6,037	1.62	1.94	27.5	1,345
CJE-X (MT)	CH_6	1.10	1.32	22.7	7,598	1.62	1.94	27.5	1,800
CJW-A (FR)	CH_8	1.06	1.27	22.3	28,228	1.61	1.93	27.5	5,721
CJW-X (FR)	CH_6	1.13	1.36	23.0	36,382	1.65	1.98	27.8	9,083
CJW-A (MT)	CH_1	1.03	1.23	22.0	6,688	1.59	1.90	27.3	1,252
CJW-X (MT)	CH_3	1.02	1.23	21.9	6,934	1.59	1.90	27.3	1,258

A—Along-wind direction

X—Across-wind direction

FR—Cumulative data without strakes (free)

MT—Cumulative data with double strakes (mitigated)

3.1.4.1 Results of Rope Strake Method

The full-length double-wrapped rope strakes described in Chapter 2 were effective at reducing the number of fatigue cycles accumulated and at reducing the occurrences of across-wind excitation, both of which are indicators of vortex shedding. Similar results were obtained at the three HMLTs where full-length strakes were installed. Experiments with the single-wrapped strake and the partial-length double strake were effective at reducing the effect, however, not to the same extent as the full-length double-wrap strake.

3.1.4.1.1 Creston Junction, Wyoming. To analyze the effectiveness of the single-wrap and double-wrap rope strake configurations at minimizing vortex shedding, a test was performed on

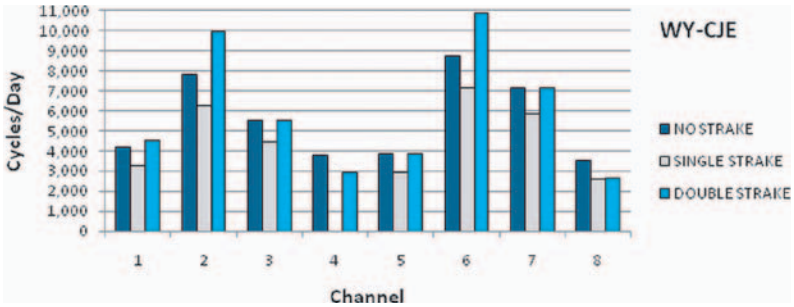

Figure 3.7. Cycle counts for WY-CJE (control group—no strakes installed).

the twin Creston Junction HMLTs. Three different strake configurations were tested: no strake, single strake, and double strake. WY-CJW was used as the experimental group where strakes were installed. WY-CJE was used as the control group, where no strakes were installed. Rainflow cycle counting was used to create stress-range histograms for both structures over all periods. The total number of cycles in the histogram was divided by the monitoring duration for each strake period to obtain the equivalent number of cycles per day.

The data in Figure 3.7 and Figure 3.8 present the results of this experiment. As seen in the figures, the strakes are successfully reducing the number of cycles in WY-CJW as compared to WY-CJE. Before discussing these results, there are a few important notes to consider:

1. The no-strake, single-strake, and double-strake labels shown in the legend refer to monitoring periods that are the same calendar periods for each HMLT and lasted approximately the same duration (e.g., the no-strake period refers to a monitoring period where strakes were not installed on either pole). Figure 3.7 presents the data for a given "control" pole (i.e., the pole for which there was no strake). Figure 3.8 presents the data from the same time for the corresponding pole where there was either no strake, a single strake, or a double strake installed.
2. The histogram data used to create the figures were truncated to stress-ranges above 1.0 ksi. Truncating the lower bins of a histogram is common in fatigue analysis, and is done here to keep the numbers manageable.
3. The strain gage labels or "channels" for WY-CJW have been shifted to account for the true orientation of the pole. The data presented for WY-CJW starts with Channel 8 followed by Channels 1 through 7. This shift aligns the channels in the figures with those having similar cardinal directions in the field. A more direct comparison between structures can be made in this fashion, as the wind would be coming from approximately the same direction for both HMLTs.

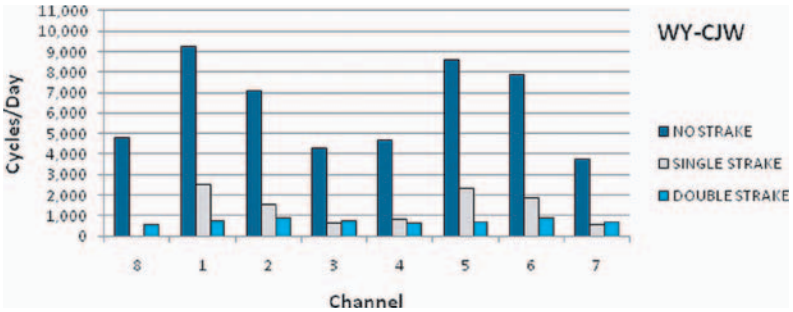

Figure 3.8. Cycle counts for WY-CJW (experimental group—strakes installed).

4. Wind data for the Creston Junction HMLTs indicate the wind is primarily out of the west. Thus, it would be expected that vortex shedding would cause vibrations mainly in the north-south direction, the across-wind direction, and strain gages placed on the northern and southern faces would have the greatest numbers of cycles. By examining the instrumentation plans in Appendix E (available on the TRB website), WY-CJE has Channels 2 and 6 placed in the north-south direction and Channels 4 and 8 placed in the east-west direction. For WY-CJW, Channels 1 and 5 are in the north-south direction and Channels 3 and 7 are in the east-west direction.

Begin by comparing the no-strake period to the single-strake period for WY-CJW, the experimental group shown in Figure 3.8. A significant reduction in cycles is noted in all channels with a reduction to less than 1,000 cycles per day in Channels 3, 4, 7, and presumably 8. Unfortunately, the data for Channel 8 are unavailable for the single-strake period. These channels represent activity in the along-wind direction. The remaining channels represent activity in the across-wind direction, where vortex shedding is expected to be more prevalent.

Extending the comparison to the double-strake period, there again is a significant reduction in the number of cycles per day. However, cycles for the double-strake period are reduced by approximately the same value for *all* channels, to less than 1,000 per day in each case. The cycle reduction for all channels is presumed to be because the double wrapping disrupts the vortices formed by wind from any direction. The sketches in Figure 2.18 best illustrate this reduction. Note that regardless of direction, there is always a strake on any windward face. This contrasts the single strake where there are lengths of pole where there is no strake on a downwind face. Providing a disruption at any given point on the pole significantly increases the likelihood of disrupting the flow that leads to vortex shedding.

After establishing the effectiveness of the double-wrapped strake, data continued to be collected for WY-CJW with the strake in place. The strake was then removed and installed at WY-CJE to replicate the results. Cycle counts for the free and mitigated conditions are presented in Figure 3.9 and Figure 3.10. These figures illustrate the effectiveness of the double-wrap strake for both HMLTs. Note that time periods and wind conditions were not the same for each; however, a reasonable comparison may be made considering the aggregate effect in the long-term.

It is also important to review the effective stress-range for any notable differences. One major concern of helical strakes is the increased area and corresponding drag they add to a structure. From the fatigue analysis there is no evidence that the addition of strakes results in the generation of larger stress ranges. The difference in the effective stress range from WY-CJW compared to WY-CJE is negligible between the free and unmitigated data sets. This is illustrated in Table 3.6 and Table 3.7. Histogram data used to calculate the stress ranges in the tables were truncated in

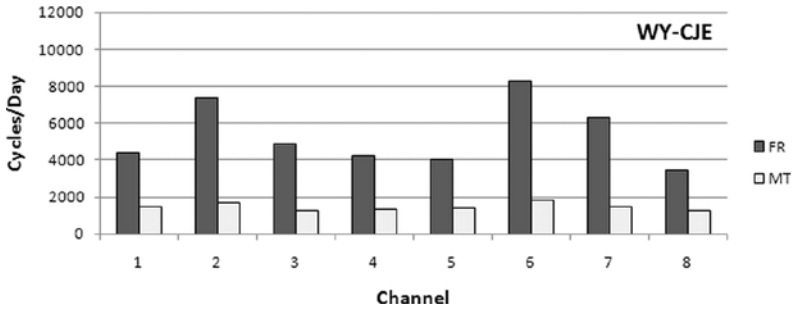

Figure 3.9. Free (FR) and mitigated (MT) cycle counts for WY-CJE.

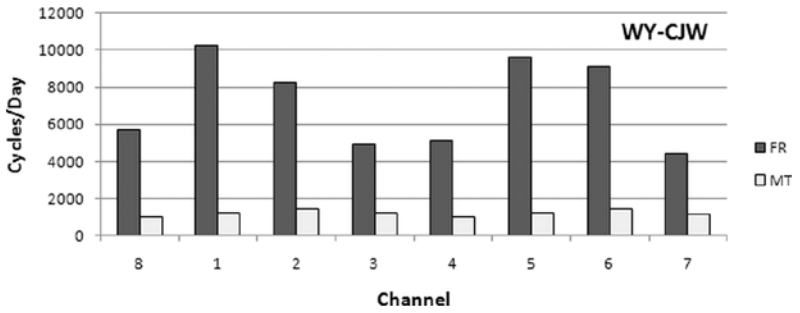

Figure 3.10. Free (FR) and mitigated (MT) cycle counts for WY-CJW.

the same manner as the data used in the previous figures. For all practical purposes, the effective stress range is the same for both HMLTs given the number of other varying factors between the structures such as local terrain effects, location of handhole, etc. A discussion of the load effect is presented later in this section and in 3.1.4.2.

In addition to cycle counts, the effectiveness of the double-wrap strake can be measured by examining the occurrences of across-wind excitation. In contrast to cycle counts, this method excludes the effect of along-wind stress cycles and, theoretically, the effect of buffeting. By excluding the along-wind response, the effect of vortex shedding can be more clearly evaluated. Plots of across-wind excitation for the free and mitigated conditions are presented in Figure 3.11 and Figure 3.12. Although the histogram data have previously shown a reduction in the number of damaging stress-cycles, this data shows the reduction in damaging stress-range.

3.1.4.1.2 Clear Lake, Iowa. To analyze the effectiveness of strake coverage, an experiment was completed on the IA-N HMLT. Data were collected for a period of time where the HMLT was covered by a full-length double-rope strake, and another period where only the top third was covered. The HMLT has previously been monitored (Connor and Hodgson, 2006) and was known to be susceptible to vortex-induced vibration. Strain gages for this study were placed in the same location as strain gages from the previous study so a direct comparison of the two data sets could be made. No data for the free condition were collected during this study, since it could be incorporated from the previous research. Results of this experiment are presented in Figure 3.13 and Figure 3.14.

Table 3.6. Free (FR) and mitigated (MT) effective stress-range values for WY-CJE.

WY-CJE		CHANNEL							
		1	2	3	4	5	6	7	8
S_{Reff} (ksi)	FR	1.68	1.57	1.44	1.60	1.69	1.58	1.49	1.57
	MT	1.62	1.61	1.58	1.62	1.62	1.62	1.59	1.60

Table 3.7. Free (FR) and mitigated (MT) effective stress-range values for WY-CJW.

WY-CJW		CHANNEL							
		8	1	2	3	4	5	6	7
S_{Reff} (ksi)	FR	1.61	1.73	1.64	1.62	1.60	1.72	1.65	1.60
	MT	1.55	1.59	1.59	1.59	1.57	1.57	1.60	1.57

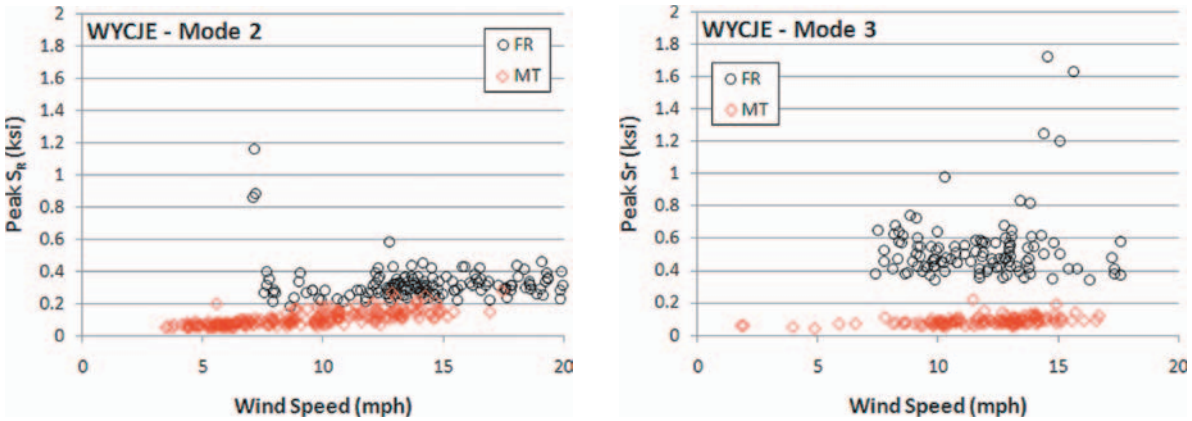

Figure 3.11. Free and mitigated occurrences of across-wind excitation for WY-CJE.

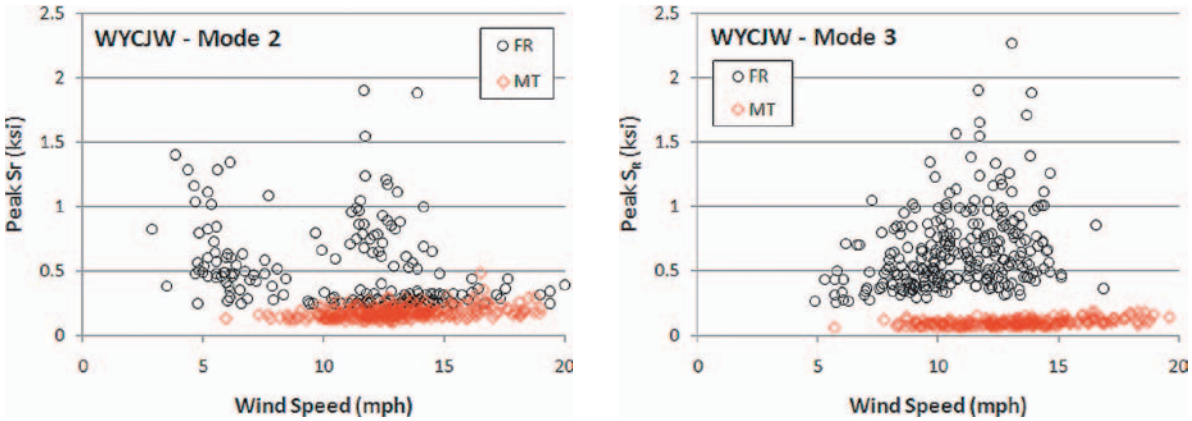

Figure 3.12. Free and mitigated occurrences of across-wind excitation for WY-CJW.

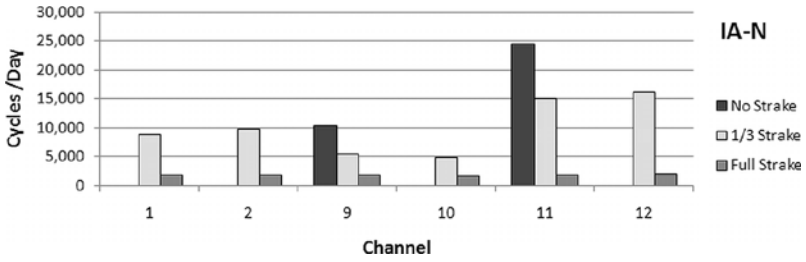

Figure 3.13. Cycle counts for IA-N.

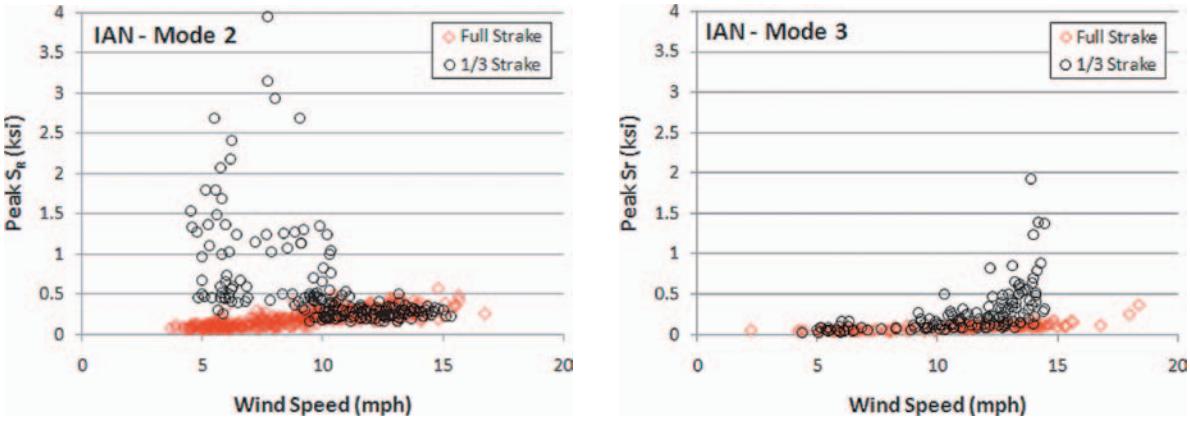

Figure 3.14. Free and mitigated occurrences of across-wind excitation for IA-N.

46 Fatigue Loading and Design Methodology for High-Mast Lighting Towers

Data for the free condition were only available for Channels 9 and 11; Channel 9 represents the along-wind direction, and Channel 11 represents the across-wind direction.

Both figures show that the one-third strake was not as effective at mitigating vortex shedding as the full-length strake. Although the one-third strake did reduce the number of cycle counts as shown in the bar chart, it was not as effective as the full-length strake, indicating vortex shedding still occurred on the lower regions of the pole. Also, it is important to note the full-length strake on the Iowa pole is shown to produce results similar to those obtained in Wyoming. This further suggests the full-length strake is not an anomaly of one type of structure or one specific geographic location but rather something applicable to a variety of structures across the country.

3.1.4.2 Mitigated Fatigue Load Effect

As stated earlier, based on the data collected herein, there is no evidence that the addition of strakes results in generation of larger stress ranges. Mitigation of vortex shedding appears to mainly affect the accumulation of stress cycles. This is illustrated in Figure 3.15, Figure 3.16, and Figure 3.17. Each figure plots normalized histogram data for both the free and mitigated conditions along with best-fit lines. Each histogram can be modeled according to an exponential equation of the type

$$y = Ae^{bx}$$

Equation 3.1: Exponential model for histogram data

where A equals the y-intercept, a parameter representative of the cycle count, and b equals the slope of the line, a parameter related to static pressure-range. In each figure, the slope of the free (FR) and mitigated (MT) data is observed to be roughly parallel, while the mitigated data is clearly offset below the free data to a lower y-intercept.

In addition to the histogram data presented above, the effect of mitigating vortex shedding can be observed by comparing values for the fatigue-limit-state pressure range, constant-amplitude effective pressure-range, and cycle frequency. The values are listed in Table 3.8, Table 3.9, and Table 3.10, along with the ratio of the free to mitigated condition, and a root-mean-square-error

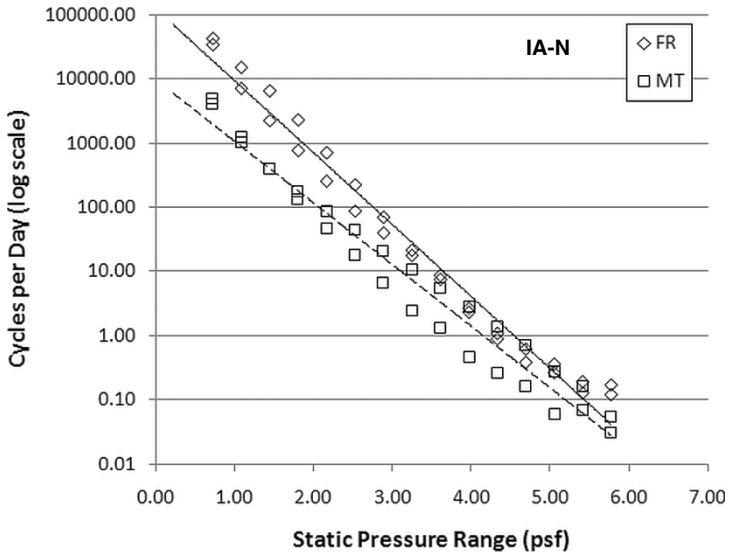

Figure 3.15. Free and mitigated histogram data for IA-N ("free" data from Connor & Hodgson).

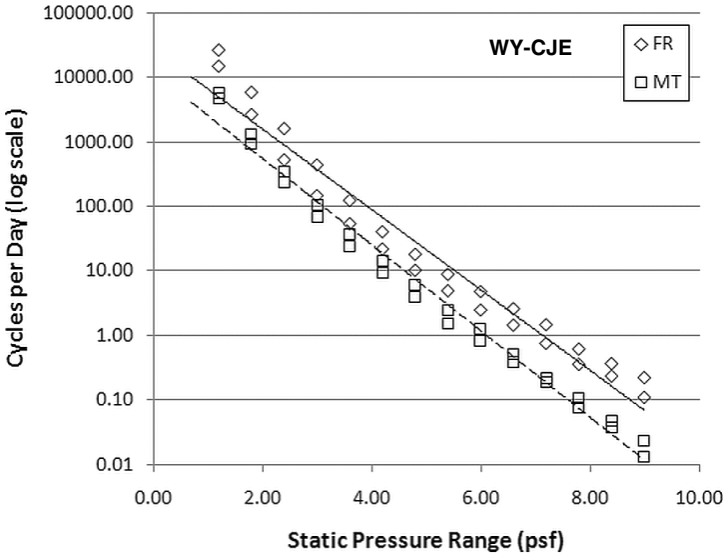

Figure 3.16. Free and mitigated histogram data for WY-CJE.

(RMSE) calculation using an expected value of unity. By comparing the RMSE values, it can be seen that the difference in variation between the load values and the cycle frequency values varies by an order of magnitude. In terms of fatigue load effect, there is little variation in the amplitude of the load applied, but considerable reduction in frequency.

3.2 Results of Aerodynamic Tests

This section encompasses the results found in the aerodynamic studies. One of the interesting results was that the CFD Unsteady Reynolds Averaged Navier Stokes (URANS) Program was not calculating separation well, and change to a large eddy simulation (LES) would need to be pursued.

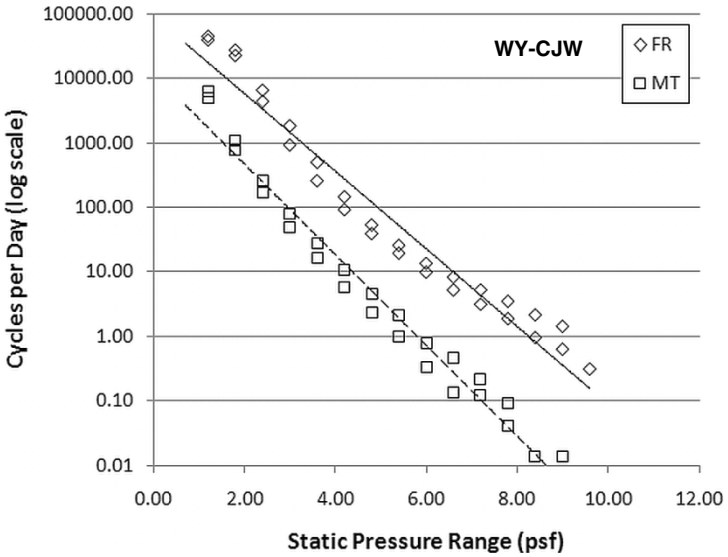

Figure 3.17. Free and mitigated histogram data for WY-CJW.

Table 3.8. Comparison of free and mitigated p_{fls} values.

FATIGUE-LIMIT-STATE PRESSURE RANGE (p_{fls})				
ID	FR	MT	FR/MT	E^2
	(psf)	(psf)		
IAN-A	n/a	4.46	-	-
IAN-X	n/a	3.76	-	-
CJE-A	4.87	5.48	0.889	0.012
CJE-X	5.61	5.60	1.001	0.000
CJW-A	6.12	4.76	1.286	0.082
CJW-X	6.54	4.73	1.381	0.145
			RMSE =	0.245

n/a – data not available in Connor and Hodgson report

E^2 – error calculated using an expected value of unity

Table 3.9. Comparison of free and mitigated p_{eff} values.

CONSTANT-AMPLITUDE EFFECTIVE PRESSURE-RANGE (p_{eff})				
ID	FR	MT	FR/MT	E^2
	(psf)	(psf)		
IAN-A	0.81*	0.98	0.828	0.030
IAN-X	0.92*	0.86	1.068	0.005
CJE-A	1.22	1.30	0.943	0.003
CJE-X	1.29	1.32	0.980	0.000
CJW-A	1.27	1.23	1.028	0.001
CJW-X	1.36	1.23	1.106	0.011
			RMSE =	0.091

* – data from Connor and Hodgson

E^2 – error calculated using an expected value of unity

Table 3.10. Comparison of free and mitigated cycle frequency values.

CYCLE FREQUENCY				
ID	FR	MT	FR/MT	E^2
	(N/day)	(N/day)		
IAN-A	44,054*	5,927	7.43	41.4
IAN-X	66,620*	7,173	9.29	68.7
CJE-A	18,693	6,037	3.10	4.4
CJE-X	35,437	7,598	4.66	13.4
CJW-A	28,228	6,688	4.22	10.4
CJW-X	36,382	6,934	5.25	18.0
			RMSE =	5.1

* – data from Connor & Hodgson

E^2 – error calculated using an expected value of unity

From experiments, there were important findings. The corner upwind configuration is much more prone to lock-in than the face upwind configuration. Another finding was that the size of the vortex cells was much larger than expected, with some cells being 18 inches out of a 60-inch model, almost one-third of the total span-wise length. From the pressure side, the irregular geometry is creating artificial separation areas around corners making the flow separate at an upstream position far away from the expected cylinder case. These results are discussed in the following sections.

3.2.1 Pressure

The results obtained from the pressure scanner show the mean pressure at each of the model faces. The wind tunnel model was rotated so that the pressure taps were at the required location to take the data presented here. This is illustrated in Figure 3.18. In this figure, the first test was taken when the pressure taps are set at the stagnation point, data were taken, then the tunnel was shut off and the model was rotated 45 degrees, data taken again, and so forth. When 180 degrees worth of data were taken, the tests were concluded and the data were compiled. The same procedure was done with the 12- and 16-sided models, but more tests were taken to ensure all face locations were tested at each configuration. Five tests were performed for the 8-sided model to cover 0 to 180 degrees in 45-degree increments. Seven tests were performed for the 12-sided model in 30-degree increments, and nine tests were performed for the 16-sided model in 22.5-degree increments.

Two sets of data were collected for each of the models to check for repeatability. Only the 12-sided model with face upwind configuration will be shown in this section. This model was chosen because it was most prone to oscillate during testing. The other models' data are shown in Appendix I (available on the TRB website).

The data for the face upwind model shown in Figure 3.19 also has experimental pressure data and theoretical inviscid data for a circular cylinder. In Figure 3.19, the non-dimensionalized pressure is shown as a diagram with length-appropriate vectors. This shows the difference in

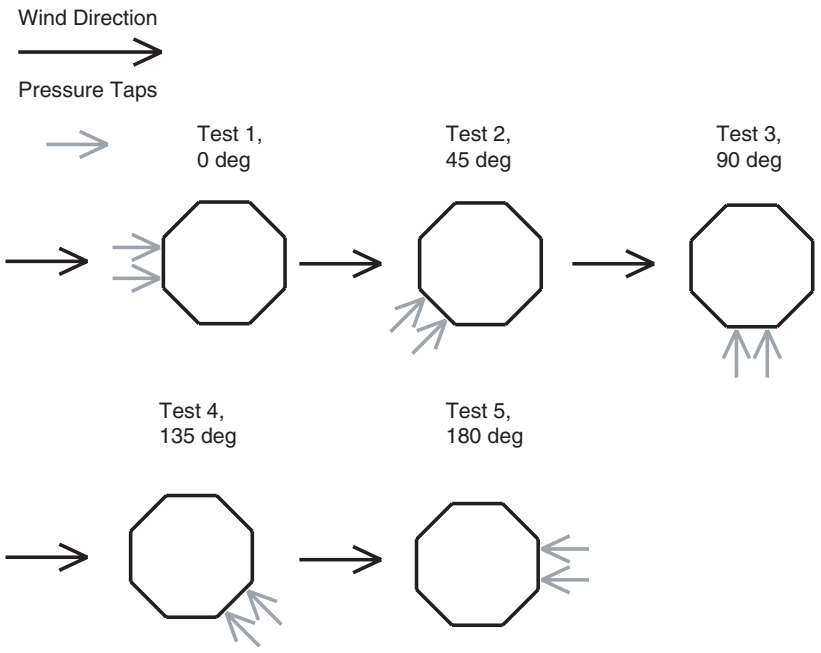

Figure 3.18. Pressure data experimental procedure.

50 Fatigue Loading and Design Methodology for High-Mast Lighting Towers

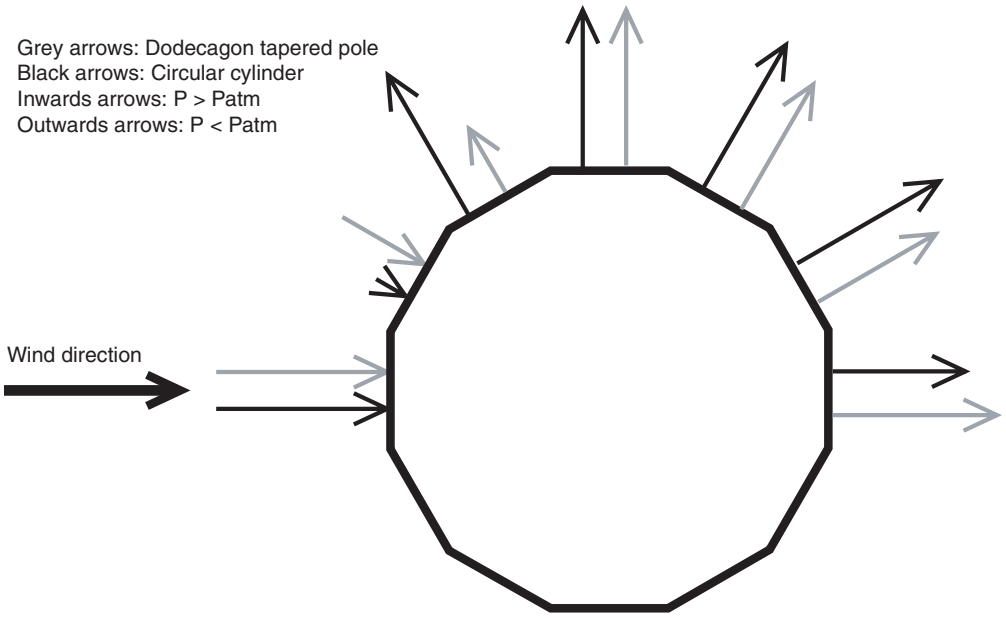

Figure 3.19. Vector plot of pressure data for the 12-sided model and circular cylinder.

pressure between the 12-sided model and the experimental cylinder. The results for the 12-sided model show where separation occurs and how it is different from the circular cylinder case. Separation occurs when the non-dimensionalized pressure vectors start to look the same farther downstream. In this case, the 12-sided cylinder separates at 90 degrees while the circular cylinder separates closer to 60 degrees. The separation for the 12-sided cylinder occurs at a location farther upstream than seen on a constant-taper circular cylinder. This is due to the sharp corners on the model that promote separation at the corner location. (Note that for the real poles, "sharp" corners are not present since there is always some radius at the fold due to the actual fabrication process.) The circular cylinder does not have sharp corners, so the flow doesn't have a discontinuous point that promotes an adverse pressure gradient.

3.2.2 Wake

This section includes a look at some of the data acquired using the hot-wire and traverse system. The hot wires were placed in the wake to check for periodic flow velocity.

3.2.2.1 Data Taking and Signal Conditioning

A multitude of waveforms were taken using the current hot-wire system. The data taking points were organized in a grid pattern as shown in Figure 3.20 and Figure 3.21.

In these two figures, the distance between points in the span-wise direction is 9 inches, and in the cross-flow direction it is 1 inch. The black edges on the outside of Figure 3.20 represent the wind tunnel walls; flow is out of the page. The aforementioned testing pattern aides in checking the data for consistency; as the probe moves to different span-wise locations, different frequencies are captured. When the probe returns to a previous span-wise location (but a different cross-wind location), the frequency should be the same as the data taken in the previous sweep. This proved to be true as long as the data were taken away from the near-model wake in the cross-wind direction (i.e., below the line traced by points 7, 8, 9 in the figures above). To estimate the sampling frequency, a generic value for the Strouhal number of 0.21 was used and

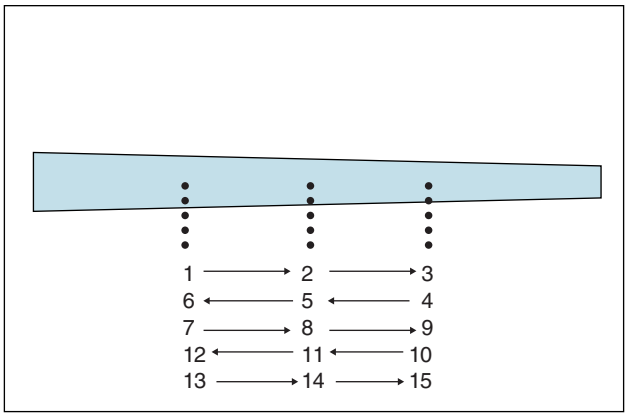

Figure 3.20. Hot-wire testing grid and order of data taking procedure.

the velocity in the tunnel was set to approximately 10 m/s (22.4 mph). This Strouhal number value came from Figure 3.22 for $10^3 < R_e < 10^5$ and the velocity from the geometry and Reynolds number that was expected. The results showed expected frequencies between 15 and 20 Hz for the range of diameters used on the models.

A sample of one of the waveforms can be seen Figure 3.23. The FFTs of the signal were not very clear, so some conditioning was done on the data; the wave was windowed and the mean was subtracted from the value. An FFT before and after clean-up can be seen in Figure 3.24. The post-processing of data shows a sharper frequency peak as well as less noise overall in the rest of the data. All sets of data were processed this way. The windowing function and code can be seen in Appendix I (available on the TRB website).

3.2.2.2 Cross-Wind Study

The results from the hot-wire grid pattern study referenced in the previous subsection are presented in this subsection. After the data were post-processed, the frequency peak on each FFT was plotted against cross-wind position in model diameters as shown in Figure 3.25. This study was done to check that the vortex shedding frequencies were consistent at different cross-wind locations. There are five different cross-wind points and three span-wise points as discussed at the beginning of the chapter. To represent the different span-wise locations, different symbols were used. Three locations were picked, the span-wise center of the model and 9-inch locations to either side of the span-wise center.

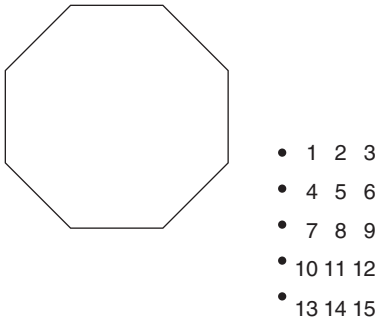

Figure 3.21. Side view of the testing grid–flow is to the right.

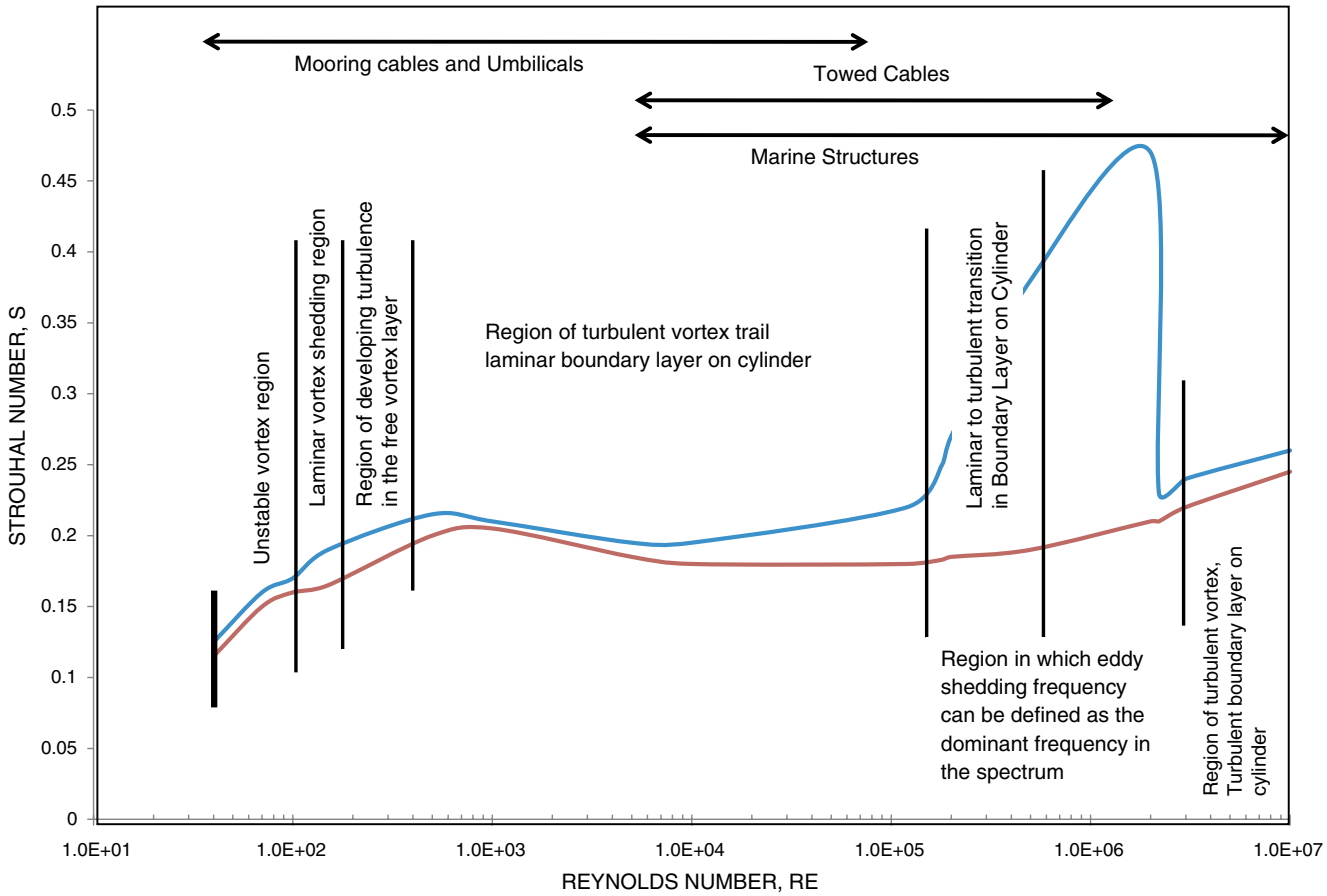

Figure 3.22. Strouhal versus Reynolds number for a circular cylinder with no taper.

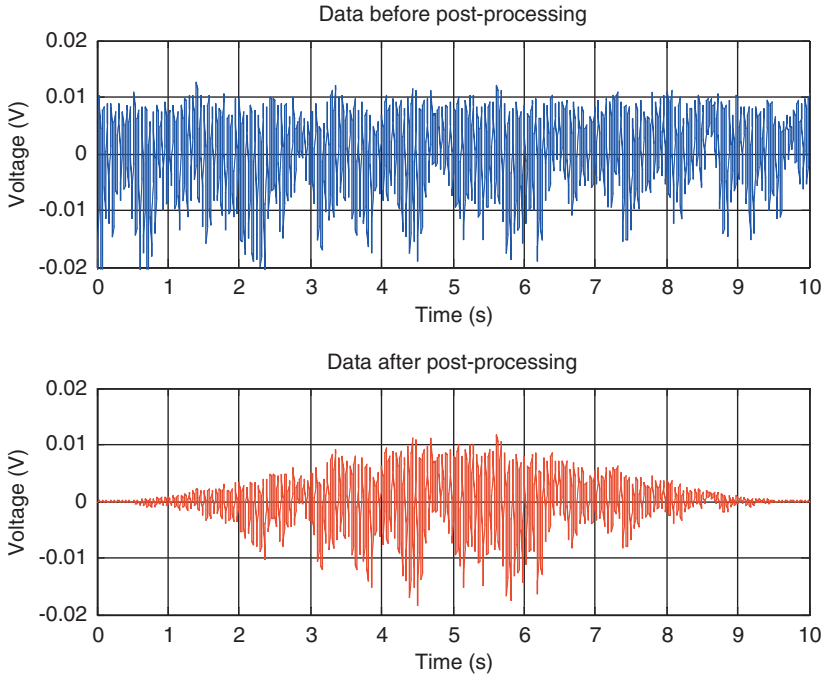

Figure 3.23. Hot-wire signal before and after processing.

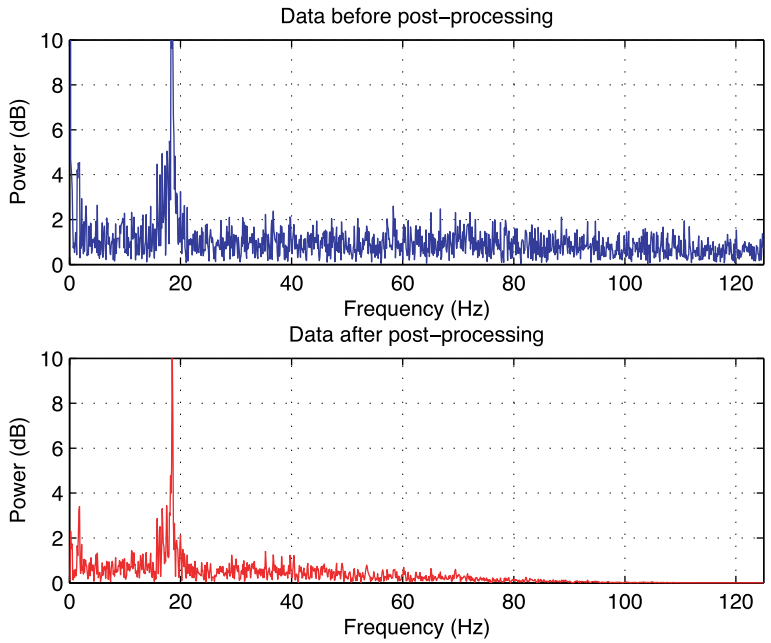

Figure 3.24. Real value of FFTs before and after processing.

Figure 3.25 shows cross-wind frequency data from the face-upwind configuration of the 12-sided model. The same configuration from other models shows the trend shown in Figure 3.25 where the data points are close to 16 Hz as they approach one model diameter distance from the model but are more spread out. If the probe is located closer to the center of the model, the readings are not coherent vortex shedding. When taking data farther than one model diameter from the cross-wind center, the results are the same as those taken near the one model diameter mark. The difference between the data points denoted by the first three symbols in the key to

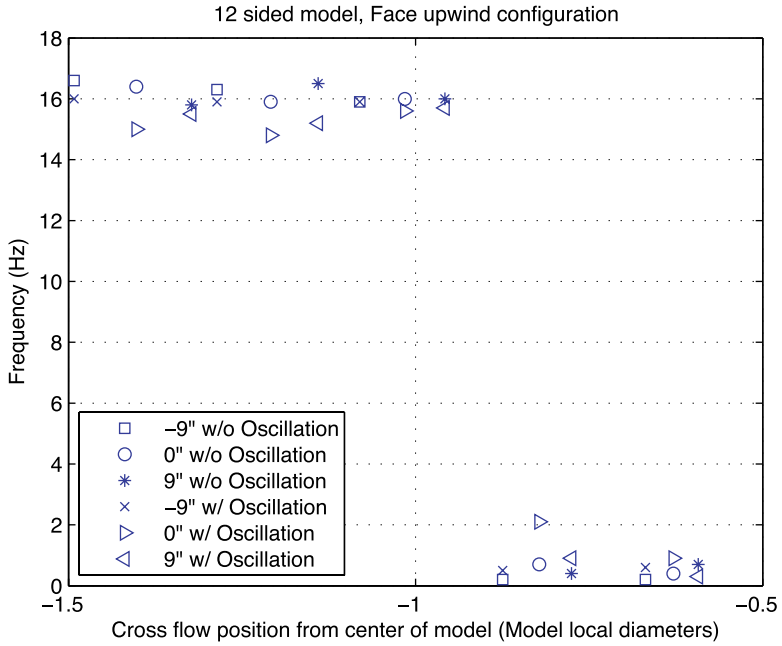

Figure 3.25. Cross-wind frequencies for 12-sided model, face-upwind configuration.

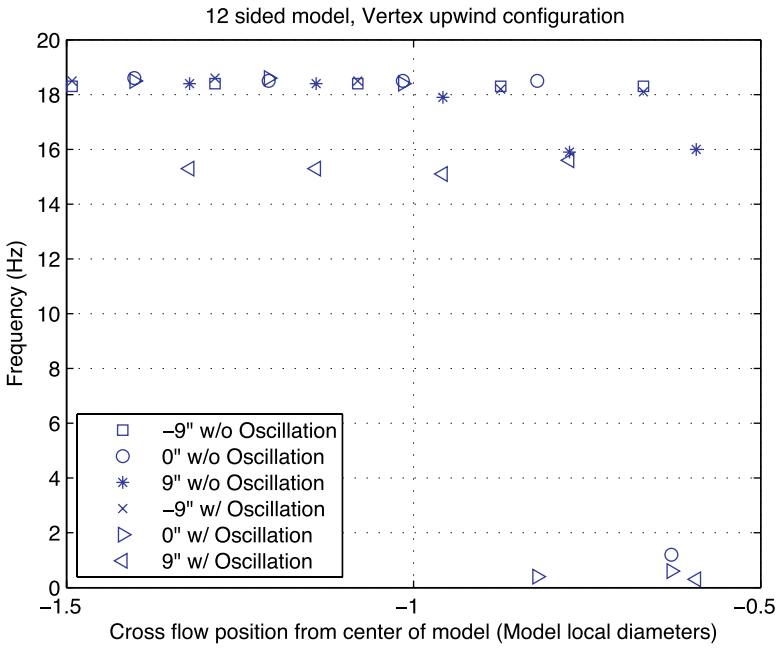

Figure 3.26. Closer frequencies for 12-sided model at different diameters, or "lock-in."

Figure 3.25 and the data points denoted by the last three symbols in the figure's key is that the natural frequency of the system on the first three symbols is much higher than the shed vortices coming off the model. For the data points denoted by the figure's last three symbols, the springs have a natural frequency close to the shedding frequency of the model. It is important to note that at a certain cross-wind distance from the model, some frequencies are very low. This is due to not getting a coherent signal; the data are from one of the recirculation zones on the wake. The hot-wire readings at these locations are not periodic vortex shedding.

According to the Strouhal relation, if the wind velocity is kept constant and the Strouhal number is assumed constant, then as diameter changes, the frequency should change linearly. This is true for a circular cylindrical case as seen in the section on Vortex Shedding. This is readily apparent for this face-upwind configuration. However, this frequency change is not so readily seen in the vertex-upwind configuration shown in Figure 3.26.

The vertex-upwind configuration shows the dominant frequency to be approximately the same for different span-wise configurations. This configuration exhibits "lock-in" for different diameters, showing the same frequency for different diameters. The only parts that show low frequencies are close to the trailing edge to the model inside the recirculation zones. These areas show pure noise and no real coherent signal. This was expected after seeing the results from the face-upwind configuration. The frequencies lining up at one frequency means that the vortices hitting the hot-wire probe have nearly the same frequency and confirms the existence of vortex cells. These cells are necessary to get a uniform excitation frequency on the structure. If the vortex cells' frequency is near the natural frequency of the HMLT pole that means that a portion of the structure is resonating and this resonance can cause an increase in amplitude and a greater potential for fatigue and failure.

3.2.2.3 Signal Partitioning

Another test was performed to check that the shedding frequency is constant in time. That is, a section of the model is not locking on to one frequency and, after a short time, is locking on to another shedding frequency. This would be a shift of the vortex cells through time and an

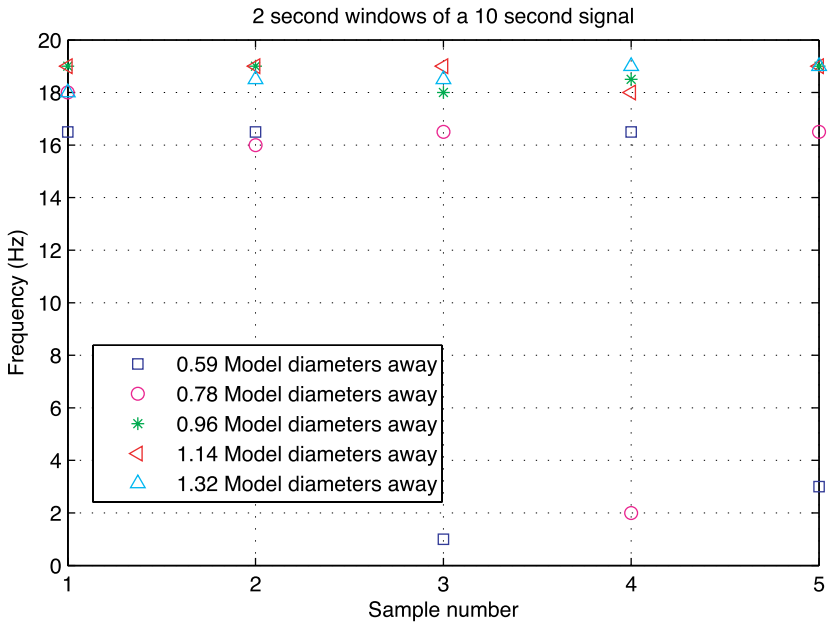

Figure 3.27. Two-second segments of signals.

important result to determine the size of the vortex cells. The results can be seen in Figure 3.27. A cross-wind scan (five 10-second waves taken at different cross-wind locations) was segmented into 2-second windows and the shedding frequencies for each of these 2-second segments was plotted as a "sample." Each cross-wind location thus has five samples that are portrayed as the X-axis in Figure 3.27, the cross-wind location is shown in the legend, and the frequency for each segment corresponds to the data point's location on the Y-axis.

As Figure 3.27 shows, for the most part, the 2-second windows have approximately the same results for the waves that are farther away from the model. The data taken closer to the model's center (with respect to the cross-wind direction) exhibit a large discrepancy, sometimes giving an incorrect frequency. This is due to the nature of the inner wake where the data are scattered and full of noise due to the recirculation zones on the trailing edge of the model. These results have confirmed that as long as the probe is far enough away from the inner wake of the model, the data acquired will be useful and repeatable for this study. This study means that the readings at each location, except the ones too close to the model, are repeatable and are not jumping between frequencies.

3.2.3 Smoke Wand

The smoke wand study was used initially to find a good cross-wind location to take hot-wire data. Data were taken at this location, but later the cross-wind study used for Section 3.2.2, Wake, was done to check for consistency. The shear layer separates at approximately the 45-degree location, however the oscillations are at a frequency between 15 and 20 Hz and very low amplitude so they cannot be seen in any of the smoke wand pictures. This separation location appears to be the same as the pressure data suggest.

3.2.4 Computational Fluid Dynamics

The computational fluid dynamics models were done as a way to check separation surfaces using a standard URANS on the program FLUENT, anything more complex than 2-D is suspect since there is a range of magnitudes that would require an extremely large amount of grid points.

56 Fatigue Loading and Design Methodology for High-Mast Lighting Towers

To put this in perspective, the boundary layer may be ½-inch thick (and you need 10 points in it to calculate separation) and the pole is up to 160 feet tall. The amount of points it would take would be a stretch; the whole experiment time would have to be devoted to this endeavor. However, a 2-D model can be used to check general separation locations.

The Cfdesign software provided limited results. It showed certain low-pressure areas correctly and seemed to predict an "updraft" (a span-wise flow due to the taper on the structure). The software used organic meshing, creating its own mesh with certain input parameters from the user.

The FLUENT CFD model showed separation further downstream than was seen on the experimental model for every case. These models are URANS calculations and may not take into account surface roughness or other factors. Separation has traditionally been an issue in CFD modeling. In all, the CFD modeling could be done using large eddy simulation (LES) for greater turbulent accuracy, but this would have to be done as a future study.

3.3 Development of Proposed Specification

The proposed specification changes developed herein perpetuate the method of infinite life design for HMLTs while redefining the fatigue design load. A "combined wind effect," a new loading concept, is introduced as part of the proposed specification. This new load more realistically mimics the loading of an in-service structure by combining the effects of buffeting and vortex shedding into a single load. The proposed specification also considers variation of mean wind speed and gives designers the ability to select a design pressure based on local wind data. Changes to the fatigue importance categories also have been made in the proposed specification. Using the importance categories, consequence of failure is considered based on HMLT proximity to the roadway.

3.3.1 Fatigue Design Life

The stress-range histogram data collected through this study diminish the uncertainty in the number of lifetime loading cycles for a given HMLT and have established that the number of loading cycles is well beyond the limiting number of cycles at the constant-amplitude fatigue limit (CAFL). Table 3.11 demonstrates the need to use infinite life design for HMLTs. For each channel considered, critical detail categories were selected for comparison such that the CAFL exceeds the fatigue-limit-state stress range (S_{Rfls}), which is the minimum stress-range used to achieve infinite life. Then, the limiting number of cycles (N_{lim}) was determined for the detail based on the appropriate S-N curve and compared to the total expected number of cycles (N_{total}) for a 50–year life. This process was carried out for three different truncation levels assuming the selected CAFL is the maximum anticipated stress-range regardless of truncation level. For most cases, infinite life design is required.

Where an HMLT has not entered the infinite life regime, it does not necessarily imply finite life: the detail may be altered, thereby increasing the critical fatigue stress-range and decreasing the limiting number of cycles for infinite life. For the instances where infinite life is not required, the sites are observed to exhibit either low demand in terms of cycle counts, or a high fatigue resistance, each resulting in low S_{Rfls} values. For example, prior to monitoring, the IA-S HMLT was retrofitted with a 0.625-inch-wall tubular pole section that drastically reduced the observed stress-range data. (The retrofit was not part of this study but a strategy undertaken by Iowa DOT as part of a separate project.) This reduction results in a conservative critical detail category and has a significant effect on N_{total} with increased truncation. The ND HMLT has a similarly high fatigue resistance with a 0.438-inch wall. Together, the IA-S and ND HMLTs were the stiffest in

Table 3.11. Determination of infinite life based on study data.

	TRUNCATION LEVEL			NONE*		> 0.50 ksi		> 1.0 ksi	
ID	S_{Rfls}	DETAIL	N_{limit}	N_{Total}	INF. LIFE	N_{Total}	INF. LIFE	N_{Total}	INF. LIFE
	(ksi)	CAT.	@ CAFL		REQUIRED?		REQUIRED?		REQUIRED?
CA-A	5.76	D	6.4E+06	2.8E+08	Yes	1.1E+08	Yes	3.3E+07	Yes
CA-X	4.51	D	6.4E+06	3.0E+08	Yes	9.2E+07	Yes	2.3E+07	Yes
IAN-A (MT)	6.17	D	6.4E+06	2.6E+08	Yes	1.1E+08	Yes	3.3E+07	Yes
IAN-X (MT)	5.21	D	6.4E+06	3.2E+08	Yes	1.3E+08	Yes	3.7E+07	Yes
IAS-A	3.24	E	1.2E+07	1.9E+08	Yes	5.1E+07	Yes	6.5E+06	*No*
IAS-X	2.87	E	1.2E+07	2.5E+08	Yes	6.3E+07	Yes	6.4E+06	*No*
KS-A	7.17	C	4.4E+06	6.0E+08	Yes	2.3E+08	Yes	8.4E+07	Yes
KS-X	7.73	C	4.4E+06	7.2E+08	Yes	2.6E+08	Yes	1.0E+08	Yes
ND-A	3.54	E	1.2E+07	2.9E+08	Yes	8.3E+07	Yes	1.1E+07	*No*
ND-X	3.87	E	1.2E+07	3.3E+08	Yes	1.1E+08	Yes	2.0E+07	*Yes*
OKNE-A	4.58	D	6.4E+06	4.2E+08	Yes	1.5E+08	Yes	3.5E+07	Yes
OKNE-X	4.19	E	1.2E+07	4.8E+08	Yes	1.6E+08	Yes	3.4E+07	Yes
OKSW-A	4.45	E	1.2E+07	7.2E+08	Yes	2.6E+08	Yes	5.8E+07	Yes
OKSW-X	4.61	D	6.4E+06	8.7E+08	Yes	3.1E+08	Yes	7.0E+07	Yes
PA-A	2.32	E'	2.2E+07	5.2E+07	Yes	5.4E+06	*No*	2.9E+05	*No*
PA-X	2.23	E'	2.2E+07	8.8E+07	Yes	8.1E+06	*No*	6.1E+05	*No*
SD-A	3.40	E	1.2E+07	5.8E+08	Yes	2.1E+08	Yes	2.7E+07	Yes
SD-X	3.74	E	1.2E+07	6.3E+08	Yes	2.3E+08	Yes	3.3E+07	Yes
CJE-A (FR)	4.06	E	1.2E+07	1.0E+09	Yes	3.4E+08	Yes	6.3E+07	Yes
CJE-X (FR)	4.68	D	6.4E+06	1.7E+09	Yes	6.5E+08	Yes	1.5E+08	Yes
CJE-A (MT)	4.57	D	6.4E+06	2.8E+08	Yes	1.1E+08	Yes	2.5E+07	Yes
CJE-X (MT)	4.67	D	6.4E+06	3.6E+08	Yes	1.4E+08	Yes	3.3E+07	Yes
CJW-A (FR)	5.10	D	6.4E+06	1.2E+09	Yes	5.2E+08	Yes	1.0E+08	Yes
CJW-X (FR)	5.45	D	6.4E+06	1.5E+09	Yes	6.6E+08	Yes	1.7E+08	Yes
CJW-A (MT)	3.97	E	1.2E+07	3.1E+08	Yes	1.2E+08	Yes	2.3E+07	*Yes*
CJW-X (MT)	3.95	E	1.2E+07	3.2E+08	Yes	1.3E+08	Yes	2.3E+07	*Yes*

N_{Total} values based on 50-year design life.

*All stress-range data collected was automatically truncated at 0.25 ksi.

the study. For the PA HMLT, two factors allow for finite life: low demand and a unique inner reinforcing sleeve. In addition, the IA-S and PA HMLTs have relatively short intervals of data collection, which may skew the results with regard to expected life.

3.3.2 Fatigue-Limit-State Pressure Range

Consequence of failure is currently incorporated into the specification through the use of Fatigue Importance Categories. The concept of "importance" allows owners to adjust the level of structural reliability of sign, signal, and lighting structures based on individual design conditions. Currently, the specification commentary recommends most HMLTs be considered Category I, the most conservative importance category. However, conditions such as distance to roadway and installation of effective vibration mitigation devices can affect the consequence of failure and structural reliability, respectively. Although the mitigation strategy previously

58 Fatigue Loading and Design Methodology for High-Mast Lighting Towers

discussed is effective and would result in a more reliable design, the research team believes that further study is needed to assess the effect of all potential mitigation devices prior to explicitly considering them for the design of *new* poles. Mitigation methods, for both disrupting vortex shedding and damping out vortex-induced vibrations, should be examined in more detail. For this reason, the proposed importance categories do not yet consider mitigation as a method of explicitly increased reliability. Decisions are based solely on consequence of failure.

This study divides consequence of failure of HMLTs into the following two outcomes:

1. **Low risk to traffic,** where the distance from edge of the roadway to the HMLT is greater than the height of the HMLT and
2. **High risk to traffic,** where the distance from edge of roadway to HMLT is less than the height of the HMLT.

It is recognized that application of this provision could result in different HMLTs being designed for different fatigue loads at the same interchange, depending on the consequence of failure. Although this may not seem to be worth the effort in design, it could result in more economical structures or, more importantly, encourage designers to place the structures in locations where the risk is less. Proposed importance categories for HMLTs are presented in Table 3.12.

The proposed combined wind effect is directly related to the fatigue-limit-state pressure-range by the following expression:

$$P_{CW} = P_{FLS} C_d$$

Equation 3.2: Combined wind effect

where P_{CW} is the combined wind effect pressure-range, P_{FLS} is the fatigue-limit-state pressure range, and C_d is the AASHTO drag coefficient. Calculated fatigue-limit-state static pressure-ranges based on histogram data and corresponding measured mean wind speed values are tabulated in Table 3.13. Note, the measured mean wind speed values presented are independent of the velocity range values listed in previous tables, which are derived from stress-range histogram data. The highlighted values exceed the current equivalent static natural wind gust pressure-range set forth in Equation 11-5 of AASHTO Signs (2009), which equals 5.2 psf when C_d and I_F are both equal to 1. The data are plotted in Figure 3.28 along with curves for Equations 11-5 and C11-5 (AASHTO, 2009). From this graph, it is apparent that the upper bound limit and the existing "adjustment" equation accounting for yearly mean wind velocity are unconservative in many cases.

The pressure-range histogram data in Figure 3.6 are shown to vary with mean wind speed, and the same is true for the fatigue-limit-state pressure range values. To account for variation in wind speed, a linear model was fit to the data representing the mean pressure-range. That line was then offset two standard deviations to form an upper bound accounting for all other variation in HMLT geometry, HMLT details, topographic effects, etc. The upper-bound static pressure-range is plotted

Table 3.12. Proposed fatigue importance categories for HMLTs.

TRAFFIC RISK?	IMPORTANCE CATEGORY
HIGH	I
LOW	II

Table 3.13. Fatigue-limit-state pressure-range and recorded mean wind speed.

ID	WS_{mean} (mph)	P_{fls} (psf)
CA-A	8.7	4.6
CA-X	8.7	3.6
IAS-A	10.3	6.1
IAS-X	10.3	5.4
KS-A	9.4	5.0
KS-X	9.0	5.3
ND-A	6.7	4.0
ND-X	6.7	4.3
OKNE-A	6.8	3.7
OKNE-X	6.8	3.4
OKSW-A	8.3	2.9
OKSW-X	8.8	3.0
PA-A	3.5	2.6
PA-X	3.5	2.5
SD-A	7.8	2.8
SD-X	7.8	3.1
CJE-A (FR)	12.8	4.9
CJE-X (FR)	12.8	5.6
CJW-A (FR)	14.0	6.1
CJW-X (FR)	14.0	6.5

with the fatigue-limit-state data in Figure 3.29. To determine the proposed P_{FLS} values, the variation in measured mean wind speed is divided into the following three outcomes:

1. Location-specific yearly mean wind velocity is less than national average,
2. Location-specific yearly mean wind velocity is greater than national average but less than the yearly mean wind velocity with 16 percent exceedance (one standard deviation), and
3. Location-specific yearly mean wind velocity is greater than 16 percent exceedance.

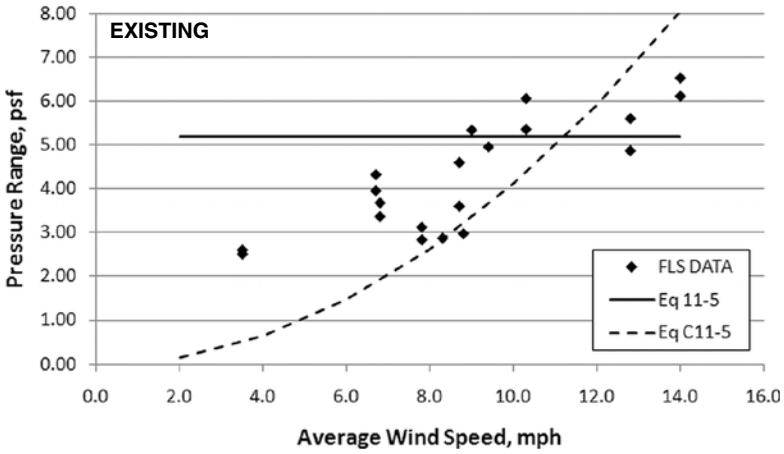

Figure 3.28. Plot of fatigue-limit-state data against existing specification equations.

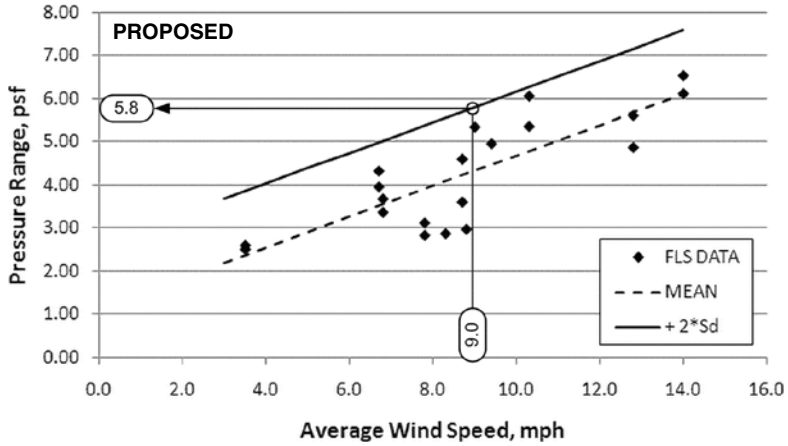

Figure 3.29. Plot of fatigue-limit-state data and proposed upper boundary.

The 16 percent exceedance level is the upper bound previously set by *NCHRP Report 412* (1998) and corresponds to approximately 11 mph. By finding the intersection of the national average yearly mean wind velocity with the measured upper-bound pressure-range from this study, a proposed minimum design pressure-range of 5.8 psf was set.

The national wind data used to determine pressure-range values from the upper bound are provided in the report "Comparative Climatic Data for the United States through 2010" published by the National Climatic Data Center, a division of NOAA (2010). This is a more current and comprehensive set of data than used in the work performed in the mid 1990s during the preparation of *NCHRP Report 412* (1998). Annual mean wind velocities from 238 stations in the lower 48 states were considered. Data from Alaska, Hawaii, and U.S. territories were specifically excluded because of the tendency for higher annual wind speed at coastal and island stations. From the data set, the national average yearly mean wind velocity is 9.0 mph, the yearly mean wind velocity with 16 percent exceedance is 10.9 mph (11 mph for simplification), and the yearly mean wind velocity with 2 percent exceedance is 12.8 mph. A wind contour map from the National Climatic Data Center is shown in Figure 3.30.

A design equation similar to equation C11-5 (AASHTO, 2009), which allows designers to vary static wind pressure based on the location-specific mean wind velocity, is not recommended for design of HMLTs. Three issues prevent recommending this approach for the proposed revisions.

1. The measured fatigue-limit-state data do not easily fit a parabolic curve through the origin like equation C11-5 suggests. Hence, the equation is inaccurate in "scaling" actual response to various mean wind speeds.
2. Considerable variation exists in the local measured wind speed data collected in this study when compared to wind velocity data provided by NOAA (2010). It is recognized that the NOAA data is from a more comprehensive study of wind across the country. As a result, the measured mean wind speed for a given HMLT in this study may vary significantly from those suggested in the contour map at the same location. Although they may be reasonable overall, adjusting the suggested wind speed solely on the contour map implies a level of accuracy not justified by this study.
3. Additional variation exists due to topographical effects and site-specific details encountered at the long-term monitoring sites. For example, the difference in mean wind speed noted at the two Oklahoma HMLTs is likely due to differences in elevation, location at the highway interchange, and/or blockages near the structure such as trees.

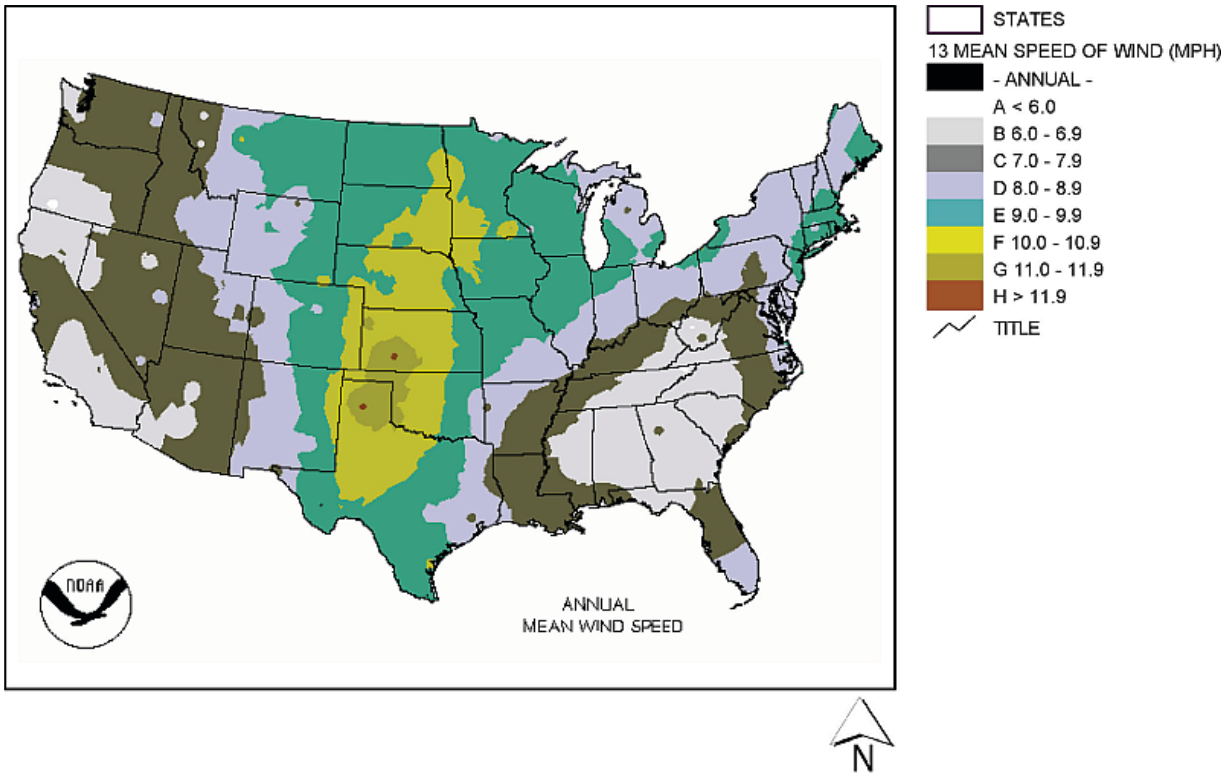

Source: NOAA National Climatic Data Center, http://www.ncdc.noaa.gov/oa/ncdc.html

Figure 3.30. NOAA annual mean wind speed contour map (2010).

Therefore, a means to adjust the design pressure-range based on yearly mean wind velocity is proposed using a three-tiered approach. Rather than scale entirely on the local wind speeds measured herein, it is proposed to scale on the readily available NOAA data, but in a much coarser fashion than the existing AASHTO Signs Commentary section provides. Although the local mean wind speed measured by this project does not always compare well with the data available from NOAA, histogram data do confirm that as the average wind speed increases, the fatigue-limit-state pressure range for a given HMLT also increases. Again, the level of accuracy suggested by the existing commentary, scaling directly on yearly mean wind velocity, is not justified.

The proposed minimum fatigue-limit-state pressure range (P_{FLS}) is based on the national average yearly mean wind velocity of 9 mph. This corresponds to a P_{FLS} value of 5.8 psf. If the yearly mean wind velocity is greater than 9 mph, but less than 11 mph (i.e., within one standard deviation from the national mean wind speed), the P_{FLS} is increased to 6.5 psf. If the yearly mean wind velocity is greater than 11 mph (i.e., greater than one standard deviation away from the mean), the P_{FLS} is further increased to 7.2 psf. As stated, this is different than the existing method as it does not attempt to "split hairs" regarding the estimate of the location-specific yearly mean wind velocity. The three possible P_{FLS} outcomes are presented in Table 3.14 according to the applicable yearly mean wind velocity. In summary, the proposed P_{FLS} values of 5.8, 6.5, and 7.2 psf are based on yearly mean wind velocities of 9, 11, and 13 mph, respectively.

However, designers should be cautioned on the effects of topography and site-specific wind effects when considering location-specific mean wind velocity in their design. For example, take the data measured at the Pennsylvania HMLT and compare it to what a designer would use based on the NOAA map and proposed static pressure-range values. The NOAA contour map suggests the Pennsylvania location would be subjected to a greater mean wind speed. However,

62 Fatigue Loading and Design Methodology for High-Mast Lighting Towers

Table 3.14. Proposed static pressure-range values.

YEARLY MEAN WIND VELOCITY, V_{mean}	PROBABILITY BASED ON V_{mean}	P_{FLS} (psf)
$V_{mean} \leq 9$ mph	50%	5.8
9 mph < $V_{mean} \leq 11$ mph	34%	6.5
$V_{mean} > 11$ mph	16%	7.2

the HMLT in Pennsylvania was largely shielded by local terrain and trees, which is likely the reason the mean wind speed shown in Table 3.13 was much lower than the NOAA contour. In contrast, the Wyoming site recorded average wind speeds exceeding those suggested by the NOAA contour map. However, the topography around the Wyoming sites was open with little obstruction. Further, it is highly unlikely one of the 238 NOAA monitoring stations was located near Creston Junction; thus, it was smeared into the contours of the nearest recording stations. Additionally, it should be noted that it **is not** appropriate to use a value less than 5.8 psf where the yearly mean wind velocity is shown to be less based on the NOAA map. The minimum pressure is based on the mean wind speed and helps to account for any local effects unknown to the designer.

A comparison of experimental data with the proposed method is presented in Table 3.15. Measured mean wind speed data are listed side by side with estimated yearly mean wind velocities from the NOAA contour map. The highlighted values show where experimental values are unconservative compared with the map. Measured P_{fls} values are listed side by side with proposed

Table 3.15. Comparison of experimental data with proposed method.

ID	WS_{mean} (mph)	NOAA (mph)	MEAS. P_{fls} (psf)	PROP. P_{FLS} (psf)
CA-A	8.7	8-9	4.6	5.8
CA-X	8.7		3.6	
IAS-A	10.3	9-10	6.1	6.5
IAS-X	10.3		5.4	
KS-A	9.4	10-11	5.0	6.5
KS-X	9.0		5.3	
ND-A	6.7	9-10	4.0	6.5
ND-X	6.7		4.3	
OKNE-A	6.8	9-10	3.7	6.5
OKNE-X	6.8		3.4	
OKSW-A	8.3	9-10	2.9	6.5
OKSW-X	8.8		3.0	
PA-A	3.5	9-10	2.6	6.5
PA-X	3.5		2.5	
SD-A	7.8	9-10	2.8	6.5
SD-X	7.8		3.1	
CJE-A (FR)	12.8	9-10	4.9	6.5
CJE-X (FR)	12.8		5.6	
CJW-A (FR)	14.0	9-10	6.1	6.5
CJW-X (FR)	14.0		6.5	

P_{FLS} values. Even though the wind speed values don't always match, a conservative design value is determined for each HMLT.

The two possible outcomes for importance category and three possible outcomes for yearly mean wind velocity combine to make a total of six possible outcomes. To incorporate consequence of failure into the proposed design method, it is proposed that HMLTs presenting a high risk to traffic be restricted from using the lowest pressure-range value of 5.8 psf. A high risk to traffic was defined by the researchers as any HMLT that could actually fall into the path of traffic. Such a structure is proposed to be classified as Category I.

It was felt that poles that could fall into the path of traffic should be designed with a higher probability of survival than is associated the mean wind speed (i.e., a 50-50 chance of exceedance). As a result, it was decided that for structures classified as Category I, increasing the P_{FLS} by one standard deviation provided sufficient reliability. Hence, the intermediate P_{FLS} value of 6.5 psf would then be required for HMLTs located where the mean wind speed is 9 mph or less, but classified as Category I. However, for poles located where the mean wind speed is greater than 9 mph, the research team decided that further increases in the design value for P_{FLS} were not warranted. This decision is based both on engineering judgment and the approach contained in the fatigue loading provisions developed during the research for *NCHRP Report 412*. Rationale for the proposed approach follows.

> Both the Category I fatigue importance factor of 1.0, and the wind gust pressure-range set by *NCHRP Report 412* are set at the same confidence limit and correspond to a yearly mean wind velocity of 11 mph. This velocity is consistent with wind that is the speed used to develop the P_{FLS} of 6.5 psf. The reduced probability of failure associated with one and two standard deviations from the mean P_{FLS} value was felt to be already conservatively set as they are based on the worst-case response of all poles instrumented.

It is recognized that the above approach is somewhat arbitrary; it is felt to adequately address the risk associated with a majority of poles. Further adjustments as a function of ADT or ADTT do not appear warranted at this time as insufficient data exist to set such limits. Rather, the simple check of whether an HMLT can fall into the path of traffic is a straightforward and sufficient criterion. The P_{FLS} values proposed for design are presented in Table 3.16.

The proposed approach provides a reasonable and familiar method of accounting for local conditions and consequence of failure without implying a level of accuracy that is not justified. It is noted that fatigue importance *factors* are conspicuously missing. It is noted that the proposed method of accounting for consequence of failure is not based on a quantitative reliability analysis, which was outside the scope of this study, but from qualitative assessment of the current state of HMLT design. In other words, if the HMLT can fall into the path of traffic, the research team felt that it should meet a higher standard, and hence a higher load range is suggested.

One final attractive option of the proposed approach is that state DOTs could easily specify which static pressure-range and/or importance factor should be used in their state, either regionally or for the entire state, to further simplify the approach.

Table 3.16. Proposed P_{FLS} values for design (psf).

FATIGUE-LIMIT-STATE PRESSURE RANGE, P_{FLS} (psf)		
YEARLY MEAN WIND VELOCITY, V_{mean}	IMPORTANCE CATEGORY	
	I	II
$V_{mean} \leq 9$ mph	6.5	5.8
9 mph < $V_{mean} \leq 11$ mph	6.5	6.5
$V_{mean} > 11$ mph	7.2	7.2

3.4 Large-Amplitude Oscillation

Over the course of this study, a YouTube video surfaced, which recorded the behavior of an HMLT outside of Watertown, South Dakota, during a late winter storm. A passing motorist shot the video, which shows the HMLT experiencing *extreme* displacements in the first mode of vibration. It can be viewed at http://www.youtube.com/watch?v=2wpc8qD6AtI. Wind speed that day was estimated to be 30 to 40 mph with higher gusts. Later investigation found the pole to be cracked near the base, and it was promptly taken out of service.

Unfortunately, the HMLT in the video was not part of the long-term monitoring study, so no data are available for that particular event. However, the research team searched through collected trigger data, data that was specifically recorded during periods of high wind speed, for any instances of behavior similar to that shown in the video. Two instances were found that may exhibit similar behavior, one at the WY-CJW HMLT in Creston Junction, Wyoming, and the other at the SD HMLT in Rapid City, South Dakota. Both experienced sustained Mode 1 oscillation at stress ranges of approximately 10 ksi for a duration of 3 minutes or more. Both instances occurred during sustained winds of approximately 30 mph, and the movement appears to be across-wind. Data for the WY-CJW event are presented in the following figures.

Figure 3.31 shows a stress-time plot for one of the channels and illustrates the sustained harmonic motion. Figure 3.32 is a close-up of the same plot and illustrates the Mode 1 behavior at 0.35 Hz and maximum stress of about 10 to 11 ksi. The estimated dynamic displacement for this magnitude of stress is 3 feet in one direction or about 6 feet of total travel at the luminaire. Figure 3.33 shows a plot of the wind speed for the event at a 3-second average, which is a common averaging time for wind gusts. The mean wind speed over the entire duration is about 32 mph. Also note that the HMLT did not have any strakes installed at the time that the large-amplitude oscillations were recorded. The WY-CJE did have strakes installed, but did not exhibit the same behavior; this may be a coincidence.

With regard to fatigue, this phenomenon is a matter of concern; it may be responsible for low-cycle fatigue behavior leading to collapse or significant cracking. If the two instances of large-amplitude oscillation mentioned above truly match the behavior in the video, then it is encouraging to know that it is extremely rare, exceeding the 1:10,000 fatigue-limit-state threshold. Also, the two instances of large-amplitude oscillation are theoretically part of the loading spectrum used to create the proposed fatigue design loads. However, without fully understanding the phenomena responsible for this type of behavior and without stochastic data related to how often it may occur, it is impossible to safeguard against it in a specification.

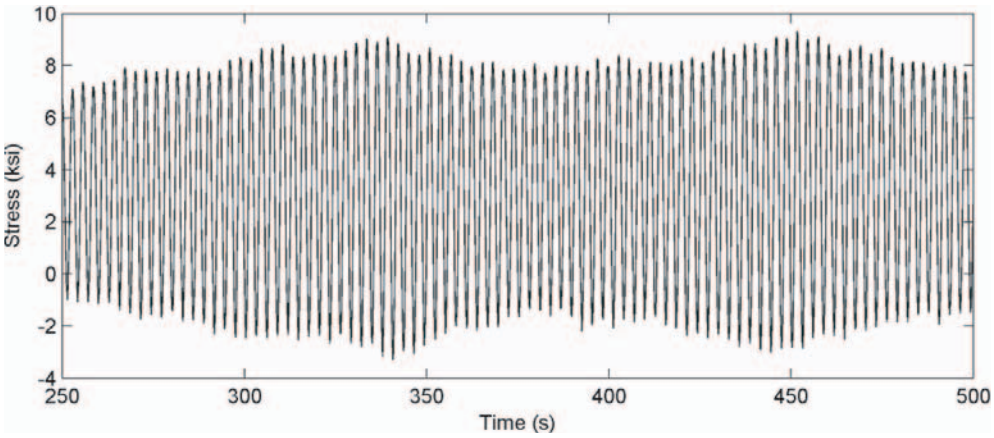

Figure 3.31. Large-amplitude oscillation at WY-CJW.

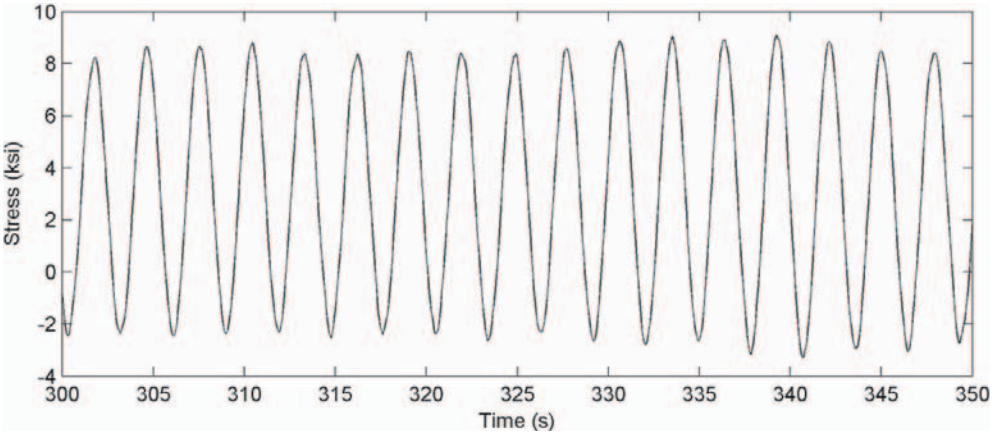

Figure 3.32. Close-up of same large-amplitude oscillation.

At this time, the research team can only speculate on the phenomena responsible for this type of behavior. It certainly warrants future research.

3.5 Fatigue Life Evaluation of Existing HMLTs

The intention of the proposed fatigue provisions is to provide for infinite life design. For new structures, this is appropriate and economical. However, recent failures and subsequent research shows that, for many existing structures, guidance on how to estimate the remaining fatigue life is needed. The procedures contained herein provide such guidance. These procedures are equally applicable for finite life design of new HMLTs in cases where such an approach is warranted.

The first step in evaluating an existing HMLT is to determine whether infinite life is achieved using the appropriate proposed fatigue-limit-state pressure range (i.e., 5.8, 6.5, or 7.2 psf). Although an existing HMLT may have originally been designed for infinite life using the earlier AASHTO Signs provisions, the pole may not meet the proposed (NCHRP Project 10-74) provisions. There are three primary reasons this may be the case, as follows:

1. It is likely that the original design used an unconservative fatigue load. Assuming the proposed 6.5 psf fatigue-limit-state load will apply to most HMLTs, the 5.2 psf load in the current edition

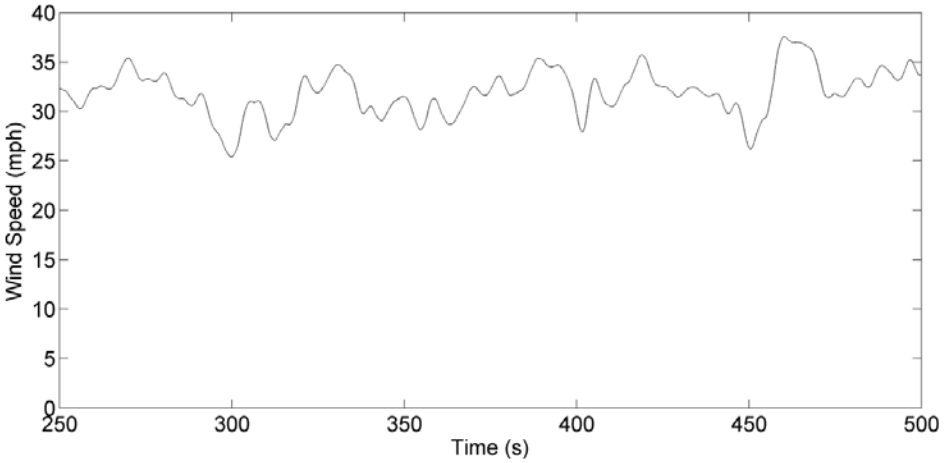

Figure 3.33. Plot of 3-second wind speed during large-amplitude event.

66 Fatigue Loading and Design Methodology for High-Mast Lighting Towers

of AASHTO Signs (2009) is obviously less. Hence, depending on how "overdesigned" the pole was, it will likely not meet the proposed specification.
2. It has been observed that in many cases, older designs often assumed a higher fatigue category for a given detail, in particular the baseplate detail, than is actually the case. The wealth of information relating to cracking in HMLTs (Dexter, 2004; Connor and Hodgson, 2006) supports this.
3. The pole was designed and built before any fatigue provisions were included in AASHTO Signs.

For infinite life design to be valid, applied loading cycles must not exceed the CAFL 99.99 percent of the time, or, in other words, the 1:10,000 confidence limit of the applied loading spectrum must be at or below the CAFL. This load is referred to as the fatigue-limit-state pressure range. To check for infinite life, the stress-range due to the fatigue-limit-state load, S_{Rfls}, must be less than the CAFL.

In addition to the calculation described above, a qualitative approach also may be used to determine whether the HMLT is subject to a finite fatigue life. Through several research programs and field observations, certain criteria have been identified that may alert an owner that finite life is likely for an existing HMLT. An owner may wish to consider finite fatigue life for any of the following reasons:

1. A fillet-welded socket-type tube-to-base-plate connection,
2. Baseplate thickness less than 3 inches,
3. A history of loose anchor nuts,
4. Less than 6 anchor rods,
5. Tube wall less than or equal to 5⁄16-inch, or
6. Excessive corrosion of tube wall.

HMLTs with just one of the factors listed above have been shown through experience (i.e., observed cracking) to have less than the intended fatigue life.

After establishing that an HMLT cannot attain infinite life, the evaluation should proceed using the constant-amplitude effective fatigue pressure-range to calculate the effective stress-range, S_{Reff}. The number of cycles the HMLT can sustain can then be estimated from the appropriate stress-life (S-N) curve. Since it has already been shown that S_{Rfls} exceeds the CAFL, the CAFL should not be considered on the S-N curve. Because the constant-amplitude effective fatigue load is considerably less than the fatigue-limit-state load, S_{Reff} will most certainly be less than the CAFL. Therefore, only the sloping portion of the S-N curve need be considered for finite life evaluation. A straight-line extension of the S-N curve will typically be required to perform the assessment, as is commonly done in fatigue evaluation of highway bridges.

3.5.1 Constant-Amplitude Effective Pressure-Range

Measured constant-amplitude effective static pressure-ranges and corresponding mean wind speed values are tabulated in Table 3.17 and plotted in Figure 3.34. The effective static pressure-ranges were arrived at by truncating the histogram data to stress-ranges above 0.5 ksi for all sites except IA-S. The IA-S HMLT was retrofitted by replacing the bottom tube portion with one 5⁄8-inch thick, which is 52 percent thicker than the next thickest pole. This additional stiffness causes the calculated pressure range associated with the histogram bins to be significantly larger than the other HMLTs in the study. As a consequence, cycle counts are lower. In other words, the lowest bin was effectively truncated on site because the base of the pole was so stiff.

The values given in Table 3.18 are recommended for evaluation of existing HMLTs. The value for the constant-amplitude *effective* fatigue static pressure-range was determined in a manner similar to the fatigue-limit-state pressure range discussed above. It is noted that this is similar to the

Table 3.17. Constant-amplitude effective pressure-range and recorded mean wind speed.

ID	WS_{avg}	P_{eff}
CA-A	8.7	1.02
CA-X	8.7	0.89
IAS-A	10.3	1.01*
IAS-X	10.3	0.95*
KS-A	9.4	1.07
KS-X	9.0	1.13
ND-A	6.7	1.02
ND-X	6.7	1.08
OKNE-A	6.8	0.89
OKNE-X	6.8	0.83
OKSW-A	8.3	1.04
OKSW-X	8.8	1.00
PA-A	3.5	0.91
PA-X	3.5	0.94
SD-A	7.8	0.77
SD-X	7.8	0.82
CJE-A (FR)	12.8	1.22
CJE-X (FR)	12.8	1.29
CJW-A (FR)	14.0	1.27
CJW-X (FR)	14.0	1.36

*P_{eff} values are truncated to stress ranges > 0.5 ksi except for IAS.

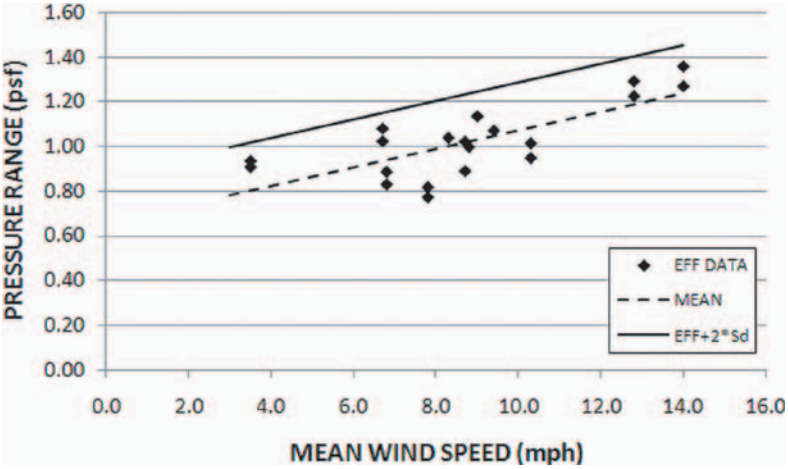

Figure 3.34. Plot of constant-amplitude effective pressure data and upper boundary.

68 Fatigue Loading and Design Methodology for High-Mast Lighting Towers

Table 3.18. Recommended fatigue load pressure-ranges for evaluation.

FATIGUE LOADS FOR EVALUATION (psf)	
Fatigue-limit-state static pressure range, P_{fls}	5.8*
Constant-amplitude effective static pressure-range, P_{eff}	1.3

*Owners may wish to utilize the values for P_{FLS} shown in Table 3.16.

concept of the HS-15 fatigue truck (0.75 × HS-20), which is used for finite life and is intended to represent the cumulative amplitude truck loading spectrum (AASHTO LRFD, 2010). Similarly, the P_{eff} is intended to represent the equivalent fatigue damage of the variable-amplitude wind pressure spectrum. Both values in Table 3.18 correspond to the national average mean wind speed, which would best represent the effect on HMLTs for evaluation purposes. In lieu of adequate local site data, an owner may wish to use the values provided in Table 3.16 for evaluation. However, this will likely result in an overestimate of the pressure ranges. It is recognized that the data shown in Table 3.16 could be utilized for the infinite life check (i.e., one could account for local mean wind speed effects with Table 3.16). The proposed evaluation procedure will provide commentary that allows an owner to use Table 3.16 if they wish. Overall, using the P_{FLS} of 5.8 will provide a reasonable value for assessment of most HMLTs. It is also noted that little variation exists for P_{eff} values over the range of yearly mean wind velocities set as the design limits. P_{eff} values of 1.25, 1.33, and 1.41 psf are determined from yearly mean wind velocities of 9, 11, and 13 mph, respectively. As a result, a single value of 1.3 psf was selected to represent most locations. Using a single effective pressure-range simplifies the approach, as it does for the design of bridges.

Table 3.19. Effective cycle frequencies and recorded mean wind speed.

ID	WS_{avg} (mph)	N/Day
CA-A	8.7	5,820
CA-X	8.7	5,016
IAS-A	10.3	10,167*
IAS-X	10.3	13,770*
KS-A	9.4	12,730
KS-X	9.0	14,359
ND-A	6.7	4,547
ND-X	6.7	6,170
OKNE-A	6.8	8,294
OKNE-X	6.8	8,872
OKSW-A	8.3	13,997
OKSW-X	8.8	16,832
PA-A	3.5	294
PA-X	3.5	441
SD-A	7.8	11,515
SD-X	7.8	12,750
CJE-A (FR)	12.8	18,693
CJE-X (FR)	12.8	35,437
CJW-A (FR)	14.0	28,228
CJW-X (FR)	14.0	36,382

*Histograms truncated to > 0.5 ksi except IAS.

3.5.2 Stress-Range Cycles for Evaluation

As discussed above, measured histogram data show cumulative fatigue damage varies proportionally with wind speed, as would be expected. Most of this variation occurs in terms of cycle counts. Referring back to Table 3.5, note that the normalized values for constant-amplitude effective pressure-range and velocity range are surprisingly similar, while values for cycles per day vary greatly. The proposed evaluation method takes advantage of this variation and allows evaluating engineers to choose an appropriate cycle frequency (i.e., cycles per day), based on mean wind speed similar to the proposed fatigue loads. Mean wind speeds and effective cycle counts are listed in Table 3.19 and plotted in Figure 3.35. The cycle counts were arrived at by truncating

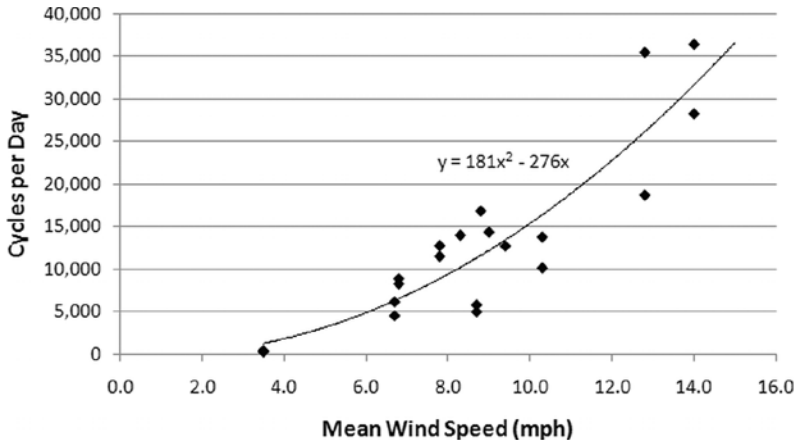

Figure 3.35. Plot of effective cycle frequencies.

Table 3.20. Recommended stress-range cycles for evaluation.

STRESS-RANGE CYCLES FOR EVALUATION	N/DAY
$V_{mean} \leq 9$ mph	9,500
9 mph $< V_{mean} \leq 11$ mph	15,000
$V_{mean} > 11$ mph	23,000
Vortex Shedding Mitigated	7,000

the first bin of histogram data for all sites except IA-S, same as the effective pressure-range data discussed above.

The curve in Figure 3.35 is the best-fit parabola through the data crossing the Y-axis at the origin. The recommended stress-range cycles for evaluation were derived from this curve using the same confidence intervals for wind speed discussed in the proposed fatigue loads. However, instead of using the upper limit of the interval, the median value was used. To determine the lower-bound cycle frequency of 9,500/day, 8 mph was used, which fits in the range of wind speed between 7 and 9 mph (one standard deviation below the mean). To determine the intermediate cycle frequency of 15,000/day, 10 mph was used, which fits in the range of wind speed between 9 and 11 mph (one standard deviation above the mean). To determine the upper-bound cycle frequency of 23,000/day, 12 mph was used, which fits in the range of wind speed between 11 and 13 mph (one and two standard deviations above the mean). Also included in the table is the proposed number of stress-range cycles to be used with an HMLT effectively mitigated against vortex shedding. The value is determined from cycle counts from the three sites where full-length double strakes were installed (WY-CJE, WY-CJW, and IA-N). The same level of truncation was used and the mean value is given. This value is likely to be conservative for most HMLTs mitigated against vortex shedding since the three sites that formed the data set experienced mean wind speeds greater than the average. Recommended stress-range cycles for evaluation are summarized in Table 3.20.

Although it is recognized that the above approach may be questionable to some, it also must be recognized that there is no rational method available to estimate "N" for a given HMLT short of conducting a field instrumentation study. Hence, at present it is offered as a reasonable method based on a significant amount of data to estimate the number of cycles to which a given HMLT may be subjected.

CHAPTER 4

Conclusions and Recommendations

4.1 Conclusions

The findings presented in this report are the basis for the proposed revisions to the fatigue design provisions of the AASHTO Standard Specifications for Structural Supports for Highway Signs, Luminaires and Traffic Signals. The results of the experimental investigation into wind loading, dynamic response, and fatigue analysis of HMLTs are summarized in the following conclusions:

1. The 0.5 percent damping ratio given in Section 11.7.2 of the current edition of AASHTO Signs (2009) is applicable for Mode I vibration of HMLTs within a reasonable statistical confidence; however, it will yield unconservative results if used to evaluate higher modes. It is known that vortex-induced vibration of HMLTs occurs in the second and third modes. Any effort to compute loads associated with vortex shedding should adjust the damping ratios accordingly. (It is noted that in the proposed specifications, such information is no longer required.) Recommended damping ratios are based on the 80 percent confidence limit in Table 102: 0.75 percent, 0.3 percent, and 0.1 percent for Modes I, II, and III, respectively.
2. Increases in the mean wind speed typically result in an increase in the number of damaging load cycles. The fatigue-limit-state pressure range also tends to increase since the magnitude, or scale, of the stress-range distribution changes with increasing cycles. However, the shape of the distribution remains essentially the same, and the resulting effective pressure range for fatigue design (including buffeting, vortex shedding, and associated dynamic response) does not change.
3. Mitigation of vortex-induced vibration mainly affects the accumulation of load cycles. For the double-wrap rope strake tested, results show a significant decrease in the number of stress cycles accumulated on a per day basis, while the corresponding constant-amplitude effective fatigue stress-range and fatigue-limit-state stress-range are essentially unaffected.
4. Infinite life design is appropriate for HMLTs. The number of lifetime loading cycles exceeds the limiting number of cycles at the constant-amplitude fatigue limit for the most common HMLT fatigue detail categories (e.g., Category E) in poles designed to the earlier versions of AASHTO Signs.
5. Static pressure-range values were developed and recommended for fatigue design of HMLTs, and account for both geographic variation in yearly mean wind velocity and variation in experimental data. The proposed static pressure-range values are 5.8, 6.5, and 7.2 psf corresponding to yearly mean wind velocities of 9, 11, and 13 mph, respectively.
6. Static pressure-range values were developed and are recommended for fatigue evaluation of HMLTs. The pressure range used to determine if an HMLT is capable of attaining infinite life is the fatigue-limit-state pressure range of 5.8 psf. The pressure range used to determine the finite life for a given HMLT can be reasonably represented by a constant-amplitude effective pressure range of 1.3 psf. Both values are based on the average yearly mean wind velocity of

9 mph in the United States. Data showed that greater measured mean wind speeds do not significantly influence the corresponding constant-amplitude effective pressure range.

7. Stress range cycle frequencies are recommended for fatigue evaluation of HMLTs. The cycle frequency values are 9,500, 15,000, and 23,000 cycles per day corresponding to yearly mean wind velocities of 8, 10, and 12 mph, respectively. A cycle frequency of 7,000 cycles per day is recommended for HMLTs mitigated against vortex shedding.
8. The coherence of the "lock-in" phenomenon is largely due to the configuration of the pole. Although a face-upwind configuration may or may not lock in, the vertex upwind configuration undoubtedly does for every type of cross section. This means that poles with a vertex toward the prevailing wind are more prone to lock in and exhibit the phenomenon due to the location where the wind separates. Of interest, the phenomenon also seemed to be more prevalent on the 12-sided model. Lock-in happened not only for a much tighter data frequency spread but also for a greater range of diameters. This seems counterintuitive since the 16-sided model is closer to a cylinder and the researcher expected it would exhibit a more uniform response. So far, lock-in has been confirmed up to 18 inches on a 5-foot model or about 25 percent of the wind tunnel model's diameter. To make sure this isn't just the whole model moving, there are also tests where only a bandwidth of 9 span-wise inches are locked in. Further study may prove this to be more than 18 inches as the static mount was not tested before the completion of this report.

4.2 Suggested Research

Based on the results of this study, the following topics are suggested for future research:

1. **Wind tunnel testing of HMLT luminaires—**Conduct wind tunnel tests of luminaire assemblies commonly used by industry to determine reasonable values of effective projected area (EPA) and/or drag coefficients to be used for design. Within the design community, little is known about the aerodynamic properties of luminaires, particularly the interaction of individual lighting elements with their adjacent supporting system.
2. **Investigate the effectiveness of commonly used mitigation devices—**Mitigation can be an effective means for reducing vortex-induced vibration and increasing the fatigue life of HMLTs. Many types of devices exist that may either disrupt the formation of vortices or provide additional damping. However, at present their effectiveness and impact on the design of new poles is not well understood.
3. **Investigate the phenomena responsible for large-amplitude oscillations—**Evidence exists that shows that HMLTs can experience large dynamic oscillations at moderate wind speeds that may significantly reduce fatigue life. These events appear to be very rare, exceeding the 1:10,000 probability, but may be responsible for low-cycle fatigue behavior leading to collapse or significant cracking.

References

Ahearn, E. B., and J. A. Puckett, "Reduction of Wind-Induced Vibrations in High-Mast Light Poles." Report No. FHWA-WY-10/02F, University of Wyoming, Laramie, WY (2010).

Anderson, J. *Fundamentals of Aerodynamics.* 4th ed., McGraw-Hill, New York (2007) pp. 278.

Burt, J. O. and E. J. LeBlanc, "Luminaire Vibration Suppression Study." Louisiana Department of Highways, Baton Rouge, LA (1974).

Connor, R., and I. C. Hodgson, *Field Instrumentation, Testing, and Long-Term Monitoring of High-Mast Lighting Towers in the State of Iowa.* Ames, IA (2006).

Dexter, R. J., *Investigation of Cracking of High-Mast Lighting Towers.* Ames, IA (2004).

Edwards, J. A., and W. L. Bingham, *Deflection Criteria for Wind Induced Vibrations in Cantilever Highway Sign Structures.* Report 110-79-2, Center for Transportation Engineering Studies, North Carolina State University at Raleigh (1984).

Every, M. J., R. King, and D. S. Weaver, "Vortex-Excited Vibrations of Cylinders and Cables and Their Suppression." *Ocean Engineering,* 9(2), (1982) pp. 135–157.

Kaczinski, M. R., R. J. Dexter, and J. P. Van Dien. *NCHRP Report 412: Fatigue-Resistant Design of Cantilevered Signal, Sign, and Light Supports.* Transportation Research Board, National Research Council, Washington, DC (1998).

Krauthammer, T., P. A. Rowekamp, and R. T. Leon, "Experimental Assessment of Wind-Induced Vibrations." *Journal of Engineering Mechanics,* 113(9), (1987) pp. 1387–1403.

Liu, Henry, *Wind Engineering: A Handbook for Structural Engineers,* Prentice-Hall, Inc., Englewood Cliffs, NJ (1991).

Miner, M. A., "Cumulative Damage in Fatigue." *Journal of Applied Mechanics,* 12, (1945) pp. A159–A164.

NOAA, "Comparative Climatic Data for the United States through 2010." National Climatic Data Center, Asheville, NC (2010).

http://hurricane.ncdc.noaa.gov/climaps/wnd60b13.pdf

Phares, B. M., P. P. Sarkar, T. J. Wipf, and B. Chang, "Development of Fatigue Design Procedures for Slender, Tapered Support Structures for Highway Signs, Luminaires, and Traffic Signals Subjected to Wind-Induced Excitation from Vortex Shedding and Buffeting." *MTC Project 2005-02,* Iowa State University, Ames, IA (2007).

Ruscheweyh, H., "Vortex-Excited Vibrations and Galloping of Slender Elements." *Journal of Wind Engineering and Industrial Aerodynamics,* Vol. 65, No. 1–3 (December 1996).

Vickery, B. J., and A. W. Clark, "Lift or Across-Wind Response of a Tapered Stack." *Journal of the Structural Division,* 98, (1972) pp. 1–20.

Vickery, B. J. and Basu, R. I., *Across-Wind Vibrations of Structures of Circular Cross-Section.* "Part II: Development of a Mathematical Model for Two-Dimensional Conditions" (1983).

Warpinski, M. K., *The Effect of Base Connection Geometry on the Fatigue Performance of Welded Socket Connections in Multi-Sided High-Mast Lighting Towers,* Lehigh University, Bethlehem, PA (2006).

Codes and Standards

AASHTO. "Standard Specifications for Structural Supports for Highway Signs, Luminaires and Traffic Signals." (5th ed.). American Association of State Highway Transportation Officials, Washington, DC (2009).

AASHTO. "LRFD Bridge Design Specifications." (5th ed.). American Association of State Highway Transportation Officials, Washington, DC (2010).

ASTM E756-98 (1998). "Standard Test Method for Measuring Vibration-Damping Properties of Materials," American Society for Testing and Materials, West Conshohocken, PA.

ASTM Standard E1049, 1985 (2005). "Standard Practices for Cycle Counting in Fatigue Analysis." ASTM International, West Conshohocken, PA.

CSA. (2006). "CAN/CSA-S6-06: Canadian Highway Bridge Design Code." Canadian Standards Association, Toronto.

APPENDIX A

HMLT Fatigue Design Examples

EXAMPLE 1

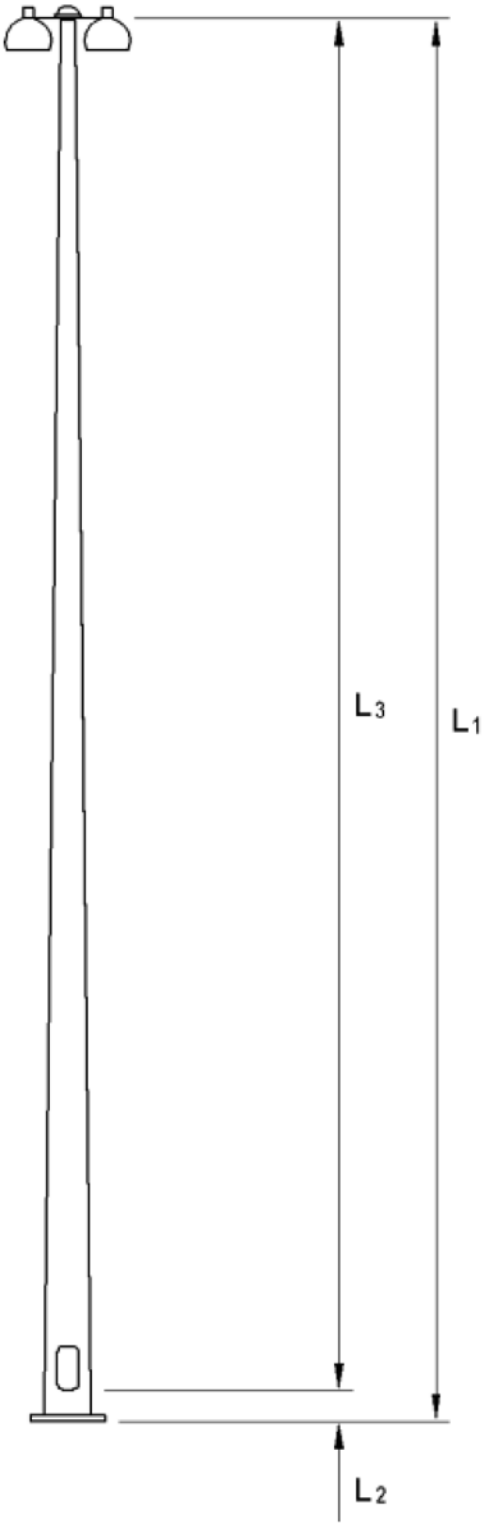

ELEVATION

GENERAL

Description

The support structure for the 80-ft HMLT shown consists of a tapered prismatic tube with access handhole and circular baseplate, and is to be designed for fatigue according to Section 11 of the AASHTO Specification. The shape of the tube is a regular polygon with 16 sides. The column-to-baseplate connection is groove welded with the backing ring attached to the base plate, and the handhole detail is of the "doubler" plate type. The location of the HMLT is in a region where NOAA weather data suggest the annual mean wind speed will not exceed 9 mph, and the lighting plan for the interchange does not require the HMLT to be any closer than 100 feet from the roadway. Furthermore, it is assumed the structure will not be built with vibration mitigating devices. All calculations shown are in imperial units.

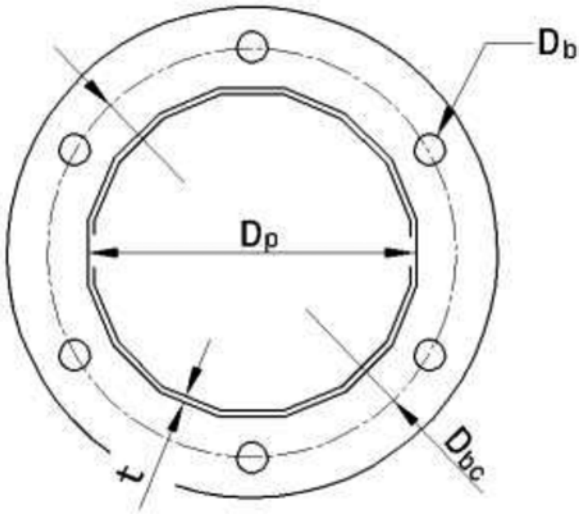

SECTION AT BASEPLATE

Dimensions

Pole

Pole height

$L_1 = 80\ ft$

Length from pole baseplate to termination of handhole $L_2 = 2\ ft$

Length from termination of handhole to luminaire $L_3 = 78\ ft$

Pole diameter at base (across flats)

$D_p = 18\ in$

Pole taper rate

$\theta = 0.14\ in/ft$

Pole wall thickness

t = $0.25\ in$

Anchor Bolts

Number of bolts

$n_b = 6$

Bolt group diameter

$D_{bg} = 23\ in$

Nominal bolt diameter

$D_b = 1.50\ in$

Luminaire

Effective projected area on a vertical plane

$EPA = 16\ ft^2$

Critical Fatigue Details

The HMLT support structure contains the following details which must be designed for fatigue:

1. Anchor bolts (Detail 5 in Table 11-4)
2. Full-penetration groove welded column-to-baseplate connection with backing ring attached to baseplate (Detail 11 in Table 11-4)
3. Transverse fillet weld at termination of handhole (Detail 3.5 in Table 6.6.1.2.3-1 in AASHTO LRFD)

FATIGUE LOADS

Static Wind Loads

The only load considered for fatigue design of HMLTs is the Combined Wind Effect (Section 11.7.2). Since the pole and the luminaire are subject to different drag coefficients, two separate calculations are made.

Drag coefficient for pole (Table 3-6) $C_d = 1.1$

Drag coefficient for luminaire (Table 3-6) $C_d = 1.0$

Since the height of the HMLT is less than the distance to the roadway, the HMLT is designed using Importance Category II from Table 11-2. The fatigue-limit-state pressure range is determined from Table 11-3. Since the annual mean wind speed is expected to be less than 9 mph, the fatigue-limit-state pressure range is

$$P_{fls} = 5.8\ psf$$

Using Equation 11-7, $P_{CW} = P_{fls} C_d$, calculate the wind effect on the pole and luminaire:

Combined wind effect pressure range applied to pole

$$P_{CW\_Pole} = 5.8\ psf\ (1.1) = 6.4\ psf$$

Combined wind effect pressure range applied to luminaire

$$P_{CW\ Lum} = 5.8\ psf\ (1.0) = 5.8\ psf$$

BENDING MOMENTS

Bending moments are calculated for two different locations: at the base of the pole, to check anchor bolts and column-to-baseplate connection, and at the termination of the handhole.

Calculate length from baseplate to center of pressure of pole

$$L_{CP1} = \frac{L_1\left(D_p - L_1\theta\right) + \frac{1}{3}L_1^2\theta}{2D_p - L_1\theta} = \frac{80\,ft\left[18in - 80\,ft\left(0.14in/\,ft\right)\right] + \frac{1}{3}\left(80\,ft\right)^2\left(0.14in/\,ft\right)}{\left[2\left(18in\right) - 80\,ft\left(0.14in/\,ft\right)\right]} = 34.0\ ft$$

Projected area of pole on a vertical plane

$$A_{p1} = \left(D_p - \frac{1}{2}L_1\theta\right)L_1 = \left[18in - \frac{1}{2}\left(80\,ft\right)\left(0.14in/\,ft\right)\right]\left(80\,ft\right)\left(\frac{ft}{12in}\right) = 82.7\ ft^2$$

Bending moment at base of pole

$$M_1 = P_{CW\_Pole}A_pL_{CP1} + P_{CW\_Lum}EPA\left(L_1\right) = \frac{6.4\,psf\left(82.7\,ft^2\right)\left(34.0\,ft\right) + 5.8\,psf\left(16\,ft^2\right)\left(80\,ft\right)}{1000lb} = 25.4\ k\cdot ft$$

Pole diameter at handhole termination

$$D_{hh} = D_p - L_2\theta = 18in - 2\,ft(0.14in/\,ft) = 17.72\ in$$

Calculate length from handhole termination to center of pressure of pole for area above handhole

$$L_{CP2} = \frac{L_3\left(D_{hh} - L_3\theta\right) + \frac{1}{3}L_3^2\theta}{2D_{hh} - L_3\theta} = \frac{78\,ft\left[17.72in - 78\,ft\left(0.14in/\,ft\right)\right] + \frac{1}{3}\left(78\,ft\right)^2\left(0.14in/\,ft\right)}{2\left(17.72in\right) - 78\,ft\left(0.14in/\,ft\right)} = 33.2\ ft$$

Projected area of pole on a vertical plane above handhole termination

$$A_{p2} = \left(D_{hh} - \frac{1}{2}L_3\theta\right)L_3 = \left[17.72in - \frac{1}{2}\left(78\,ft\right)\left(0.14in/\,ft\right)\right]\left(78\,ft\right)\left(\frac{ft}{12in}\right) = 79.7\ ft^2$$

Bending moment at termination of handhole

$$M_2 = P_{CW\_Pole}A_{p2}L_{CP2} + P_{CW\_Lum}EPA\left(L_3\right) = \frac{6.4\,psf\left(79.7\,ft^2\right)\left(33.2\,ft\right) + 5.8\,psf\left(16\,ft^2\right)\left(78\,ft\right)}{1000lb} = 24.2k\cdot ft$$

STRESS RANGE CALCULATIONS

Anchor Bolts

For the 1.50 inch diameter anchor bolts chosen, the tensile stress area is 1.41 in^2. The tensile stress area may be found in any steel design manual.

Moment of inertia of bolt group

$$I_{bg} = \frac{n_b R_{bg}^2}{2}$$ where R_{bg} equals the radius of the bolt group, *11.5 in.*

$$I = \frac{6(11.5in)^2}{2} = 397in^2$$

Maximum applied load range per bolt

$$L_{Rb} = \frac{M_1 R_{bg}}{I_{bg}} = \frac{25.4kft(11.5in)}{397in^2}(12in/ft) = 8.83\,k/bolt$$

Anchor bolt stress range $(S_R)_b = 8.83\ k/1.41\ in^2 = 6.26\ ksi$

Anchor bolts are classified as Category D details for infinite life (Detail 5 in Table 11-4). The CAFL corresponding to Category D is 7.0 ksi. Since the calculated stress range (6.26 ksi) is less than the CAFL (7.0 ksi), the anchor bolt group is adequate for fatigue.

Column-to-Baseplate Connection

The section modulus for various tubular shapes can be determined using the equations given in Appendix B of the specification. For the 16-sided pole given

$$S = 3.22R^2t$$

where R equals the radius of the tube measured to the mid-thickness of the wall.

Radius of pole at its base, measured to mid-thickness of wall

$R = (18 - 0.25\ in)/2 = 8.875\ in$

Section modulus of pole at its base $S_p = 3.22(8.875\ in)^2(0.25\ in) = 63.4\ in^3$

Stress range at pole base

$$(S_R)_p = \frac{M_1}{S_p} = \frac{25.4kft}{63.4in^3}(12in/ft) \qquad (S_R)_p = 4.81\ ksi$$

A groove welded column-to-baseplate connection *with* backing ring is classified as a Category E fatigue detail (Detail 11 in Table 11-4). The CAFL corresponding to Category E is 4.5 ksi. Since the calculated stress range (4.81 ksi) is *greater than* the CAFL (4.5 ksi), the detail is not adequate for fatigue. Increasing the thickness of the pole wall to 0.313 inches will alleviate this problem as shown below.

Radius of pole at its base, measured to mid-thickness of wall

$R = (18 - 0.313\ in)/2 = 8.844\ in$

Section modulus of pole at its base $S_p = 3.22(8.844\ in)^2(0.313\ in) = 78.8\ in^3$

Stress range at pole base

$$(S_R)_p = \frac{M_1}{S_p} = \frac{25.4kft}{78.8in^3}(12in/ft) \qquad (S_R)_p = 3.87\ ksi\ <\ 4.5ksi \rightarrow OK!$$

Transverse Fillet Weld at Handhole

A detail of the doubler plate handhole reinforcement is shown below. The area with greatest potential for crack growth is the transverse fillet weld across the bottom of the plate.

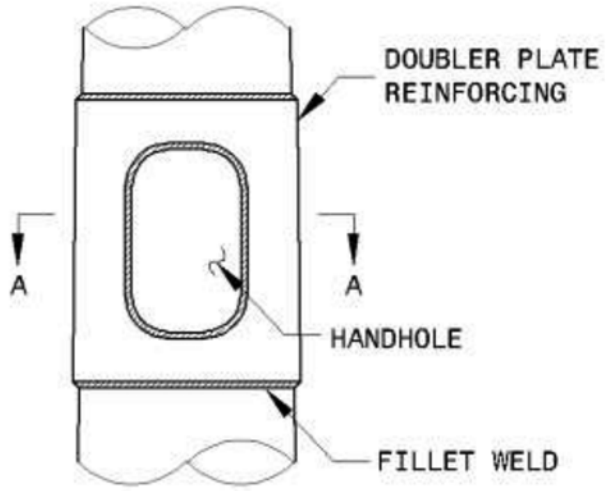

The diameter of the pole at the location of the transverse fillet weld is 17.72 inches as calculated above.

Radius of pole at the location of the transverse fillet weld, measured to mid-thickness of wall

$$R = (17.72 - 0.313\ in)/2 = 8.704\ in$$

Section modulus of pole at its base $S_{hh} = 3.22(8.704\ in)^2(0.313\ in) = 76.3\ in^3$

Stress range at pole base

$$(S_R)_{hh} = \frac{M_2}{S_{hh}} = \frac{24.2kft}{76.3in^3}(12in/ft) \qquad (S_R)_{hh} = 3.81\ ksi$$

The termination of welds at the end of a plate with or without welds across the ends is classified as a Category E fatigue detail (Detail 3.5 in Table 6.6.1.2.3-1 in AASHTO LRFD). The CAFL corresponding to Category E is 4.5 ksi. Since the calculated stress range (3.92 ksi) is less than the CAFL (4.5 ksi), the detail is adequate for fatigue.

EXAMPLE 2

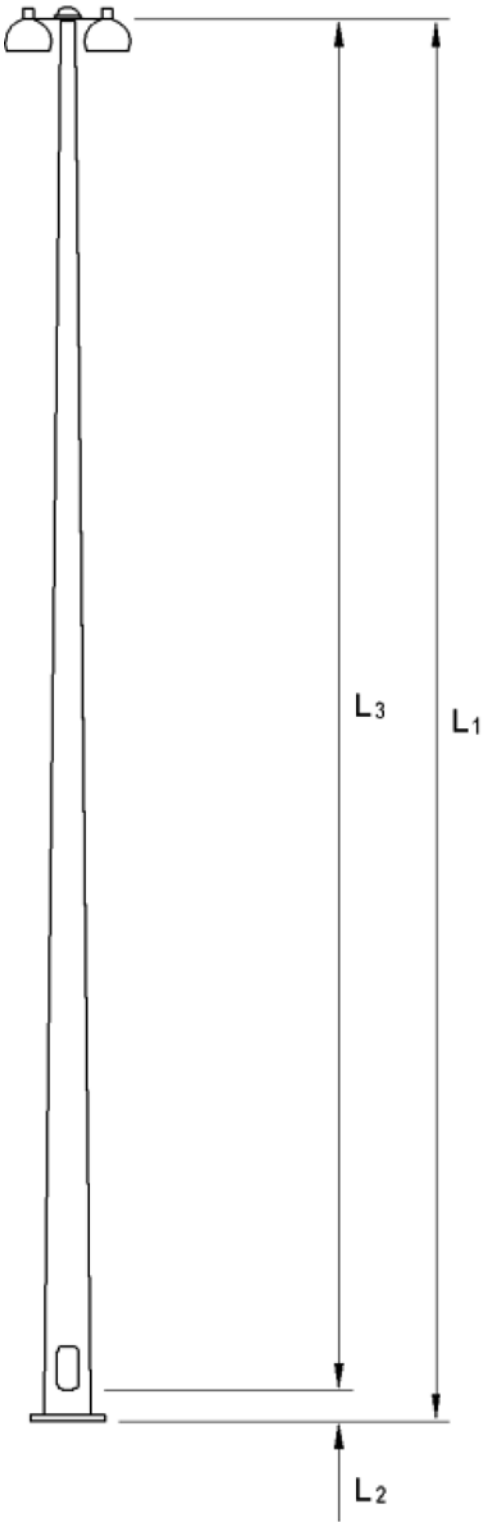

ELEVATION

GENERAL

Description

The support structure for the 120-ft HMLT shown consists of a tapered prismatic tube with access handhole and circular baseplate, and is to be designed for fatigue according to Section 11 of the AASHTO Specifications. The shape of the tube is a regular polygon with 12 sides. The column-to-baseplate connection is groove welded with the backing ring attached to the baseplate, and the handhole detail is of the "doubler" plate type. The location of the HMLT is in a region where NOAA weather data suggest the annual mean wind speed will exceed 11 mph, and the lighting plan for the interchange requires the HMLT to be 90 ft from the roadway. It is assumed the structure will not be built with vibration mitigating devices. All calculations shown are in imperial units.

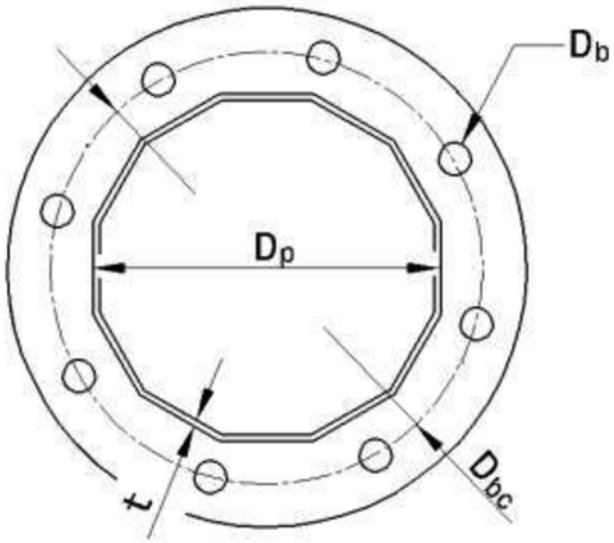

SECTION AT BASEPLATE

Dimensions

Pole

Pole height $L_1 = 120\ ft$

Length from pole baseplate to termination of handhole $L_2 = 2\ ft$

Length from termination of handhole to luminaire $L_3 = 118\ ft$

Pole diameter at base (across flats) $D_p = 24\ in$

Pole taper rate $\theta = 0.14\ in/ft$

Pole wall thickness at base $t = 0.50\ in$

Anchor Bolts

Number of bolts $n_b = 8$

Bolt group diameter $D_{bg} = 30\ in$

Nominal bolt diameter $D_b = 2.0\ in$

Luminaire

Effective projected area on a vertical plane $EPA = 20\ ft^2$

Critical Fatigue Details

The HMLT support structure contains the following details that must be designed for fatigue:

1. Anchor bolts (Detail 5 in Table 11-4)
2. Full-penetration groove welded column-to-baseplate connection with backing ring attached to baseplate (Detail 11 in Table 11-4)
3. Transverse fillet weld at termination of handhole (Detail 3.5 in Table 6.6.1.2.3-1 in AASHTO LRFD)

FATIGUE LOADS

Static Wind Loads

The only load considered for fatigue design of HMLTs is the Combined Wind Effect (Section 11.7.2). Since the pole and the luminaire are subject to different drag coefficients, two separate calculations are made.

Drag coefficient for pole (Table 3-6) $C_d = 1.2$

Drag coefficient for luminaire (Table 3-6) $C_d = 1.0$

Since the height of the HMLT is greater than the distance to the roadway, the HMLT is designed using Importance Category I from Table 11-2. The fatigue-limit-state pressure range is determined from Table 11-3. Since the annual mean wind speed is expected to be greater than 11 mph, the fatigue-limit-state pressure range is

$$P_{fls} = 7.2\ psf$$

Using Equation 11-7, $P_{CW} = P_{fls}C_d$, calculate the wind effect on the pole and luminaire.

Combined wind effect pressure range applied to pole

$$P_{CW\_Pole} = 7.2\ psf\ (1.2) = 8.6\ psf$$

Combined wind effect pressure range applied to luminaire

$$P_{CW\ Lum} = 7.2\ psf\ (1.0) = 7.2\ psf$$

BENDING MOMENTS

Bending moments are calculated at two different locations: at the base of the pole—to check anchor bolts and column-to-baseplate connection—and at the termination of the handhole.

Calculate length from baseplate to center of pressure of pole

$$L_{CP1} = \frac{L_1\left(D_p - L_1\theta\right) + \frac{1}{3}L_1^2\theta}{2D_p - L_1\theta} = \frac{120\,ft\left[24in - 120\,ft\left(0.14in/\,ft\right)\right] + \frac{1}{3}\left(120\,ft\right)^2\left(0.14in/\,ft\right)}{2\left(24in\right) - 120\,ft\left(0.14in/\,ft\right)} = 49.2\;ft$$

Projected area of pole on a vertical plane

$$A_{p1} = \left(D_p - \frac{1}{2}L_1\theta\right)L_1 = \left[24in - \frac{1}{2}\left(120\,ft\right)\left(0.14in/\,ft\right)\right]\left(120\,ft\right)\left(\frac{ft}{12in}\right) = 156\;ft^2$$

Bending moment at base of pole

$$M_1 = P_{CW\_Pole}A_pL_{CP1} + P_{CW\_Lum}EPA\left(L_1\right) = \frac{8.6\,psf\left(156\,ft^2\right)\left(49.2\,ft\right) + 7.2\,psf\left(20\,ft^2\right)\left(120\,ft\right)}{1000lb} = 83.3\,k\cdot ft$$

Pole diameter at handhole termination

$$D_{hh} = D_p - L_2\theta = 24in - 2ft(0.14in/\,ft) = 23.72\,in$$

Calculate length from handhole termination to center of pressure of pole for area above handhole

$$L_{CP2} = \frac{L_3\left(D_{hh} - L_3\theta\right) + \frac{1}{3}L_3^2\theta}{2D_{hh} - L_3\theta} = \frac{118\,ft\left[23.72in - 118\,ft\left(0.14in/\,ft\right)\right] + \frac{1}{3}\left(118\,ft\right)^2\left(0.14in/\,ft\right)}{2\left(23.72in\right) - 118\,ft\left(0.14in/\,ft\right)} = 48.5\;ft$$

Projected area of pole on a vertical plane above handhole termination

$$A_{p2} = \left(D_{hh} - \frac{1}{2}L_3\theta\right)L_3 = \left[23.72in - \frac{1}{2}\left(118\,ft\right)\left(0.14in/\,ft\right)\right]\left(118\,ft\right)\left(\frac{ft}{12in}\right) = 152\;ft^2$$

Bending moment at termination of handhole

$$M_2 = P_{CW\_Pole}A_{p2}L_{CP2} + P_{CW\_Lum}EPA\left(L_3\right) = \frac{8.6\,psf\left(152\,ft^2\right)\left(48.5\,ft\right) + 7.2\,psf\left(20\,ft^2\right)\left(118\,ft\right)}{1000lb} = 80.4k\cdot ft$$

STRESS RANGE CALCULATIONS

Anchor Bolts

For the 2.00-inch diameter anchor bolts chosen, the tensile stress area is $2.50\;in^2$. The tensile stress area may be found in any steel design manual.

Moment of inertia of bolt group

$$I_{bg} = \frac{n_b R_{bg}^2}{2}$$ where R_{bg} equals the radius of the bolt group, *15 in*.

$$I = \frac{8(15in)^2}{2} = 900\ in^2$$

Maximum applied load range per bolt

$$L_{Rb} = \frac{M_1 R_{bg}}{I_{bg}} = \frac{83.3kft\,(15in)}{900in^2}(12in/ft) = 16.7\ k/bolt$$

Anchor bolt stress range $(S_R)_b = 16.7\ k/2.50\ in^2 = 6.68\ ksi$

Anchor bolts are classified as Category D details for infinite life (Detail 5 in Table 11-4). The CAFL corresponding to Category D is 7.0 ksi. Since the calculated stress range (6.68 ksi) is less than the CAFL (7.0 ksi), the anchor bolt group is adequate for fatigue.

Column-to-Baseplate Connection

The section modulus for various tubular shapes can be determined using the equations given in Appendix B of the specification. For the 12-sided pole given

$$S = 3.29R^2t$$

where R equals the radius of the tube measured to the mid-thickness of the wall.

Radius of pole at its base, measured to mid-thickness of wall

$R = (24 - 0.5\ in)/2 = 11.75\ in$

Section modulus of pole at its base $S_p = 3.29(11.75\ in)^2(0.5\ in) = 227\ in^3$

Stress range at pole base

$$(S_R)_p = \frac{M_1}{S_p} = \frac{83.3kft}{227in^3}(12in/ft) \qquad (S_R)_p = 4.40\ ksi$$

A groove welded column-to-baseplate connection *with* backing ring is classified as a Category E fatigue detail (Detail 11 in Table 11-4). The CAFL corresponding to Category E is 4.5 ksi. Since the calculated stress range (4.40 ksi) is less than the CAFL (4.5 ksi), the detail is adequate for fatigue.

Transverse Fillet Weld at Handhole

A detail of the doubler plate handhole reinforcement is shown below. The area with greatest potential for crack growth is the transverse fillet weld across the bottom of the plate.

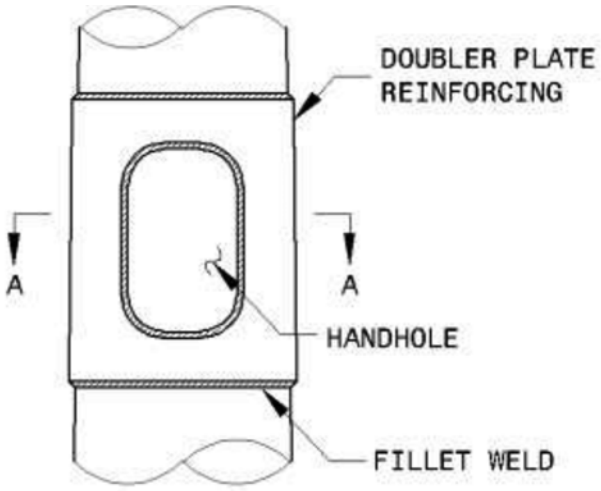

The diameter of the pole at the location of the transverse fillet weld is 23.72 inches as calculated above.

Radius of pole at the location of the transverse fillet weld, measured to mid-thickness of wall

$$R = (23.72 - 0.5\ in)/2 = 11.61\ in$$

Section modulus of pole at its base $S_{hh} = 3.29(11.61\ in)^2(0.5\ in) = 222\ in^3$

Stress range at pole base

$$(S_R)_{hh} = \frac{M_2}{S_{hh}} = \frac{80.4kft}{222in^3}\left(12in/ft\right) \qquad (S_R)_{hh} = 4.35\ ksi$$

The termination of welds at the end of a plate with or without welds across the ends is classified as a Category E fatigue detail (Detail 3.5 in Table 6.6.1.2.3-1 in AASHTO LRFD). The CAFL corresponding to Category E is 4.5 ksi. Since the calculated stress range (4.35 ksi) is less than the CAFL (4.5 ksi), the detail is adequate for fatigue.

EXAMPLE 3

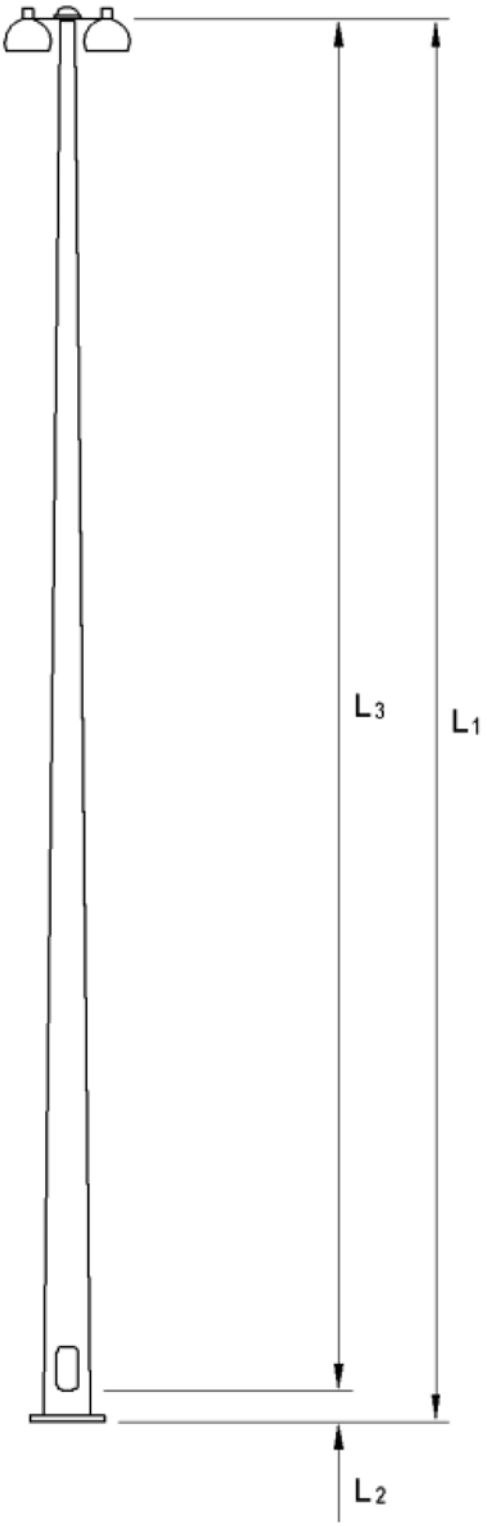

ELEVATION

GENERAL

Description

The support structure for the 120-ft HMLT shown consists of a tapered prismatic tube with access handhole and circular baseplate, and is to be designed for fatigue according to Section 11 of the AASHTO Specifications. The shape of the tube is a regular polygon with 16 sides. The column-to-baseplate connection is a fillet-welded socket type, and the handhole is reinforced with a fillet-welded stiffening ring. The location of the HMLT is in a region where NOAA data suggest the annual mean wind speed will not exceed 9 mph; however, the lighting plan for the interchange requires the HMLT to be 80 ft from the roadway. Furthermore, it is assumed the structure will not be built with vibration mitigating devices. All calculations shown are in imperial units.

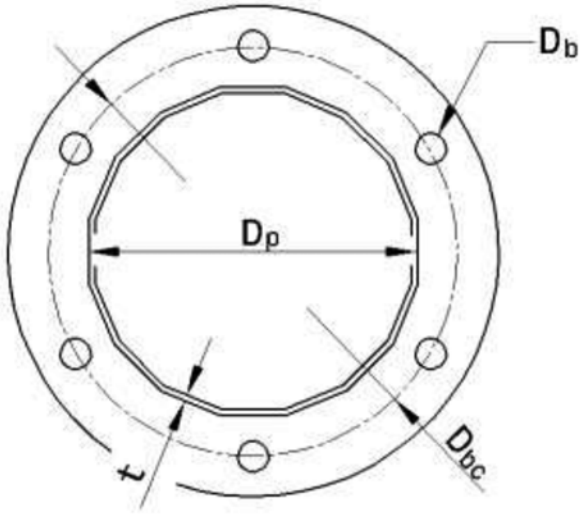

SECTION AT BASEPLATE

Dimensions

Pole

Pole height
$L_1 = 120\ ft$
Length from pole baseplate to termination of handhole $L_2 = 2\ ft$
Length from termination of handhole to luminaire $L_3 = 118\ ft$
Length from pole baseplate to slip-joint
$L_4 = 11\ ft$
Pole diameter at base (across flats)
$D_p = 24\ in$
Pole taper rate
$\theta = 0.14\ in/ft$
Pole wall thickness at base
$t_1 = 0.50\ in$
Pole wall thickness above slip-joint
$t_2 = 0.25\ in$

Anchor Bolts

Number of bolts
$n_b = 8$
Bolt group diameter
$D_{bg} = 30\ in$
Nominal bolt diameter
$D_b = 1.75\ in$

Luminaire

Effective projected area on a vertical plane
$EPA = 12\ ft^2$

Critical Fatigue Details

The HMLT support structure contains the following details that must be designed for fatigue:

1. Anchor bolts (Detail 5 in Table 11-4)
2. Column-to-baseplate fillet-welded socket connection (Detail 16 in Table 11-4)
3. Transverse fillet weld at termination of handhole (Detail 20 in Table 11-4)

FATIGUE LOADS

Static Wind Loads

The only load considered for fatigue design of HMLTs is the Combined Wind Effect (Section 11.7.2). Since the pole and the luminaire are subject to different drag coefficients, two separate calculations are made.

Drag coefficient for pole (Table 3-6) $C_d = 1.1$
Drag coefficient for luminaire (Table 3-6) $C_d = 1.0$

Since the height of the HMLT is greater than the distance to the roadway, the HMLT is designed using Importance Category I from Table 11-2. The fatigue-limit-state pressure range is determined from Table 11-3. Even though the annual mean wind speed is expected to be less than 9 mph, the intermediate value must be used.

$$P_{fls} = 6.5\ psf$$

Using Equation 11-7, $P_{CW} = P_{fls}C_d$, calculate the wind effect on the pole and luminaire.
Combined wind effect pressure range applied to pole

$$P_{CW\ Pole} = 6.5\ psf\ (1.1) = 7.2\ psf$$

Combined wind effect pressure range applied to luminaire

$$P_{CW\ Lum} = 6.5\ psf\ (1.0) = 6.5\ psf$$

BENDING MOMENTS

Bending moments are calculated at three different locations: at the base of the pole—to check anchor bolts and column-to-baseplate connection—at the termination of the handhole, and at the slip-joint.

Calculate length from baseplate to center of pressure of pole

$$L_{CP1} = \frac{L_1\left(D_p - L_1\theta\right) + \frac{1}{3}L_1^2\theta}{2D_p - L_1\theta} = \frac{120\,ft\left[24in - 120\,ft\left(0.14in/\,ft\right)\right] + \frac{1}{3}\left(120\,ft\right)^2\left(0.14in/\,ft\right)}{2\left(24in\right) - 120\,ft\left(0.14in/\,ft\right)} = 49.2\ ft$$

Projected area of pole on a vertical plane

$$A_{p1} = \left(D_p - \frac{1}{2}L_1\theta\right)L_1 = \left[24in - \frac{1}{2}\left(120\,ft\right)\left(0.14in/\,ft\right)\right]\left(120\,ft\right)\left(\frac{ft}{12in}\right) = 156\ ft^2$$

Bending moment at base of pole

$$M_1 = P_{CW\_Pole}A_pL_{CP1} + P_{CW\_Lum}EPA\left(L_1\right) = \frac{7.2\,psf\left(156\,ft^2\right)\left(49.2\,ft\right) + 6.5\,psf\left(12\,ft^2\right)\left(120\,ft\right)}{1000lb} = 64.6\ k\cdot ft$$

Pole diameter at handhole termination

$$D_{hh} = D_p - L_2\theta = 24in - 2\,ft(0.14in/\,ft) = 23.72\ in$$

Calculate length from handhole termination to center of pressure of pole for area above handhole

$$L_{CP2} = \frac{L_3\left(D_{hh} - L_3\theta\right) + \frac{1}{3}L_3^2\theta}{2D_{hh} - L_3\theta} = \frac{118\,ft\left[23.72in - 118\,ft\left(0.14in/\,ft\right)\right] + \frac{1}{3}\left(118\,ft\right)^2\left(0.14in/\,ft\right)}{2\left(23.72in\right) - 118\,ft\left(0.14in/\,ft\right)} = 48.5\ ft$$

Projected area of pole on a vertical plane above handhole termination

$$A_{p2} = \left(D_{hh} - \frac{1}{2}L_3\theta\right)L_3 = \left[23.72in - \frac{1}{2}\left(118\,ft\right)\left(0.14in/\,ft\right)\right]\left(118\,ft\right)\left(\frac{ft}{12in}\right) = 152\ ft^2$$

Bending moment at termination of handhole

$$M_2 = P_{CW\_Pole}A_{p2}L_{CP2} + P_{CW\_Lum}EPA\left(L_3\right) = \frac{7.2\,psf\left(152\,ft^2\right)\left(48.5\,ft\right) + 6.5\,psf\left(12\,ft^2\right)\left(118\,ft\right)}{1000lb} = 62.3k\cdot ft$$

STRESS RANGE CALCULATIONS

Anchor Bolts

For the 1.75-inch diameter anchor bolts chosen, the tensile stress area is $1.90\ in^2$. The tensile stress area may be found in any steel design manual.

Moment of inertia of bolt group

$$I_{bg} = \frac{n_b R_{bg}^2}{2}$$ where R_{bg} equals the radius of the bolt group, $15\ in$.

$$I = \frac{8(15in)^2}{2} = 900\ in^2$$

Maximum applied load range per bolt

$$L_{Rb} = \frac{M_1 R_{bg}}{I_{bg}} = \frac{64.6kft(15in)}{900in^2}(12in/ft) = 12.92\ k/bolt$$

Anchor bolt stress range $(S_R)_b = 12.92\ k/1.90\ in^2 = 6.80\ ksi$

Anchor bolts are classified as Category D details for infinite life (Detail 5 in Table 11-4). The CAFL corresponding to Category D is 7.0 ksi. Since the calculated stress range (6.80 ksi) is less than the CAFL (7.0 ksi), the anchor bolt group is adequate for fatigue.

Column-to-Baseplate Connection

The section modulus for various tubular shapes can be determined using the equations given in Appendix B of the specification. For the 16-sided pole given

$$S = 3.22R^2t$$

where R equals the radius of the tube measured to the mid-thickness of the wall.

Radius of pole at its base, measured to mid-thickness of wall

$$R = (24 - 0.5\ in)/2 = 11.75\ in$$

Section modulus of pole at its base $S_p = 3.22(11.75\ in)^2(0.5\ in) = 222\ in^3$

Stress range at pole base

$$(S_R)_p = \frac{M_1}{S_p} = \frac{64.6kft}{222in^3}(12in/ft)$$ $(S_R)_p = 3.49\ ksi$

A fillet-welded socket column-to-baseplate connection is classified as a Category E' fatigue detail (Detail 16 in Table 11-4). The CAFL corresponding to Category E' is 2.6 ksi. Since the calculated stress range (3.49 ksi) is *greater than* the CAFL (2.6 ksi), the detail is not adequate for fatigue.

To increase the thickness of the pole base above 0.50 inches and to also keep the design economical, a slip-joint is added near the bottom of the pole as shown in the figure below. Increasing the thickness of the pole wall to 0.688 inches will alleviate this problem as shown below.

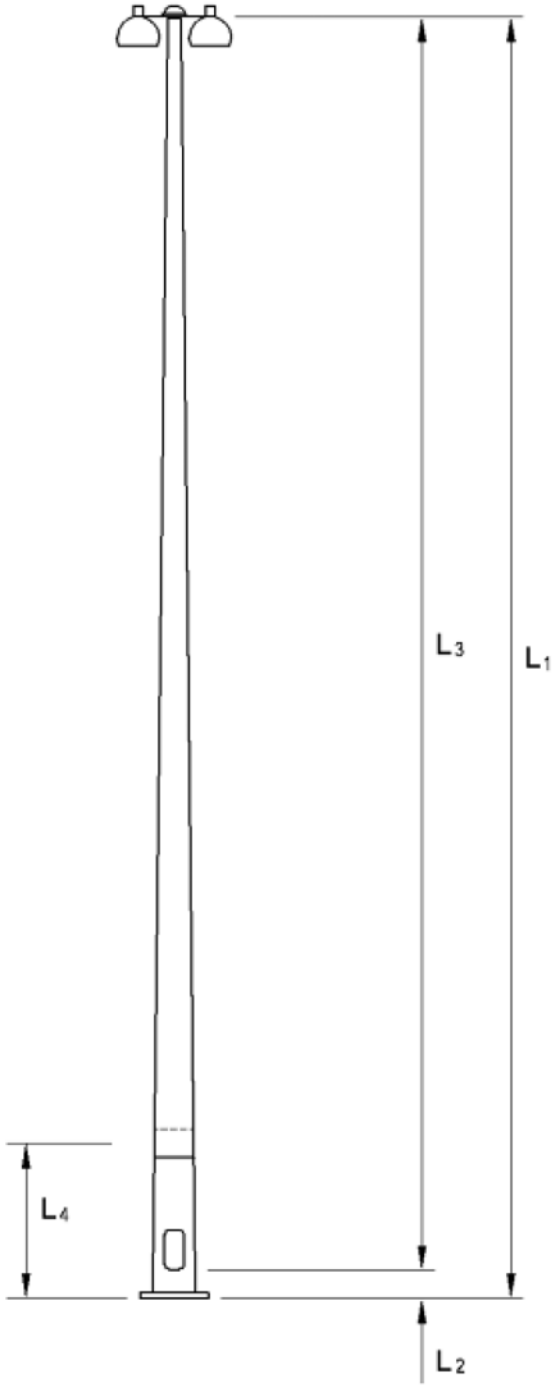

Radius of pole at its base, measured to mid-thickness of wall

$$R = (24 - 0.688\ in)/2 = 11.66\ in$$

Section modulus of pole at its base

$$S_p = 3.22(11.66\ in)^2(0.688\ in) = 301\ in^3$$

Stress range at pole base

$$(S_R)_p = \frac{M_1}{S_p} = \frac{64.6kft}{301in^3}\left(12in/ft\right)$$

$$(S_R)_p = 2.58\ ksi < 2.6\ ksi \rightarrow OK!$$

Transverse Fillet Weld at Handhole

The diameter of the pole at the location of the transverse fillet weld is 23.72 inches as calculated above.

Radius of pole at the location of the transverse fillet weld, measured to mid-thickness of wall

$$R = (23.72 - 0.688\ in)/2 = 11.52\ in$$

Section modulus of pole at its base $S_{hh} = 3.22(11.52\ in)^2(0.688\ in) = 294\ in^3$

Stress range at termination of handhole

$$(S_R)_{hh} = \frac{M_2}{S_{hh}} = \frac{62.3kft}{294in^3}\left(12in/\ ft\right) \qquad (S_R)_{hh} = 2.54\ ksi$$

Assuming the length of the handhole is greater than 4 inches, the handhole detail is considered Category E for fatigue (Detail 20 in Table 11-4). The CAFL corresponding to Category E is 4.5 ksi. Since the calculated stress range (2.54 ksi) is less than the CAFL (4.5 ksi), the detail is adequate for fatigue.

Slip-Joint

Since the slip-joint was added near the base of the pole, it must also be checked for fatigue. (Slip-joint splice, Detail 2 in Table 11-4.) Begin by calculating the bending moment at that location.

Pole diameter at slip-joint

$$D_{sj} = D_p - L_4\theta = 24in - 11ft(0.14in/\ ft) = 22.46\ in$$

Calculate length from slip-joint to center of pressure of pole for area above slip-joint. Let L_5 equal the length from the slip-joint to the luminaire ($109\ ft$).

$$L_{CP3} = \frac{L_5\left(D_{sj} - L_5\theta\right) + \frac{1}{3}L_5^2\theta}{2D_{sj} - L_5\theta} = \frac{109ft\left[22.46in - 109ft\left(0.14in/\ ft\right)\right] + \frac{1}{3}\left(109ft\right)^2\left(0.14in/\ ft\right)}{2\left(22.46in\right) - 109ft\left(0.14in/\ ft\right)} = 45.2\ ft$$

Projected area of pole on a vertical plane above slip-joint

$$A_{p3} = \left(D_{sj} - \frac{1}{2}L_5\theta\right)L_5 = \left[22.46in - \frac{1}{2}\left(109ft\right)\left(0.14in/\ ft\right)\right]\left(109ft\right)\left(\frac{ft}{12in}\right) = 134.7\ ft^2$$

Bending moment at slip-joint

$$M_3 = P_{CW\_Pole}A_{p2}L_{CP2} + P_{CW\_Lum}EPA\left(L_5\right) = \frac{7.2psf\left(134.7ft^2\right)\left(45.2ft\right) + 6.5psf\left(12ft^2\right)\left(109ft\right)}{1000lb} = 52.3k\cdot ft$$

The diameter of the pole at the location of the slip-joint is 22.46 inches as calculated above. The section modulus for various tubular shapes can be determined using the equations given in Appendix B of the specification. For the 16-sided pole given

$$S = 3.22R^2t$$

where R equals the radius of the tube measured to the mid-thickness of the wall.

Radius of pole at the slip-joint, measured to mid-thickness of wall

$$R = (22.46 - 0.25\ in)/2 = 11.11\ in$$

Section modulus of pole at its base

$$S_{sj} = 3.22(11.11\ in)^2(0.25\ in) = 99.3\ in^3$$

Stress range at pole base

$$(S_R)_{sj} = \frac{M_3}{S_{sj}} = \frac{52.3kft}{99.3in^3}\left(12in/ft\right) \qquad (S_R)_p = 6.32\ ksi$$

A slip-joint splice is classified as a Category B fatigue detail (Detail 2 in Table 11-4). The CAFL corresponding to Category B is 16 ksi. Since the calculated stress range (6.32 ksi) is less than the CAFL (16 ksi), the detail is adequate for fatigue.

EXAMPLE 4

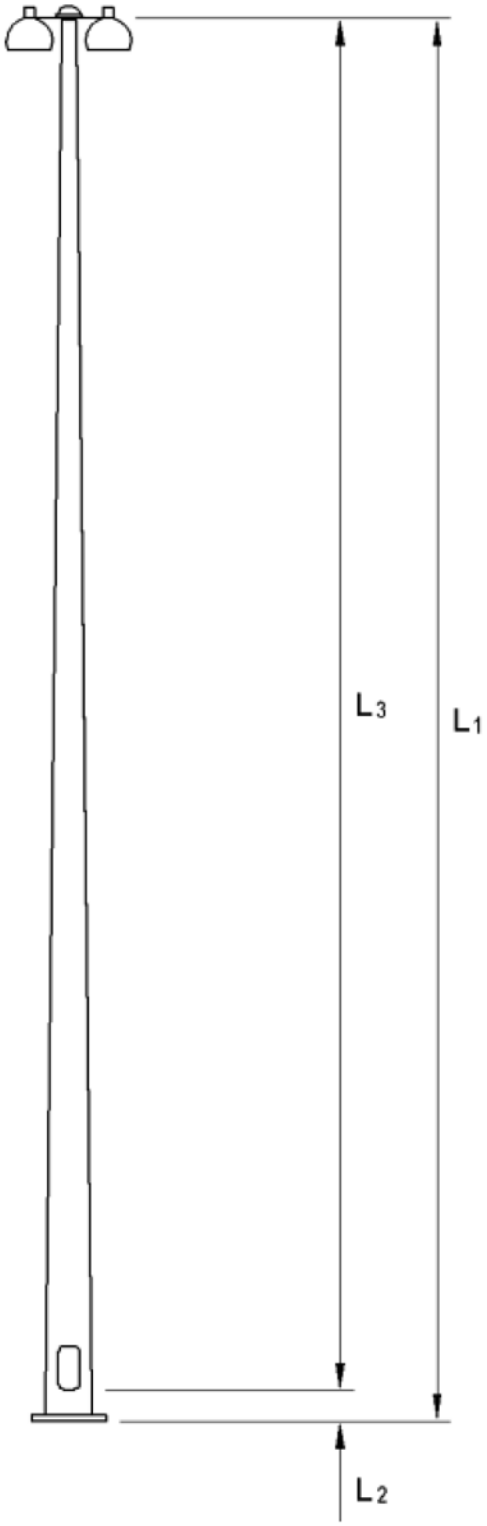

ELEVATION

GENERAL

Description

The support structure for the 160-ft HMLT shown consists of a tapered prismatic tube with access handhole and circular baseplate, and is to be designed for fatigue according to Section 11 of the AASHTO Specifications. The shape of the tube is a regular polygon with 12 sides. The column-to-baseplate connection is groove welded with backing ring attached to the baseplate, and the handhole is reinforced with a fillet-welded stiffening ring. The location of the HMLT is in a region where NOAA data suggest the annual mean wind speed will not exceed 9 mph; however, the lighting plan for the interchange requires the HMLT to be 110 feet from the roadway. Furthermore, it is assumed the structure will not be built with vibration mitigating devices. All calculations shown are in imperial units.

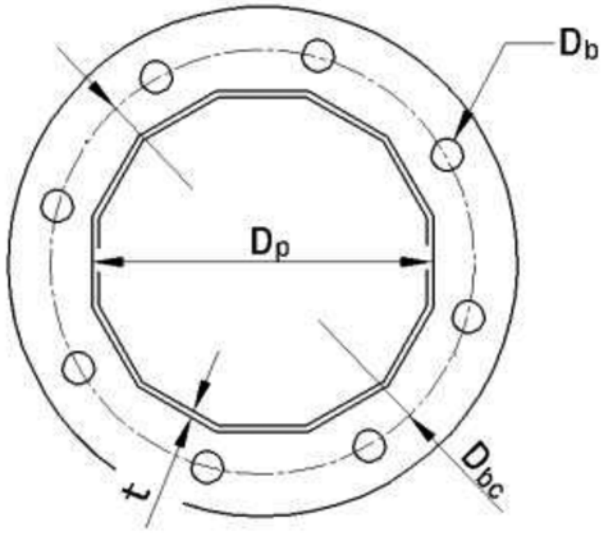

SECTION AT BASEPLATE

Dimensions

Pole

Pole height $L_1 = 160\ ft$

Length from pole baseplate to termination of handhole $L_2 = 1.5\ ft$

Length from termination of handhole to luminaire $L_3 = 158.5\ ft$

Pole diameter at base (across flats) $D_p = 30\ in$

Pole taper rate $\theta = 0.14\ in/ft$

Pole wall thickness t = $0.563\ in$

Anchor Bolts

Number of bolts $n_b = 8$

Bolt group diameter $D_{bg} = 37.5\ in$

Nominal bolt diameter $D_b = 2.25\ in$

Luminaire

Effective projected area on a vertical plane $EPA = 12\ ft^2$

Critical Fatigue Details

The HMLT support structure contains the following details that must be designed for fatigue:

1. Anchor bolts (Detail 5 in Table 11-4)
2. Full-penetration groove welded column-to-baseplate connection with backing ring attached to baseplate (Detail 11 in Table 11-4)
3. Transverse fillet weld at termination of handhole (Detail 20 in Table 11-4)

FATIGUE LOADS

Static Wind Loads

The only load considered for fatigue design of HMLTs is the Combined Wind Effect (Section 11.7.2). Since the pole and the luminaire are subject to different drag coefficients, two separate calculations are made.

Drag coefficient for pole (Table 3-6) $C_d = 1.2$

Drag coefficient for luminaire (Table 3-6) $C_d = 1.0$

Since the height of the HMLT is greater than the distance to the roadway, the HMLT is designed using Importance Category I from Table 11-2. The fatigue-limit-state pressure range is determined from Table 11-3. Even though the annual mean wind speed is expected to be less than 9 mph, the intermediate value must be used.

$$P_{fls} = 6.5\ psf$$

Using Equation 11-7, $P_{CW} = P_{fls} C_d$, calculate the wind effect on the pole and luminaire.

Combined wind effect pressure range applied to pole

$$P_{CW\_Pole} = 6.5\ psf\ (1.2) = 7.8\ psf$$

Combined wind effect pressure range applied to luminaire

$$P_{CW\_Lum} = 6.5\ psf\ (1.0) = 6.5\ psf$$

BENDING MOMENTS

Bending moments are calculated for two different locations: at the base of the pole—to check anchor bolts and column-to-baseplate connection—and at the termination of the handhole.

Calculate length from baseplate to center of pressure of pole

$$L_{CP1} = \frac{L_1\left(D_p - L_1\theta\right) + \frac{1}{3}L_1^2\theta}{2D_p - L_1\theta} = \frac{160\,ft\left[30in - 160\,ft\left(0.14in/\,ft\right)\right] + \frac{1}{3}\left(160\,ft\right)^2\left(0.14in/\,ft\right)}{2\left(30in\right) - 160\,ft\left(0.14in/\,ft\right)} = 64.1\ ft$$

Projected area of pole on a vertical plane

$$A_{p1} = \left(D_p - \frac{1}{2}L_1\theta\right)L_1 = \left[30in - \frac{1}{2}\left(160\,ft\right)\left(0.14in/\,ft\right)\right]\left(160\,ft\right)\left(\frac{ft}{12in}\right) = 251\ ft^2$$

Bending moment at base of pole

$$M_1 = P_{CW\_Pole}A_pL_{CP1} + P_{CW\_Lum}EPA\left(L_1\right) = \frac{7.8psf\left(251ft^2\right)\left(64.1ft\right) + 6.5psf\left(12\,ft^2\right)\left(160\,ft\right)}{1000lb} = 138.0\ k\cdot ft$$

Pole diameter at handhole termination

$$D_{hh} = D_p - L_2\theta = 30in - 1.5\,ft(0.14in/\,ft) = 29.79\ in$$

Calculate length from handhole termination to center of pressure of pole for area above handhole

$$L_{CP2} = \frac{L_3\left(D_{hh} - L_3\theta\right) + \frac{1}{3}L_3^2\theta}{2D_{hh} - L_3\theta}$$

$$= \frac{158.5\,ft\left[29.79in - 158.5\,ft\left(0.14in/\,ft\right)\right] + \frac{1}{3}\left(158.5\,ft\right)^2\left(0.14in/\,ft\right)}{2\left(29.79in\right) - 158.5\,ft\left(0.14in/\,ft\right)} = 63.6\ ft$$

Projected area of pole on a vertical plane above handhole termination

$$A_{p2} = \left(D_{hh} - \frac{1}{2}L_3\theta\right)L_3 = \left[29.79in - \frac{1}{2}\left(158.5\,ft\right)\left(0.14in/\,ft\right)\right]\left(158.5\,ft\right)\left(\frac{ft}{12in}\right) = 247\ ft^2$$

Bending moment at base of pole

$$M_2 = P_{CW\_Pole}A_{p2}L_{CP2} + P_{CW\_Lum}EPA\left(L_3\right)$$

$$= \frac{7.8psf\left(247\,ft^2\right)\left(63.6\,ft\right) + 6.5psf\left(12\,ft^2\right)\left(158.5\,ft\right)}{1000lb} = 134.9k\cdot ft$$

STRESS RANGE CALCULATIONS

Anchor Bolts

For the 2.25-inch diameter anchor bolts chosen, the tensile stress area is 3.25 in^2. The tensile stress area may be found in any steel design manual.

Moment of inertia of bolt group

$$I_{bg} = \frac{n_b R_{bg}^2}{2}$$ where R_{bg} equals the radius of the bolt group, $18.75\ in$.

$$I = \frac{8(18.75in)^2}{2} = 1406\ in^2$$

Maximum applied load range per bolt

$$L_{Rb} = \frac{M_1 R_{bg}}{I_{bg}} = \frac{138.0kft(18.75in)}{1406in^2}(12in/ft) = 22.1\ k/bolt$$

Anchor bolt stress range $(S_R)_b = 22.1\ k/3.25\ in^2 = 6.80\ ksi$

Anchor bolts are classified as Category D details for infinite life (Detail 5 in Table 11-4). The CAFL corresponding to Category D is 7.0 ksi. Since the calculated stress range (6.80 ksi) is less than the CAFL (7.0 ksi), the anchor bolt group is adequate for fatigue.

Column-to-Baseplate Connection

The section modulus for various tubular shapes can be determined using the equations given in Appendix B of the specification. For the 12-sided pole given

$$S = 3.29R^2t$$

where R equals the radius of the tube measured to the mid-thickness of the wall.

Radius of pole at its base, measured to mid-thickness of wall

$R = (30 - 0.563\ in)/2 = 14.72\ in$

Section modulus of pole at its base $S_p = 3.29(14.72\ in)^2(0.563\ in) = 401\ in^3$

Stress range at pole base

$$(S_R)_p = \frac{M_1}{S_p} = \frac{138.0kft}{401in^3}(12in/ft) \qquad (S_R)_p = 4.13\ ksi$$

A groove welded column-to-baseplate connection *with* backing ring is classified as a Category E fatigue detail (Detail 11 in Table 11-4). The CAFL corresponding to Category E is 4.5 ksi. Since the calculated stress range (4.13 ksi) is less than the CAFL (4.5 ksi), the detail is adequate for fatigue.

Transverse Fillet Weld at Handhole

The diameter of the pole at the location of the transverse fillet weld is 29.79 inches as calculated above.

Radius of pole at the location of the transverse fillet weld, measured to mid-thickness of wall

$$R = (29.79 - 0.563\ in)/2 = 14.61\ in$$

Section modulus of pole at its base $S_{hh} = 3.29(14.61\ in)^2(0.563\ in) = 396\ in^3$

Stress range at pole base

$$(S_R)_{hh} = \frac{M_2}{S_{hh}} = \frac{134.9 kft}{396 in^3}\left(12 in / ft\right) \qquad (S_R)_{hh} = 4.09\ ksi$$

Assuming the length of the handhole is greater than 4 inches, the handhole detail is considered Category E for fatigue (Detail 20 in Table 11-4). The CAFL corresponding to Category E is 4.5 ksi. Since the calculated stress range (4.09 ksi) is less than the CAFL (4.5 ksi), the detail is adequate for fatigue.

EXAMPLE 5

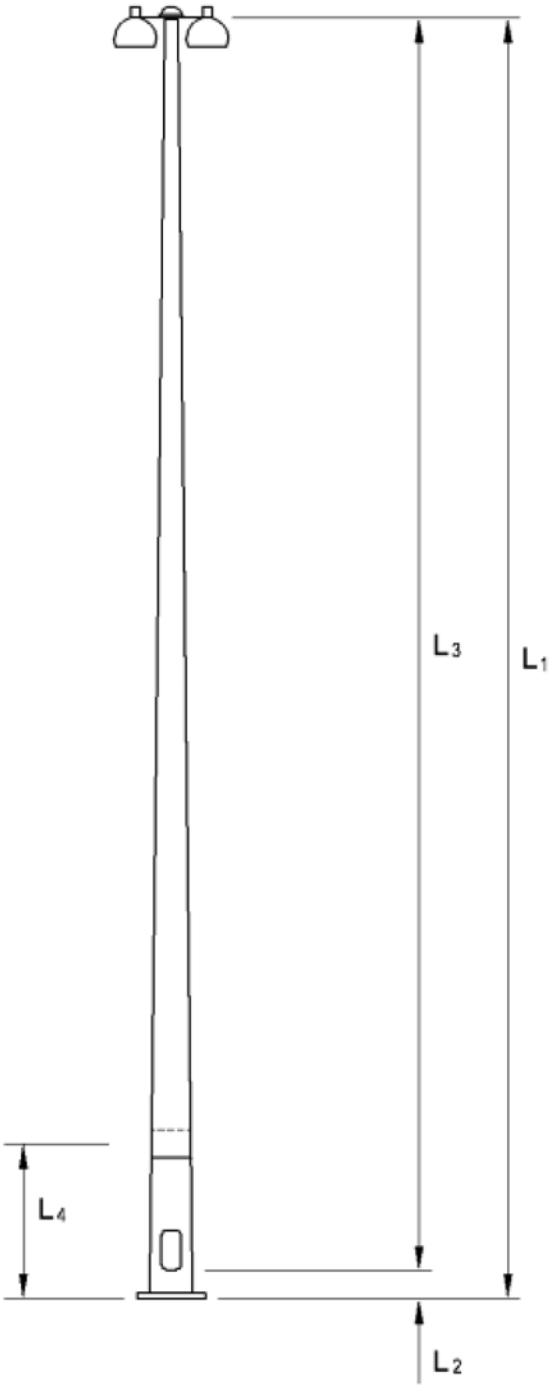

ELEVATION

GENERAL

Description

The support structure for the 160-ft HMLT shown consists of a tapered prismatic tube with access handhole and circular baseplate, and is to be designed for fatigue according to Section 11 of the AASHTO Specification. The shape of the tube is a regular polygon with 16 sides. The column-to-baseplate connection is groove welded with the backing ring attached to the baseplate, and the handhole detail is of the "doubler" plate type. The location of the HMLT is in a region where the annual mean wind speed is expected to exceed 11 mph, and the lighting plan for the interchange requires the HMLT to be 100 ft from the roadway. Considering the height of the HMLT and anticipated wind load, a slip-joint is located near the bottom of the pole to allow for a more economical design. Furthermore, it is assumed the structure will not be built with vibration mitigating devices. All calculations shown are in imperial units.

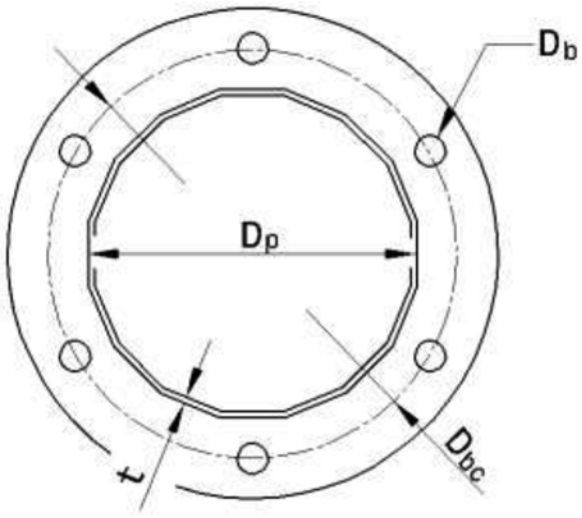

SECTION AT BASEPLATE

Dimensions

Pole

Pole height
$L_1 = 160\ ft$
Length from pole baseplate to termination of handhole $L_2 = 1.5\ ft$
Length from termination of handhole to luminaire $L_3 = 158.5\ ft$
Length from pole baseplate to slip-joint
$L_4 = 12\ ft$
Pole diameter at base (across flats)
$D_p = 30\ in$
Pole taper rate
$\theta = 0.14\ in/ft$
Pole wall thickness at base
$t_1 = 0.625\ in$
Pole wall thickness above slip-joint
$t_2 = 0.25\ in$

Anchor Bolts

Number of bolts
$n_b = 8$
Bolt group diameter
$D_{bg} = 37\ in$
Nominal bolt diameter
$D_b = 2.50\ in$

Luminaire

Effective projected area on a vertical plane
$EPA = 16\ ft^2$

Critical Fatigue Details

The HMLT support structure contains the following details that must be designed for fatigue:

1. Anchor bolts (Detail 5 in Table 11-4)
2. Full-penetration groove welded column-to-baseplate connection with backing ring attached to baseplate (Detail 11 in Table 11-4)
3. Transverse fillet weld at termination of handhole (Detail 3.5 in Table 6.6.1.2.3-1 in AASHTO LRFD)
4. Slip-joint splice (Detail 2 in Table 11-4)

FATIGUE LOADS

Static Wind Loads

The only load considered for fatigue design of HMLTs is the Combined Wind Effect (Section 11.7.2). Since the pole and the luminaire are subject to different drag coefficients, two separate calculations are made.

Drag coefficient for pole (Table 3-6) $C_d = 1.1$
Drag coefficient for luminaire (Table 3-6) $C_d = 1.0$

The fatigue-limit-state pressure range is determined from Table 11-3. Considering the proximity of the HMLT with the roadway, and the high mean wind speed, the maximum value must be used.

$$P_{fls} = 7.4\ psf$$

Using Equation 11-7, $P_{CW} = P_{fls}C_d$, calculate the wind effect on the pole and luminaire.

Combined wind effect pressure range applied to pole

$$P_{CW\_Pole} = 7.2\ psf\ (1.1) = 7.9\ psf$$

Combined wind effect pressure range applied to luminaire

$$P_{CW\ Lum} = 7.2\ psf\ (1.0) = 7.2\ psf$$

BENDING MOMENTS

Bending moments are calculated at three different locations at the base of the pole—to check anchor bolts and column-to-baseplate connection—at the termination of the handhole, and at the slip-joint.

Calculate length from baseplate to center of pressure of pole

$$L_{CP1} = \frac{L_1\left(D_p - L_1\theta\right) + \frac{1}{3}L_1^2\theta}{2D_p - L_1\theta} = \frac{160\,ft\left[30in - 160\,ft\left(0.14in/\,ft\right)\right] + \frac{1}{3}\left(160\,ft\right)^2\left(0.14in/\,ft\right)}{2\left(30in\right) - 160\,ft\left(0.14in/\,ft\right)} = 64.1\ ft$$

Projected area of pole on a vertical plane

$$A_{p1} = \left(D_p - \frac{1}{2}L_1\theta\right)L_1 = \left[30in - \frac{1}{2}\left(160\,ft\right)\left(0.14in/\,ft\right)\right]\left(160\,ft\right)\left(\frac{1}{12}\right) = 251\ ft^2$$

Bending moment at base of pole

$$M_1 = P_{CW\_Pole}A_pL_{CP1} + P_{CW\_Lum}EPA\left(L_1\right) = \frac{7.9\,psf\left(251\,ft^2\right)\left(64.1\,ft\right) + 7.2\,psf\left(16\,ft^2\right)\left(160\,ft\right)}{1000lb} = 145.5\,k\cdot ft$$

Pole diameter at handhole termination

$$D_{hh} = D_p - L_2\theta = 30in - 1.5\,ft(0.14in/\,ft) = 29.79\ in$$

Calculate length from handhole termination to center of pressure of pole for area above handhole

$$L_{CP2} = \frac{L_3\left(D_{hh} - L_3\theta\right) + \frac{1}{3}L_3^2\theta}{2D_{hh} - L_3\theta}$$

$$= \frac{158.5\,ft\left[29.79in - 158.5\,ft\left(0.14in/\,ft\right)\right] + \frac{1}{3}\left(158.5\,ft\right)^2\left(0.14in/\,ft\right)}{2\left(29.79in\right) - 158.5\,ft\left(0.14in/\,ft\right)} = 63.6\ ft$$

Projected area of pole on a vertical plane above handhole termination

$$A_{p2} = \left(D_{hh} - \frac{1}{2}L_3\theta\right)L_3 = \left[29.79in - \frac{1}{2}\left(158.5\,ft\right)\left(0.14in/\,ft\right)\right]\left(158.5\,ft\right)\left(\frac{ft}{12in}\right) = 247\ ft^2$$

Bending moment at termination of handhole

$$M_2 = P_{CW\_Pole} A_{p2} L_{CP2} + P_{CW\_Lum} EPA(L_3)$$
$$= \frac{7.9\,psf\left(247\,ft^2\right)(63.6\,ft) + 7.2\,psf\left(16\,ft^2\right)(158.5\,ft)}{1000lb} = 142.4k \cdot ft$$

Pole diameter at slip-joint

$$D_{sj} = D_p - L_4\theta = 30in - 12\,ft(0.14in/\,ft) = 28.32\,in$$

Calculate length from slip-joint to center of pressure of pole for area above slip-joint. Let L_5 equal the length from the slip-joint to the luminaire ($148\,ft$).

$$L_{CP3} = \frac{L_5\left(D_{sj} - L_5\theta\right) + \frac{1}{3}L_5^2\theta}{2D_{sj} - L_5\theta} = \frac{148\,ft\left[28.32in - 148\,ft\left(0.14in/\,ft\right)\right] + \frac{1}{3}\left(148\,ft\right)^2\left(0.14in/\,ft\right)}{2\left(28.32in\right) - 148\,ft\left(0.14in/\,ft\right)} = 59.8\,ft$$

Projected area of pole on a vertical plane above slip-joint

$$A_{p3} = \left(D_{sj} - \frac{1}{2}L_5\theta\right)L_5 = \left[28.32in - \frac{1}{2}(148\,ft)(0.14in/\,ft)\right](148\,ft)\left(\frac{ft}{12in}\right) = 222\ ft^2$$

Bending moment at slip-joint

$$M_3 = P_{CW\_Pole} A_{p2} L_{CP2} + P_{CW\_Lum} EPA(L_5) = \frac{7.9\,psf\left(222\,ft^2\right)(59.8\,ft) + 7.2\,psf\left(16\,ft^2\right)(148\,ft)}{1000lb} = 121.9k \cdot ft$$

STRESS RANGE CALCULATIONS

Anchor Bolts

For the 2.50-inch diameter anchor bolts chosen, the tensile stress area is $4.00\ in^2$. The tensile stress area may be found in any steel design manual.

Moment of inertia of bolt group

$$I_{bg} = \frac{n_b R_{bg}^2}{2}$$ where R_{bg} equals the radius of the bolt group, $18.5\ in$.

$$I = \frac{8\left(18.5in\right)^2}{2} = 1369\ in^2$$

Maximum applied load range per bolt

$$L_{Rb} = \frac{M_1 R_{bg}}{I_{bg}} = \frac{145.5kft\left(18.5in\right)}{1369in^2}\left(12in/\,ft\right) = 23.6\ k/bolt$$

Anchor bolt stress range $(S_R)_b = 23.6\ k/4.00\ in^2 = 5.90\ ksi$

Anchor bolts are classified as Category D details for infinite life (Detail 5 in Table 11-4). The CAFL corresponding to Category D is 7.0 ksi. Since the calculated stress range (5.90 ksi) is less than the CAFL (7.0 ksi), the anchor bolt group is adequate for fatigue.

Column-to-Baseplate Connection

The section modulus for various tubular shapes can be determined using the equations given in Appendix B of the specification. For the 16-sided pole given

$$S = 3.22R^2t$$

where R equals the radius of the tube measured to the mid-thickness of the wall.

Radius of pole at its base, measured to mid-thickness of wall

$$R = (30 - 0.625\ in)/2 = 14.69\ in$$

Section modulus of pole at its base

$$S_p = 3.22(14.69\ in)^2(0.625\ in) = 434\ in^3$$

Stress range at pole base

$$(S_R)_p = \frac{M_1}{S_p} = \frac{145.5kft}{434in^3}\left(12in/ft\right) \qquad (S_R)_p = 4.02\ ksi$$

A groove welded column-to-baseplate connection *with* backing ring is classified as a Category E fatigue detail (Detail 11 in Table 11-4). The CAFL corresponding to Category E is 4.5 ksi. Since the calculated stress range (4.08 ksi) is less than the CAFL (4.5 ksi), the detail is adequate for fatigue.

Transverse Fillet Weld at Handhole

A detail of the doubler plate handhole reinforcement is shown below. The area with greatest potential for crack growth is the transverse fillet weld across the bottom of the plate.

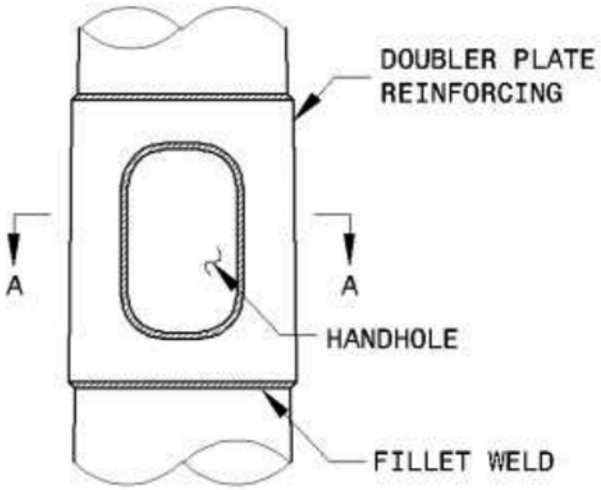

The diameter of the pole at the location of the transverse fillet weld is 29.79 inches as calculated above.

Radius of pole at the location of the transverse fillet weld, measured to mid-thickness of wall

$$R = (29.79 - 0.625\ in)/2 = 14.58\ in$$

Section modulus of pole at its base $S_{hh} = 3.22(14.58\ in)^2(0.625\ in) = 428\ in^3$

Stress range at termination of handhole

$$(S_R)_{hh} = \frac{M_2}{S_{hh}} = \frac{142.4kft}{428in^3}\left(12in/\ ft\right) \qquad (S_R)_{hh} = 3.99\ ksi$$

Assuming the length of the handhole is greater than 4 inches, the handhole detail is considered Category E for fatigue (Detail 20 in Table 11-4). The CAFL corresponding to Category E is 4.5 ksi. Since the calculated stress range (3.99 ksi) is less than the CAFL (4.5 ksi), the detail is adequate for fatigue.

Slip-Joint

The diameter of the pole at the location of the slip-joint is 28.32 inches as calculated above. The section modulus for various tubular shapes can be determined using the equations given in Appendix B of the specification. For the 16-sided pole given

$$S = 3.22R^2t$$

where R equals the radius of the tube measured to the mid-thickness of the wall.

Radius of pole at the slip-joint, measured to mid-thickness of wall

$$R = (28.32 - 0.25\ in)/2 = 14.04\ in$$

Section modulus of pole at its base $S_{sj} = 3.22(14.04\ in)^2(0.25\ in) = 158.6\ in^3$

Stress range at pole base

$$(S_R)_{sj} = \frac{M_3}{S_{sj}} = \frac{121.9kft}{158.6in^3}\left(12in/\ ft\right) \qquad (S_R)_p = 9.22\ ksi$$

A slip-joint splice is classified as a Category B fatigue detail (Detail 2 in Table 11-4). The CAFL corresponding to Category B is 16 ksi. Since the calculated stress range (9.22 ksi) is less than the CAFL (16 ksi), the detail is adequate for fatigue.

APPENDIX B

Proposed Specification and Commentary

SECTION 11: FATIGUE DESIGN

TABLE OF CONTENTS

11.1—SCOPE 11-1

11.2—DEFINITIONS 11-1

11.3—NOTATION 11-1

11.4—APPLICABLE STRUCTURE TYPES 11-3

11.5—DESIGN CRITERIA 11-3

11.6—FATIGUE IMPORTANCE FACTORS 11-5

11.7—FATIGUE DESIGN LOADS 11-8

11.7.1—Sign and Traffic Signal Structures 11-8

11.7.1.1—Galloping 11-9

11.7.1.2—Vortex Shedding 11-11

11.7.1.3 ~~11.7.3~~—Natural Wind Gust 11-13

11.7.1.4 ~~11.7.4~~—Truck-Induced Gust 11-14

11.7.2—High-mast Lighting Towers 11-15

11.8—DEFLECTION 11-17

11.9—FATIGUE RESISTANCE 11-18

11.10—REFERENCES 11-28

SECTION 11:

FATIGUE DESIGN

11.1—SCOPE

This Section contains provisions for the fatigue design of cantilevered and noncantilevered steel and aluminum structural supports for highway signs, luminaires, and traffic signals.

C11.1

This Section focuses on fatigue, which is defined herein as the damage that may result in fracture after a sufficient number of stress fluctuations. It is based on NCHRP Report 412, *Fatigue Resistant Design of Cantilevered Signal, Sign and Light Supports* (Kaczinski et al., 1998), NCHRP Report 469, *Fatigue-Resistant Design of Cantilever Signal, Sign, and Light Supports* (Dexter and Ricker, 2002), and NCHRP Report 494, *Structural Supports for Highway Signs, Luminaires, and Traffic Signals* (Fouad et al., 2003), NCHRP Project 10-74, *Development of Fatigue Loading and Design Methodology for High-Mast Light Poles* (Connor et al, 2012).

11.2—DEFINITIONS

Constant-Amplitude Fatigue Limit (CAFL)—Nominal stress range below which a particular fatigue detail can withstand an infinite number of repetitions without fatigue failure.

Fatigue—Damage resulting in fracture caused by stress fluctuations.

In-Plane Bending—Bending in-plane for the main member (column). At the connection of an arm or arm's built-up box to a vertical column, the in-plane bending stress range in the column is a result of galloping or truck-induced gust loads on the arm and/or arm's attachments.

Limit State Wind Load Effect—A specifically defined load criteria.

Load-Bearing Attachment—Attachment to main member where there is a transverse load range in the attachment itself in addition to any primary stress range in the main member.

Nonload-Bearing Attachment—Attachment to main member where the only significant stress range is the primary stress in the main member.

Out-of-Plane Bending—Bending out-of-plane for the main member (column). At the connection of an arm or arm's built-up box to a vertical column, the out-of-plane bending stress range in the column is a result of natural wind-gust loads on the arm and the arm's attachments.

Pressure Range—Pressure due to a limit state wind load effect that produces a stress range.

Stress Range—The algebraic difference between extreme stresses used in fatigue design.

Yearly Mean Wind Velocity—Long-term average of the wind speed for a given area.

HMLT – Acronym for high-mast lighting tower

11.3—NOTATION

b = flat-to-flat width of a multisided section (m, ft)
C_d = appropriate drag coefficient from Section 3, "Loads," for given attachment or member
d = diameter of a circular section (m, ft)
D = inside diameter of exposed end of female section for slip-joint splice (mm, in.)
E = modulus of elasticity (MPa, ksi)
f_n = first natural frequency of the structure (cps)

f_{n1} = first modal frequency (cps)
$(F)_n$ = fatigue strength (CAFL) (MPa, ksi)
g = acceleration of gravity (9810 mm/s^2, 386 in./s^2)
H = effective weld throat (mm, in.)
I = moment of inertia (mm^4, in.^{4})
I_{avg} = average moment of inertia for a tapered pole (mm^4, in.^{4})
I_{top} = moment of inertia at top of tapered pole (mm^4, in.^{4})
I_{bottom} = moment of inertia at bottom of tapered pole (mm^4, in.^{4})
I_F = fatigue importance factors applied to limit state wind load effects to adjust for the desired level of structural reliability
L = length of the pole (Article 11.7.2) (mm, in.)
L = slip-splice overlap length (example 1 of Figure ~~11-1~~11-2) (mm, in.)
L = length of reinforcement at handhole (example 13 of Figure ~~11-1~~11-2) (mm, in.)
L = length of longitudinal attachment (examples 12, 14, and 15 of Figure ~~11-1~~11-2) (mm, in.)
P_{CW} = combined wind pressure range for fatigue design of HMLTs (Pa, psf)
P_{FLS} = fatigue-limit-state wind pressure range for fatigue design of HMLTs (Pa, psf)
P_G = galloping-induced vertical shear pressure range (Pa, psf)
P_{NW} = natural wind gust pressure range (Pa, psf)
P_{TG} = truck-induced gust pressure range (Pa, psf)
P_{VS} = vortex shedding-induced pressure range (Pa, psf)
r = radius of chord or column (mm, in.)
R = transition radius of longitudinal attachment (mm, in.)
S_n = Strouhal number
S_R = nominal stress range of the main member or branching member (MPa, ksi)
t = thickness (mm, in.)
t_b = wall thickness of branching member (mm, in.)
t_c = wall thickness of main member (column) (mm, in.)
t_p = plate thickness of attachment (mm, in.)
V_c = critical wind velocity for vortex shedding (m/s, mph)
V_{mean} = yearly mean wind velocity for a given area (m/s, mph)
V_T = truck speed for truck-induced wind gusts (m/s, mph)
W = weight of the luminaire (N, k)
w = weight of the pole per unit length (N/mm, k/in.)
β = damping ratio
α = angle of transition taper of longitudinal attachment (example 14 of Figure ~~11-1~~11-2) (°)
α = ovalizing parameter for bending in the main member (note b of Table ~~11-2~~11-4)
ΔF = constant amplitude fatigue limit stress range (MPa, ksi)
$\Delta\sigma$ = indication of stress range in member

11.4—APPLICABLE STRUCTURE TYPES

Design for fatigue shall be required for the following type structures:

a. overhead cantilevered sign structures,

b. overhead cantilevered traffic signal structures,

c. high-level, high-mast lighting structures,

d. overhead noncantilevered sign structures, and

e. overhead noncantilevered traffic signal structures.

C11.4

NCHRP Report 412 is the basis for the fatigue design provisions for cantilevered structures. NCHRP Report 494 is the basis for the fatigue design provisions for noncantilevered support structures. The fatigue design procedures outlined in this Section may be applicable to steel and aluminum structures in general. However, only specific types of structures are identified for fatigue design in this Article. Common lighting poles and roadside signs are not included because they are smaller structures and normally have not exhibited fatigue problems. An exception would be square lighting poles, as they have exhibited poor fatigue performance. Square cross-sections have been much more prone to fatigue problems than round cross-sections. Caution should be exercised regarding the use of square lighting poles even when a fatigue design is performed. The provisions of this Section are not applicable for the design of span-wire (strain) poles.

11.5—DESIGN CRITERIA

Cantilevered and noncantilevered support structures shall be designed for fatigue to resist each of the applicable equivalent static wind load effects specified in Article 11.7, and modified by the appropriate fatigue importance factors given in Article 11.6. Stresses due to these loads on all components, mechanical fasteners, and weld details shall be limited to satisfy the requirements of their respective detail categories within the constant-amplitude fatigue limits (CAFL) provided in Article 11.9.

C11.5

Accurate load spectra and life prediction techniques for defining fatigue loadings are generally not available. The assessment of stress fluctuations and the corresponding number of cycles for all wind-induced events (lifetime loading histogram) is practically impossible. With this uncertainty, the design of sign, luminaire, and traffic signal supports for a finite fatigue life becomes impractical. Therefore, an *infinite life* fatigue design approach is recommended and is considered sound practice. Fatigue stress limits are based on the CAFL. The CAFL values provided in Table ~~11-3~~11-5 are approximately the same as those given in Table ~~10.3.1A of the *Standard Specifications for Highway Bridges*~~6.6.1.2.5-3 of the *LRFD Bridge Design Specifications*.

An *infinite life* fatigue approach was developed in an experimental study that considered several critical welded details (Fisher et al. 1993). The *infinite life* fatigue approach can be used when the number of wind load cycles expected during the lifetime of the structures is greater than the number of cycles at the CAFL. This is particularly the case for structural supports where the wind load cycles in 25 years or greater lifetimes are expected to exceed 100 million cycles, whereas typical weld details reach the CAFL at 10 to 20 million cycles.

Fatigue-critical details are designed with nominal stress ranges that are below the appropriate CAFL. To assist designers, typical support structure details based on AASHTO and American Welding Society (AWS) fatigue design categories are provided in Table ~~11-2~~11-4 and Figure ~~11-1~~11-2. The above-referenced details were produced based on a review of state departments of transportation standard drawings and manufacturers' literature. This list should not be considered a complete set of all possible connection details, but rather it is intended to remove the uncertainty associated with applying the provisions of the ~~*Standard Specifications for Highway Bridges*~~ *LRFD Bridge Design Specifications* to the fatigue design of support structures. Choice of details improves the fatigue resistance of these structures, and it can eliminate or reduce increases in member size required for less fatigue-resistant details.

The notes for Table ~~11-2~~11-4 specify the use of Stress Category K_2. This stress category corresponds to the category for cyclic punching shear stress in tubular members specified by the *AWS Structural Welding Code D1.1—Steel*. Fatigue design for the column's wall under this condition may require sizes of the built-up box connection or column wall thicknesses that are excessive for practical use. For this occurrence, an adequate fatigue-resistant connection other than the built-up box shown in Figure ~~11-1~~11-2 should be considered.

Fatigue testing has shown the advantage of ring stiffeners that completely encircle a pole relative to a built-up box connection. For built-up box connections, it is recommended that the width of the box be the same as the diameter of the column (i.e., the sides of the box are tangent to the sides of the column).

Regarding full-penetration groove-welded tube-to-transverse plate connections, NCHRP Report 412 did not fully investigate the effects from the possible use of additional reinforcing fillet welds. Additional research and testing of these types of detail configurations are needed to support future updates of this Section.

Stress categories in Table ~~11-2~~11-4 for weld terminations at the end of longitudinal stiffeners were based, in part, on assigned categories for attachments in the AASHTO Bridge Specifications. Fatigue testing of many fillet-welded tube-to-longitudinal stiffener connections indicates that the angle of intersection, the transitional radius to the pole wall, the length of the stiffener, and the ratio of the stiffener thickness to pole wall thickness, for example, all have effects on the fatigue life of the detail. Some tube-to-stiffener connections have a potential to develop high stress concentrations in the tube wall in the vicinity of the weld termination at the end of longitudinal stiffeners. Testing on poles having wall thickness less than 6 mm (0.25 in.) indicates that longitudinal stiffeners yielded little or no improvement of the fatigue performance of the connection (Koenigs et al., 2003). Until further research can give reliable estimates of the effects of stiffeners, all welds terminating at the end of longitudinal stiffeners shall be classified as Stress Category E′.

11.6—FATIGUE IMPORTANCE FACTORS

A fatigue importance factor, I_F, that accounts for the risk of hazard to traffic and damage to property shall be applied to the limit state wind-load effects specified in Article 11.7. Fatigue importance factors for traffic signal, sign, and luminaire support structures exposed to the four wind load effects are presented in Table 11-1.

The importance categories given in Table 11-2 shall be used for high-mast lighting towers.

Equal leg welds in socket connections have been shown by fatigue testing to have a fatigue strength less than Stress Category E′. The fatigue strength of a socket-welded connection can be improved by using an unequal leg fillet weld.

C11.6

Fatigue importance factors are introduced into the Specifications to adjust the level of structural reliability of cantilevered and noncantilevered support structures. Fatigue importance factors should be determined by the Owner. For combined structures, where traffic signals and luminaires are joined, the use of the more conservative fatigue importance factor is recommended.

The importance categories and fatigue importance factors found in Table 11-1 (rounded to the nearest 0.05) are results from NCHRP Reports 469 and 494. Three categories of support structures are presented in Table 11-1. Structures classified as Category I present a high hazard in the event of failure and should be designed to resist rarely occurring wind loading and vibration phenomena. It is recommended that all structures without effective mitigation devices on roadways with a speed limit in excess of 60 km/hr (35 mph) and average daily traffic (ADT) exceeding 10 000 or average daily truck traffic (ADTT) exceeding 1000 should be classified as Category I structures. ADT and ADTT are for one direction regardless of the number of lanes.

Structures without mitigation devices may be classified as Category I if any of the following apply:

1. Cantilevered sign structures with a span in excess of 16 m (50 ft) ~~or high-mast towers in excess of 30 m (100 ft),~~
2. Large sign structures, both cantilevered and noncantilevered, including variable message signs, and
3. Structures located in an area that is known to have wind conditions that are conducive to vibration.

Structures should be classified as Category III if they are located on roads with speed limits of 60 km/hr (35 mph) or less. Structures that are located such that a failure will not affect traffic may be classified as Category III.

All structures not explicitly meeting the Category I or Category III criteria should be classified as Category II.

Maintenance and inspection programs should be considered integral to the selection of the fatigue importance category.

There are many factors that affect the selection of the fatigue category and engineering judgment is required.

The fatigue importance factors for HMLTs found in Table 11-2 are based on the research conducted as part of NCHRP 10-74. The importance factors for HMLTs have been separated and simplified from those in Table 11-1. Since HMLTs are generally only used on high ADTT roadways, whether a pole can or cannot fall in the path of traffic is selected as the critical parameter..

Table 11–1—Fatigue Importance Factors, I_F

Fatigue Category			Fatigue Importance Factor, I_F			
			Galloping	Vortex Shedding	Natural Wind Gusts	Truck-Induced Gusts
Cantilevered	I	Sign	1.0	x*	1.0	1.0
		Traffic Signal	1.0	x*	1.0	1.0
		Lighting	x	1.0	1.0	x
	II	Sign	0.70	x*	0.85	0.90
		Traffic Signal	0.65	x*	0.80	0.85
		Lighting	x	0.65	0.75	x
	III	Sign	0.40	x*	0.70	0.80
		Traffic Signal	0.30	x*	0.55	0.70
		Lighting	x	0.30	0.50	x
Noncantilevered	I	Sign	x	x*	1.0	1.0
		Traffic Signal	x	x*	1.0	1.0
	II	Sign	x	x*	0.85	0.90
		Traffic Signal	x	x*	0.80	0.85
	III	Sign	x	x*	0.70	0.80
		Traffic Signal	x	x*	0.55	0.70

Notes:

x Structure is not susceptible to this type of loading.

* Overhead cantilevered and noncantilevered sign and traffic signal components are susceptible to vortex shedding prior to placement of the signs and traffic signal heads, i.e., during construction.

Table 11-2—Fatigue Importance Categories for HMLTs

Hazard Level	Importance Category
High (distance to roadway ≤ height of HMLT)	I
Low (distance to roadway > height of HMLT)	II

11.7—FATIGUE DESIGN LOADS

To avoid large-amplitude vibrations and to preclude the development of fatigue cracks in various connection details and at other critical locations, cantilevered and noncantilevered support structures shall be designed to resist each of the following applicable limit state equivalent static wind loads acting separately. These loads shall be used to calculate nominal stress ranges near fatigue-sensitive connection details described in Article 11.5 and deflections for service limits described in Article 11.8.

In lieu of using the equivalent static pressures provided in this Specification, a dynamic analysis of the structure may be performed using appropriate dynamic load functions derived from reliable data.

Fatigue loading provisions for high-mast lighting towers (HMLTs) are differentiated from those associated with other traffic structures. HMLTs shall be designed for the loading given in Article 11.7.2.

11.7.1—Sign and Traffic Signal Structures

Equivalent static wind loads for the fatigue design of sign and traffic signal structures shall be determined from Articles 11.7.1.1 through 11.7.1.4 as applicable. The structures included in this section are defined in Article 11.5 and the associated commentary.

C11.7

Cantilevered and noncantilevered support structures are exposed to several wind phenomena that can produce cyclic loads. Vibrations associated with these cyclic forces can become significant. NCHRP Report 412 identified galloping, vortex shedding, natural wind gusts, and truck-induced gusts as wind-loading mechanisms that can induce large-amplitude vibrations and/or fatigue damage in cantilevered traffic signal, sign, and light support structures. NCHRP Report 494 identified natural wind gusts and truck-induced gusts as wind-loading mechanisms that can induce large-amplitude vibrations and/or fatigue damage in noncantilevered traffic signal and sign support structures. The amplitude of vibration and resulting stress ranges are increased by the low levels of stiffness and damping possessed by many of these structures. In some cases, the vibration is only a serviceability problem because motorists cannot clearly see the mast arm attachments or are concerned about passing under the structures. In other cases, where deflections may or may not be considered excessive, the magnitudes of stress ranges induced in these structures have resulted in the development of fatigue cracks at various connection details including the anchor bolts.

The provisions for fatigue loading of HMLTs is based on the research conducted as part of NCHRP Project 10-74, which developed a loading spectrum inclusive of all applicable load effects due to natural wind.

The wind-loading phenomena specified in this section possess the greatest potential for creating large-amplitude vibrations in cantilevered support structures. In particular, galloping and vortex shedding are aeroelastic instabilities that typically induce vibrations at the natural frequency of the structure (i.e., resonance). These conditions can lead to fatigue failures in a relatively short period of time.

Design pressures for ~~four~~fatigue wind-loading mechanisms are presented as an equivalent static wind pressure range, or a shear stress range in the case of galloping. These pressure (or shear stress) ranges should be applied as prescribed by static analysis to determine stress ranges near fatigue-sensitive details. In lieu of designing for galloping or vortex-shedding limit state fatigue wind load effects, mitigation devices may be used as approved by the Owner. Mitigation devices are discussed in NCHRP Reports ~~412 and 469~~412, 469, and 10-74.

C11.7.1

11.7.1.1—Galloping

Overhead cantilevered sign and traffic signal support structures shall be designed for galloping-induced cyclic loads by applying an equivalent static shear pressure vertically to the surface area, as viewed in normal elevation of all sign panels and/or traffic signal heads and backplates rigidly mounted to the cantilevered horizontal support. The vertical shear pressure range shall be equal to the following:

$$P_G = 1000 I_F \quad \text{(Pa)} \qquad (11\text{-}1)$$

$$P_G = 21 I_F \quad \text{(psf)}$$

In lieu of designing to resist periodic galloping forces, cantilevered sign and traffic signal structures may be erected with effective vibration mitigation devices. Vibration mitigation devices should be approved by the Owner, and they should be based on historical or research verification of its vibration damping characteristics.

Alternatively, for traffic signal structures, the Owner may choose to install approved vibration mitigation devices if structures exhibit a galloping problem. The mitigation devices should be installed as quickly as possible after the galloping problem appears.

The Owner may choose to exclude galloping loads for the fatigue design of overhead cantilevered sign support structures with quadri-chord (i.e., four-chord) horizontal trusses.

C11.7.1.1

Galloping, or Den Hartog instability, results in large-amplitude, resonant oscillations in a plane normal to the direction of wind flow. It is usually limited to structures with nonsymmetrical cross-sections, such as sign and traffic signal structures with attachments to the horizontal cantilevered arm. Structures without attachments to the cantilevered horizontal arm support are not susceptible to galloping-induced wind load effects.

The results of wind tunnel (Kaczinski et al., 1998) and water tank (McDonald et al., 1995) testing, as well as the oscillations observed on cantilevered support structures in the field, are consistent with the characteristics of the galloping phenomena. These characteristics include the sudden onset of large-amplitude, across-wind vibrations that increase with increases in wind velocity. Galloping is typically not caused by wind applied to the support structure, but rather applied to the attachments to the horizontal cantilevered arm, such as signs and traffic signals.

The geometry and orientation of these attachments, as well as the wind direction, directly influence the susceptibility of cantilevered support structures to galloping. Traffic signals are more susceptible to galloping when configured with a backplate. In particular, traffic signal attachments configured with or without a backplate are more susceptible to galloping when subject to flow from the rear. Galloping of sign attachments is independent of aspect ratio and is more prevalent with wind flows from the front of the structure.

By conducting wind tunnel tests and analytical calibrations to field data and wind tunnel test results, an equivalent static vertical shear of 1000 Pa (21 psf) was determined for the galloping phenomenon. This vertical shear range should be applied to the entire frontal area of each of the sign and traffic signal attachments in a static analysis to determine stress ranges at critical connection details. For example, if a 2.5 × 3.0 m (8 × 10 ft) sign panel is mounted to a horizontal mast arm, a static force of $7500 \times I_F$, N ($1680 \times I_F$, lb) should be applied vertically at the area centroid of the sign panel. A study (Florea et al, 2007) has shown that the equivalent static force that an attachment experiences depends on the location along the arm where it is attached. Equivalent static pressures or vertical shear ranges applied to the frontal area of each sign or traffic signal attachment are greater towards the tip of the mast arm. The specification does not consider the effect of the attachment location when calculating the galloping force. Further testing is necessary to verify this and to suggest location-specific ranges.

A pole with multiple horizontal cantilevered arms may be designed for galloping loads applied separately to each individual arm, and need not consider galloping simultaneously occurring on multiple arms.

Overhead cantilevered sign support structures with quadri-chord horizontal trusses do not appear to be susceptible to galloping because of their inherent stiffness.

Two possible means exist to mitigate galloping-induced oscillations in cantilevered support structures. The dynamic properties of the structure or the aerodynamic properties of the attachments can be adequately altered to mitigate galloping. The installation of a device providing positive aerodynamic damping can be used to alter the structure's response from the aerodynamic effects on the attachments.

A method of providing positive aerodynamic damping to a traffic signal structure involves installing a sign blank mounted horizontally and directly above the traffic signal attachment closest to the tip of the mast arm. This method has been shown to be effective in mitigating galloping-induced vibrations on traffic signal support structures with horizontally mounted traffic signal attachments (McDonald et al., 1995). For vertically mounted traffic signal attachments, a sign blank mounted horizontally near the tip of the mast arm has mitigated large-amplitude galloping vibrations occurring in traffic signal support structures. This sign blank is placed adjacent to a traffic signal attachment, and a separation exists between the sign blank and the top of the mast arm. In both cases, the sign blanks are required to provide a sufficient surface area for mitigation to occur. However, the installation of sign blanks may influence the design of structures for truck-induced wind gusts by increasing the projected area on a horizontal plane. NCHRP Reports 412 and 469 provide additional discussion on this possible mitigation device and on galloping susceptibility and mitigation.

11.7.1.2—Vortex Shedding

Cantilevered lighting structures shall be designed to resist vortex shedding-induced loads for critical wind velocities less than approximately 20 m/s (45 mph).

The critical wind velocity, V_c (m/s, mph), at which vortex shedding lock-in can occur may be calculated as follows:

For circular sections:

$$V_c = \frac{f_n d}{S_n} \quad \text{(m/s)} \qquad (11\text{-}2)$$

$$V_c = 0.68\frac{f_n d}{S_n} \quad \text{(mph)}$$

For multisided sections:

$$V_c = \frac{f_n b}{S_n} \quad \text{(m/s)} \qquad (11\text{-}3)$$

$$V_c = 0.68\frac{f_n b}{S_n} \quad \text{(mph)}$$

where f_n is a natural frequency of the structure (cps); d and b are the diameter and flat-to-flat width of the horizontal mast arm or pole shaft for circular and multisided sections (m, ft), respectively; and S_n is the Strouhal number. The Strouhal number shall be taken as *0.18* for circular sections, *0.15* for multisided sections, and *0.11* for square or rectangular sections. For a tapered pole, d and b are the average diameter and width.

The equivalent static pressure range to be used for the design of vortex shedding-induced loads shall be:

$$P_{vs} = \frac{0.613 V_c^2 C_d I_F}{2\beta} \quad \text{(Pa)} \qquad (11\text{-}4)$$

$$P_{vs} = \frac{0.00256 V_c^2 C_d I_F}{2\beta} \quad \text{(psf)}$$

where V_c is expressed in m/s (mph); C_d is the drag coefficient as specified in Section 3, "Loads," which is based on the critical wind velocity V_c; and β is the damping ratio, which may be estimated as 0.005.

The equivalent static pressure range P_{vs} shall be applied transversely to poles (i.e., horizontal direction) and horizontal mast arms (i.e., vertical direction).

In lieu of designing to resist periodic vortex-shedding forces, effective vibration mitigation devices may be used.

C11.7.1.2

The shedding of vortices on alternate sides of a member may result in oscillations in a plane normal to the direction of wind flow. Typical natural frequencies and member dimensions preclude the possibility of most cantilevered sign and traffic signal support structures from being susceptible to vortex shedding-induced vibrations.

NCHRP Report 469 shows that poles with tapers exceeding 0.0117 m/m (0.14 in./ft) can also experience vortex shedding in lighting structures. Observations and studies indicate that tapered poles can experience vortex shedding in second or third mode vibrations and that those vibrations can lead to fatigue problems. Procedures to consider higher mode vortex shedding on tapered poles are demonstrated in NCHRP Report 469.

Structural elements exposed to steady, uniform wind flows shed vortices in the wake behind the element in a pattern commonly referred to as a von Karmen vortex street. When the frequency of vortex shedding approaches one of the natural frequencies of the structure, usually the first mode (or higher modes as demonstrated in NCHRP Report 469), significant amplitudes of vibration can be caused by a condition termed lock-in. The critical velocity at which lock-in occurs is defined by the Strouhal relationship:

$$V_c = \frac{f_n d}{S_n} \qquad (C11\text{-}1)$$

For the first mode of vibration, a lower bound wind speed can be established for traffic signal and sign structures. Although vortices are shed at low wind velocities for wind speeds less than 5 m/s (16 fps, 11 mph), the vortices do not impart sufficient energy to excite most structures. Typical natural frequencies and member diameters for sign and traffic signal support structures result in critical wind velocities well below the 5 m/s (16 fps, 11 mph) threshold for the occurrence of vortex shedding. Because of extremely low levels of damping, vortex shedding may significantly excite resonant vibration. At wind speeds greater than about 20 m/s (65 fps, 45 mph), enough natural turbulence is generated to disturb the formation of vortices. Because V_c is relatively low, the largest values of C_d for the support may be conservatively used.

Horizontal arms may be susceptible to vortex shedding before sign and signal heads are attached, i.e., during construction. Although possible, tests (Kaczinski et al., 1998; McDonald et al., 1995) have indicated that the occurrence of vortex shedding from attachments to cantilevered sign and traffic signal support structures is not critical. These attachments are more susceptible to galloping-induced vibrations.

Calculation of the first modal frequency for simple pole structures (i.e., without mast arms) can be computed using:

$$f_{n1} = \frac{1.75}{\pi}\sqrt{\frac{EIg}{wL^4}} \quad \text{(C11-2)}$$

(without luminaire mass)

$$f_{n1} = \frac{1.732}{2\pi}\sqrt{\frac{EIg}{WL^3 + 0.236wL^4}} \quad \text{(C11-3)}$$

(with luminaire mass)

where W is the weight of the luminaire (N, k), w is the weight of the pole per unit length (N/mm, k/in.), g is the acceleration of gravity (9810 mm/s^2, 386 in./s^2), L is the length of the pole (mm, in.), and I is the moment of inertia of the pole (mm^4, in.^{4}). For tapered poles, I_{avg} is substituted for I, where:

$$I_{avg} = \frac{I_{top} + I_{bottom}}{2} \quad \text{(C11-4)}$$

I_{top} is the moment of inertia at the tip of the pole and I_{bottom} is the moment of inertia at the bottom of the pole.

The first modal frequency for poles with mast arms, however, is best accomplished by a finite element based modal analysis. The mass of the luminaire/mast arm attachments shall be included in the analysis to determine the first mode of vibration transverse to the wind direction. Poles that may not have the attachments installed immediately shall be designed for this worst-case condition. Because the natural frequency of a structure without an attached mass is typically higher than those with an attachment, the resulting critical wind speed and vortex shedding pressure range are also higher for this situation.

11.7.1.3 ~~11.7.3~~—Natural Wind Gust

Cantilevered and noncantilevered overhead sign and overhead traffic signal ~~and high level lighting~~ supports shall be designed to resist an equivalent static natural wind gust pressure range of:

$$P_{NW} = 250 C_d I_F \quad \text{(Pa)} \qquad \text{(11-5)}$$

$$P_{NW} = 5.2 C_d I_F \quad \text{(psf)}$$

where C_d is the appropriate drag coefficient based on the yearly mean wind velocity of 5 m/s (11.2 mph) specified in Section 3, "Loads," for the considered element to which the pressure range is to be applied. If Eq. C11-5 is used in place of Eq. 11-5, C_d may be based on the location-specific yearly mean wind velocity V_{mean}. The natural wind gust pressure range shall be applied in the horizontal direction to the exposed area of all support structure members, signs, traffic signals, and/or miscellaneous attachments. Designs for natural wind gusts shall consider the application of wind gusts for any direction of wind.

The design natural wind gust pressure range is based on a yearly mean wind speed of 5 m/s (11.2 mph). For locations with more detailed wind records, particularly sites with higher wind speeds, the natural wind gust pressure may be modified at the discretion of the Owner.

C11.7.1.3 ~~11.7.3~~

Because of the inherent variability in the velocity and direction, natural wind gusts are the most basic wind phenomena that may induce vibrations in wind-loaded structures. The equivalent static natural wind gust pressure range specified for design was developed with data obtained from an analytical study of the response of cantilevered support structures subject to random gust loads (Kaczinski et al., 1998).

Because V_{mean} is relatively low, the largest values of C_d for the support may be conservatively used.

This parametric study was based on the 0.01 percent exceedance for a yearly mean wind velocity of 5 m/s (11.2 mph), which is a reasonable upper bound of yearly mean wind velocities for most locations in the country. There are locations, however, where the yearly mean wind velocity is larger than 5 m/s (11.2 mph). For installation sites with more detailed information regarding yearly mean wind speeds (particularly sites with higher wind speeds), the following equivalent static natural wind gust pressure range may ~~shall~~ be used for design:

$$P_{NW} = 250 C_d \left(\frac{V_{mean}}{5 m/s} \right)^2 I_F \quad \text{(Pa)} \qquad \text{(C11-5)}$$

$$P_{NW} = 5.2 C_d \left(\frac{V_{mean}}{11.2 mph} \right)^2 I_F \quad \text{(psf)}$$

The largest natural wind gust loading for an arm or pole with a single arm is from a wind gust direction perpendicular to the arm. For a pole with multiple arms, such as two perpendicular arms, the critical direction for the natural wind gust is usually not normal to either arm. The design natural wind gust pressure range shall be applied to the exposed surface areas seen in an elevation view orientated perpendicular to the assumed wind gust direction.

11.7.1.4 ~~11.7.4~~—Truck-Induced Gust

Cantilevered and noncantilevered overhead sign and traffic signal support structures shall be designed to resist an equivalent static truck gust pressure range of

$$P_{TG} = 900 C_d I_F \quad \text{(Pa)} \qquad \text{(11-6)}$$
$$P_{TG} = 18.8 C_d I_F \quad \text{(psf)}$$

where C_d is the drag coefficient based on the truck speed of 30 m/s (65 mph) from Section 3, "Loads," for the considered element to which the pressure range is to be applied. If Eq. C11-6 is used in place of Eq. 11-6, C_d should be based on the considered truck speed V_T. The pressure range shall be applied in the vertical direction to the horizontal support as well as the area of all signs, attachments, walkways, and/or lighting fixtures projected on a horizontal plane. This pressure range shall be applied along any 3.7-m (12-ft) length to create the maximum stress range, excluding any portion of the structure not located directly above a traffic lane. The equivalent static truck pressure range may be reduced for locations where vehicle speeds are less than 30 m/s (65 mph).

The magnitude of applied pressure range may be varied depending on the height of the horizontal support and the attachments above the traffic lane. Full pressure shall be applied for heights up to and including 6 m (20 ft), and then the pressure may be linearly reduced for heights above 6 m (20 ft) to a value of zero at 10 m (33 ft).

The truck-induced gust loading shall be excluded unless required by the Owner for the fatigue design of overhead traffic signal support structures.

C11.7.1.4 ~~11.7.4~~

The passage of trucks beneath support structures may induce gust loads on the attachments mounted to the horizontal support of these structures. Although loads are applied in both horizontal and vertical directions, horizontal support vibrations caused by forces in the vertical direction are most critical. Therefore, truck gust pressures are applied only to the exposed horizontal surface of the attachment and horizontal support.

A pole with multiple horizontal cantilever arms may be designed for truck gust loads applied separately to each individual arm and need not consider truck gust loads applied simultaneously to multiple arms.

Recent vibration problems on sign structures with large projected areas in the horizontal plane, such as variable message sign (VMS) enclosures, have focused attention on vertical gust pressures created by the passage of trucks beneath the sign.

The design pressure calculated from Eq. 11-6 is based on a truck speed of 30 m/s (65 mph). For structures installed at locations where the posted speed limit is much less than 30 m/s (65 mph), the design pressure may be recalculated based on this lower truck speed. The following equation may be used:

$$P_{TG} = 900 C_d \left(\frac{V_T}{30 \frac{m}{s}} \right)^2 I_F \quad \text{(Pa)} \qquad \text{(C11-6)}$$

$$P_{TG} = 18.8 C_d \left(\frac{V_T}{65 mph} \right)^2 I_F \quad \text{(psf)}$$

where V_T is the truck speed in m/s (mph).

The given truck-induced gust loading shall be excluded unless required by the Owner for the fatigue design of overhead traffic signal structures. Many traffic signal structures are installed on roadways with negligible truck traffic. In addition, the typical response of traffic signal structures from truck-induced gusts is significantly overestimated by the design pressures prescribed in this article (NCHRP Report 469). This has been confirmed in a recent study (Albert et al, 2007) involving full-scale field tests where strains were monitored on cantilevered traffic signal structures. Over 400 truck events were recorded covering a variety of truck types and vehicle speeds; only 18 trucks produced even a detectable effect on the cantilevered traffic signal structures and the strains were very small relative to those associated with the design pressures in this Article.

11.7.2—High-mast Lighting Towers

High-mast lighting towers shall be designed for fatigue to resist the combined wind effect, an equivalent static pressure range of

$$P_{CW} = P_{FLS} C_d \qquad (11\text{-}7)$$

where P_{FLS} is the fatigue-limit-state static pressure range presented in Table 11-3. For the structural element considered, C_d is the appropriate drag coefficient specified in Section 3, "Loads," and shall be based on the yearly mean wind velocity, V_{mean}. The combined wind effect pressure range shall be applied in the horizontal direction to the exposed area of all high-mast lighting tower components. Designs for combined wind shall consider the application of wind from any direction.

The yearly mean wind velocity used in determining P_{FLS} shall be as given in Figure 11-1. Designers are cautioned of the effects of topography when considering location-specific mean wind velocity in their design. These effects can cause considerable variation in wind speed. For locations with more detailed wind records, the yearly mean wind velocity may be modified at the discretion of the Owner.

C11.7.2

NCHRP Project 10-74 is the basis for fatigue loads identified in this section. Prior to 2012, these AASHTO specifications made no distinction between high-mast lighting towers and other signal, sign, or luminaire support structures. Failures of HMLTs resulting from wind-induced fatigue led to field testing, laboratory wind tunnel testing, and analytical studies to determine appropriate load models for the fatigue design of high-mast lighting towers.

The fatigue-limit-state static pressure range values listed in Table 11-3 account for fatigue importance factors and variation in mean wind speed. The combined wind pressure range includes the cumulative fatigue damage effects of vortex shedding.

Figure 11-1 serves as a broad guide for determining regional mean wind speed. Local conditions are known to vary and may not necessarily be represented by the map. NCHRP Report 412 and NCHRP 10-74 found the design method to be conservative in most cases; however, designers are encouraged to check local wind records and/or consider topographical effects in choosing a yearly mean wind speed for design if the local wind conditions are suspected to be more severe than suggested by Figure 11-1.

Table 11-3–Fatigue-limit-state Pressure Range for HMLT Design, P_{FLS}

Yearly Mean Wind Velocity, V_{mean}	Importance Category	
	I	II
$V_{mean} \leq 9$ mph	310 Pa (6.5 psf)	280 Pa (5.8 psf)
9 mph $< V_{mean} \leq$ 11 mph	310 Pa (6.5 psf)	310 Pa (6.5 psf)
$V_{mean} >$ 11 mph	340 Pa (7.2 psf)	340 Pa (7.2 psf)

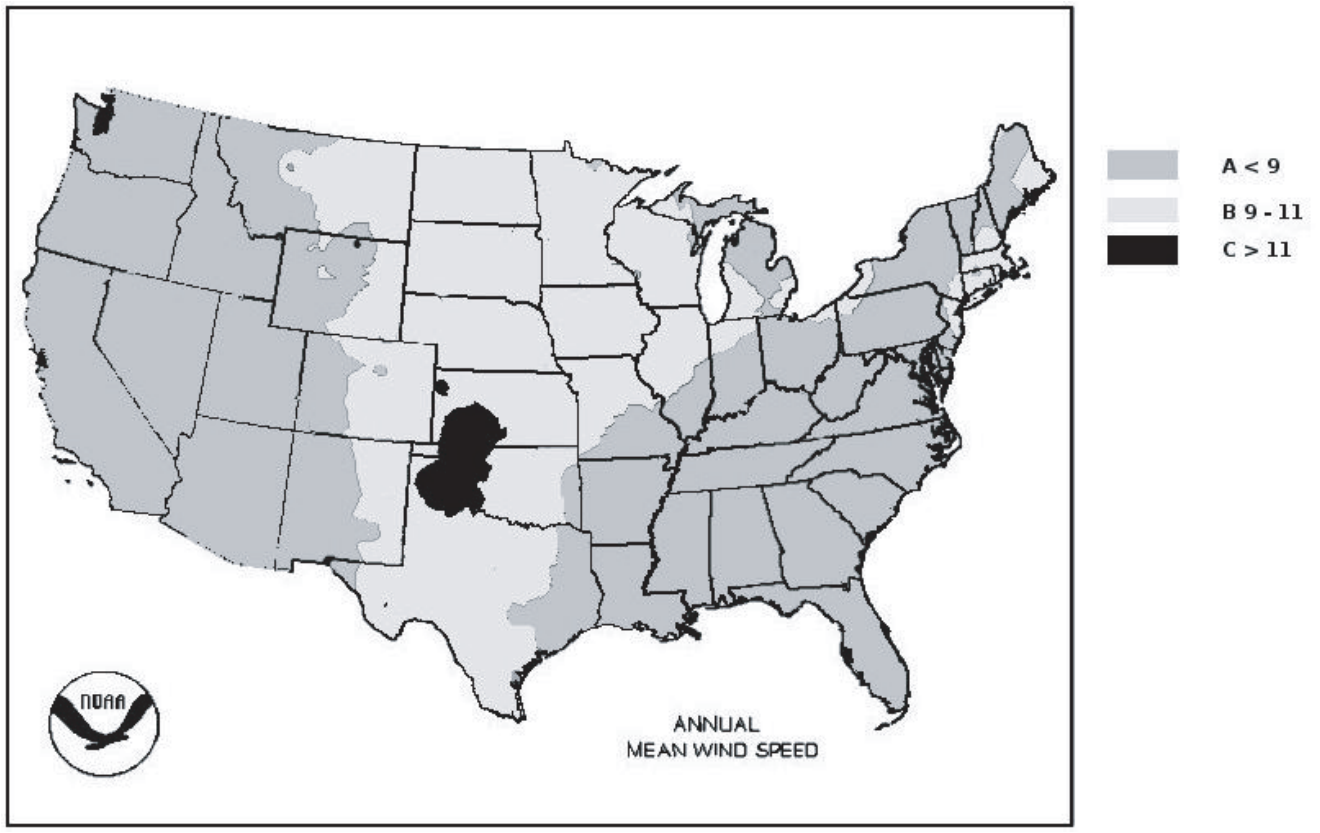

Figure 11-1—Yearly Mean Wind Velocity, mph

No separate load is specified to account for vortex shedding since it is incorporated in the combined wind pressure range for HMLTs, P_{CW} used for fatigue design in Article 11.7.2.

Where serviceability and maintenance requirements due to vortex shedding induced vibrations are an issue, devices such as strakes, shrouds, mechanical dampers, etc. may be used to mitigate the effect.

High-mast lighting towers can be highly susceptible to vibrations induced by vortex shedding, leading to the rapid accumulation of damaging stress cycles (depending on the fatigue detail category selected) that lead to fatigue failure. Prior to 2012, HMLTs were included in Section 11.7.1.2. NCHRP Project 10-74 studied the response of these structures in the field and determined that the previous edition did not properly quantify vortex shedding. Rather than separate the effect of vortex shedding from all other wind phenomena, a loading spectrum was developed to encompass all typical wind load effects. The fatigue-limit-state static wind pressures listed in Table 11-3 represent this combined wind load effect.

Maintenance and serviceability issues resulting from vortex shedding may have a detrimental effect of the performance of HMLTs. Issues with anchor bolts loosening and rattling of the luminaire have been known to occur. Where fatigue-prone details exist, which may shorten the life of HMLTs due to a lower fatigue resistance than initially considered, or in cases where an HMLT initially designed for a finite lifetime may wish to be extended, mitigation devices have proved reliable in reducing the number of damaging stress cycles. Information pertaining to the performance and sizing of strakes and shrouds on HMLTs is presented in NCHRP Report 10-74 and *Reduction of Wind-Induced Vibrations in High-mast Light Poles* (Ahearn and Puckett).

11.8—DEFLECTION

Galloping and truck-gust-induced vertical deflections of cantilevered single-arm sign supports and traffic signal arms and noncantilevered supports should not be excessive so as to result in a serviceability problem, because motorists cannot clearly see the attachments or are concerned about passing under the structures.

C11.8

Because of the low levels of stiffness and damping inherent in cantilevered single mast arm sign and traffic signal support structures, even structures that are adequately designed to resist fatigue damage may experience excessive vertical deflections at the free end of the horizontal mast arm. The primary objective of this provision is to minimize the number of motorist complaints.

NCHRP Report 412 recommends that the total deflection at the free end of single-arm sign supports and all traffic signal arms be limited to 200 mm (8 in.) vertically, when the equivalent static design wind effect from galloping and truck-induced gusts are applied to the structure. NCHRP Report 494 recommends applying the 200-mm (8-in.) vertical limit to noncantilevered support structures. Double-member or truss-type cantilevered horizontal sign supports were not required to have vertical deflections checked because of their inherent stiffness. There are no provisions for a displacement limitation in the horizontal direction.

11.9—FATIGUE RESISTANCE

The allowable CAFLs are provided in ~~Table 11-3~~ Table 11-5. A summary of the typical fatigue-sensitive connection details are presented in ~~Table 11-2~~ Table 11-4 and illustrated in Figure ~~11-1~~11-2. Wind loads of Article 11.7 shall be considered in computing the fatigue stress range.

Unless noted in ~~Table 11-2~~ Table 11-4, the member cross-section adjacent to the weld toe shall be used to compute the nominal stress range.

C11.9

The CAFLs were established based on fatigue testing and the resistances were computed based on elastic section analysis, i.e., nominal values in the cross-section. Therefore, it is assumed that these resistances include effects of residual stresses due to fabrication, out-of-plane distortions, etc. At this time, only stress range due to wind is used; therefore, dead load effects may be neglected.

Residual stresses and anchor bolt pretension are generally not considered in the computations.

~~Table 11-2~~ Table 11-4—Fatigue Details of Cantilevered and Noncantilevered Support Structures

Construction	Detail	Stress Category	Application	Example
Plain Members	1. With rolled or cleaned surfaces. Flame-cut edges with ANSI/AASHTO/AWS D5.1 (Article 3.2.2) smoothness of 1000 μ-in. or less.	*A*	—	—
	2. Slip-joint splice where *L* is greater than or equal to 1.5 diameters.	*B*	High-level lighting poles.	1
Mechanically Fastened Connections	3. Net section of fully tightened, high-strength (ASTM A 325, A 490) bolted connections.	*B*	Bolted joints.	2
	4. Net section of other mechanically fastened connections: a. Steel: b. Aluminum:	 *D* *E*	—	3
	5. Anchor bolts or other fasteners in tension; stress range based on the tensile stress area. Misalignments of less than 1:40 with firm contact existing between anchor bolt nuts, washers, and base plate.	*D*	Anchor bolts. Bolted mast-arm-to-column connections.	8, 16
	6. Connection of members or attachment of miscellaneous signs, traffic signals, etc. with clamps or U-bolts.	*D*	—	—
Holes and Cutouts	7. Net section of holes and cutouts.	*D*	Wire outlet holes. Drainage holes. Unreinforced handholes.	5
Groove Welded Connections	8. Tubes with continuous full- or partial-penetration groove welds parallel to the direction of the applied stress.	*B′*	Longitudinal seam welds.	6
	9. Full-penetration groove-welded splices with welds ground to provide a smooth transition between members (with or without backing ring removed).	*D*	Column or mast arm butt-splices.	4
	10. Full-penetration groove-welded splices with weld reinforcement not removed (with or without backing ring removed).	*E*	Column or mast arm butt-splices.	4
	11. Full-penetration groove-welded tube-to-transverse plate connections with the backing ring attached to the plate with a full-penetration weld, or with a continuous fillet weld around interior face of backing ring. The thickness of the backing ring shall not exceed 10 mm (0.375 in.) when a fillet weld attachment to plate is used. Full-penetration groove-welded tube-to-transverse plate connections welded from both sides with backgouging (without backing ring).	*E*	Column-to-base-plate connections. Mast-arm-to-flange-plate connections.	5
	12. Full-penetration groove-welded tube-to-	*E′*	Column-to-base-plate	5

Continued on next page

Construction	Detail	Stress Category	Application	Example
	transverse plate connections with the backing ring not attached to the plate with a continuous full-penetration weld, or with a continuous interior fillet weld.		connections. Mast-arm-to-flange-plate connections.	
Fillet-Welded Connections	13. Fillet-welded lap splices.	*E*	Column or mast arm lap splices.	3
	14. Members with axial and bending loads with fillet-welded end connections without notches perpendicular to the applied stress. Welds distributed around the axis of the member so as to balance weld stresses.	*E*	Angle-to-gusset connections with welds terminated short of plate edge. Slotted tube-to-gusset connections with coped holes.[e]	2, 6
	15. Members with axial and bending loads with fillet-welded end connections with notches perpendicular to the applied stress. Welds distributed around the axis of the member so as to balance weld stresses.	*E′*	Angle-to-gusset connections. Slotted tube-to-gusset connections without coped holes.	2, 6
	16. Fillet-welded tube-to-transverse plate connections. [j]	*E′*	Column-to-base-plate or mast-arm-to-flange-plate socket connections.	7, 8, 16
	17. Fillet-welded connections with one-sided welds normal to the direction of the applied stress.	*E′*	Built-up box mast-arm-to-column connections.	8, 16
	18. Fillet-welded mast-arm-to-column pass-through connections.	*E′* [f]	Mast-arm-to-column pass-through connections.	9
	19. Fillet-welded T-, Y-, and K-tube-to-tube, angle-to-tube, or plate-to-tube connections.	[a, b]	Chord-to-vertical or chord-to-diagonal truss connections.[a] Mast-arm directly welded to column. [b] Built-up box connection.[b]	8, 10, 11
	25. Fillet-welded ring-stiffened box-to-tube connection.	[g]	Ring-stiffened built-up box connections.	16
Attachments	20. Longitudinal attachments with partial- or full-penetration groove welds, or fillet welds, in which the main member is subjected to longitudinal loading: $L < 51$ mm (2 in.): 51 mm (2 in.) $\leq L \leq 12t$ and 102 mm (4 in.): $L > 12t$ or 102 mm (4 in.) when $t \leq 25$ mm (1 in.):	 *C* *D* *E*	Reinforcement at handholes.	13
	21. Longitudinal attachments with partial- or full-penetration groove welds, or fillet welds in which the main member is subjected to longitudinal loading.	*E′*	Weld terminations at ends of longitudinal stiffeners. [h, i]	12, 14
	22. Detail 22 has been intentionally removed.			
	23. Transverse load-bearing fillet-welded attachments where $t \leq 13$ mm (0.5 in.) and the main member is subjected to minimal axial and/or flexural loads. (When $t > 13$ mm	*C*	Longitudinal stiffeners welded to base plates.	12, 14

Continued on next page

Construction	Detail	Stress Category	Application	Example
	[0.5 in.], see note d.)			
	24. Transverse load-bearing longitudinal attachments with partial- or full-penetration groove welds or fillet welds, in which the nontubular main member is subjected to longitudinal loading and the weld termination embodies a transition radius that is ground smooth:		Gusset-plate-to-chord attachments.	15
	$R > 51\ \text{mm}\ (2\ \text{in.})$	D		
	$R \le 51\ \text{mm}\ (2\ \text{in.})$	E [c]		

Notes:

[a] Stress Category *ET* with respect to stress in branching member provided that $r/t \le 24$ for the chord member. When $r/t > 24$, then the fatigue strength equals:

$$(F)_n = (\Delta F)_n^{ET} \times \left(\frac{24}{\frac{r}{t}} \right)^{0.7}$$

where:

$(\Delta F)_n^{ET}$

is the CAFL for Category *ET*.
Stress Category E with respect to stress in chord.

[b] Stress Category *ET* with respect to stress in branching member.
Stress Category K_2 with respect to stress in main member (column) provided that: $r/t_c \le 24$ for the main member.
When $r/t_c > 24$, then the fatigue strength equals:

$$(F)_n = (\Delta F)_n^{K_2} \times \left(\frac{24}{\frac{r}{t_c}} \right)^{0.7}$$

where:

$(\Delta F)_n^{K_2}$

is the CAFL for Category K_2.

The nominal stress range in the main member equals $(S_R)_{\text{main member}} = (S_R)_{\text{branching member}} (t_b/t_c)\ \alpha$
where t_b is the wall thickness of the branching member, t_c is the wall thickness of the main member (column), and α is the ovalizing parameter for the main member equal to 0.67 for in-plane bending and equal to 1.5 for out-of-plane bending in the main member. $(S_R)_{\text{branching member}}$ is the calculated nominal stress range in the branching member induced by fatigue design loads. (See commentary of Article 11.5.)

The main member shall also be designed for Stress Category E using the elastic section of the main member and moment just below the connection of the branching member.

[c] First check with respect to the longitudinal stress range in the main member per the requirements for longitudinal attachments. The attachment must then be separately checked with respect to the transverse stress range in the attachment per the requirements for transverse load-bearing longitudinal attachments.

[d] When $t > 13\ mm$ (0.5 in.), the fatigue strength shall be the lesser of Category C or the following:

$$(\Delta F) = (\Delta F)_n^c \times \left(\frac{0.094 + 1.23\frac{H}{t_p}}{t_p^{\frac{1}{6}}} \right) (\text{MPa}) \qquad (\Delta F) = (\Delta F)_n^c \times \left(\frac{0.0055 + 0.72\frac{H}{t_p}}{t_p^{\frac{1}{6}}} \right) (\text{ksi})$$

where $(\Delta F)_n^c$

is the CAFL for Category *C*, *H* is the effective weld throat (mm, in.), and t_p is the attachment plate thickness (mm, in.).

e The diameter of coped holes shall be the greater of 25 mm (1 in.), twice the gusset plate thickness, or twice the tube thickness.

f In addition to checking the branching member (mast arm), the main member (column) shall be designed for Stress Category E using the elastic section of the main member and moment just below the connection of the branching member (mast arm).

g Stress Category *E′* with respect to stress in branching member (ring-stiffened built-up box connection). The main member shall be designed for Stress Category E using the elastic section of the main member and moment just below the connection of the branching member.

h Only longitudinal stiffeners with lengths greater than 102 mm (4 in.) are applicable for Detail 21. On column-to-base-plate or mast-arm-to-flange plate socket connections having a wall thickness greater than 6 mm (0.25 in.) that have exhibited satisfactory field performance, the use of stiffeners having a transition radius or taper with the weld termination ground smooth may be designed at a higher stress category with the approval of the Owner. Under this exception, the Owner shall establish the stress category to which the detail shall be designed. See commentary for Article 11.5.

i Nondestructive weld inspection should be used in the vicinity of the weld termination of longitudinal stiffeners. Grinding of weld terminations to a smooth transition with the tube face is not allowed in areas with fillet welds or partial-penetration welds connecting the stiffener to the tube. Full-penetration welds shall be used in areas where grinding may occur. See commentary for Article 11.5.

j Fillet welds for socket connections (Detail 16) shall be unequal leg welds, with the long leg of the fillet weld along the column or mast arm. The termination of the longer weld leg should contact the shaft's surface at approximately a 30º angle.

~~Table 11-3~~ Table 11-5—Constant-Amplitude Fatigue Limits

Detail Category	Steel		Aluminum	
	MPa	ksi	MPa	ksi
A	165	24	70	10.2
B	110	16	41	6.0
B′	83	12	32	4.6
C	69	10	28	4.0
D	48	7	17	2.5
E	31	4.5	13	1.9
E′	18	2.6	7	1.0
ET	8	1.2	3	0.44
K_2	7	1.0	2.7	0.38

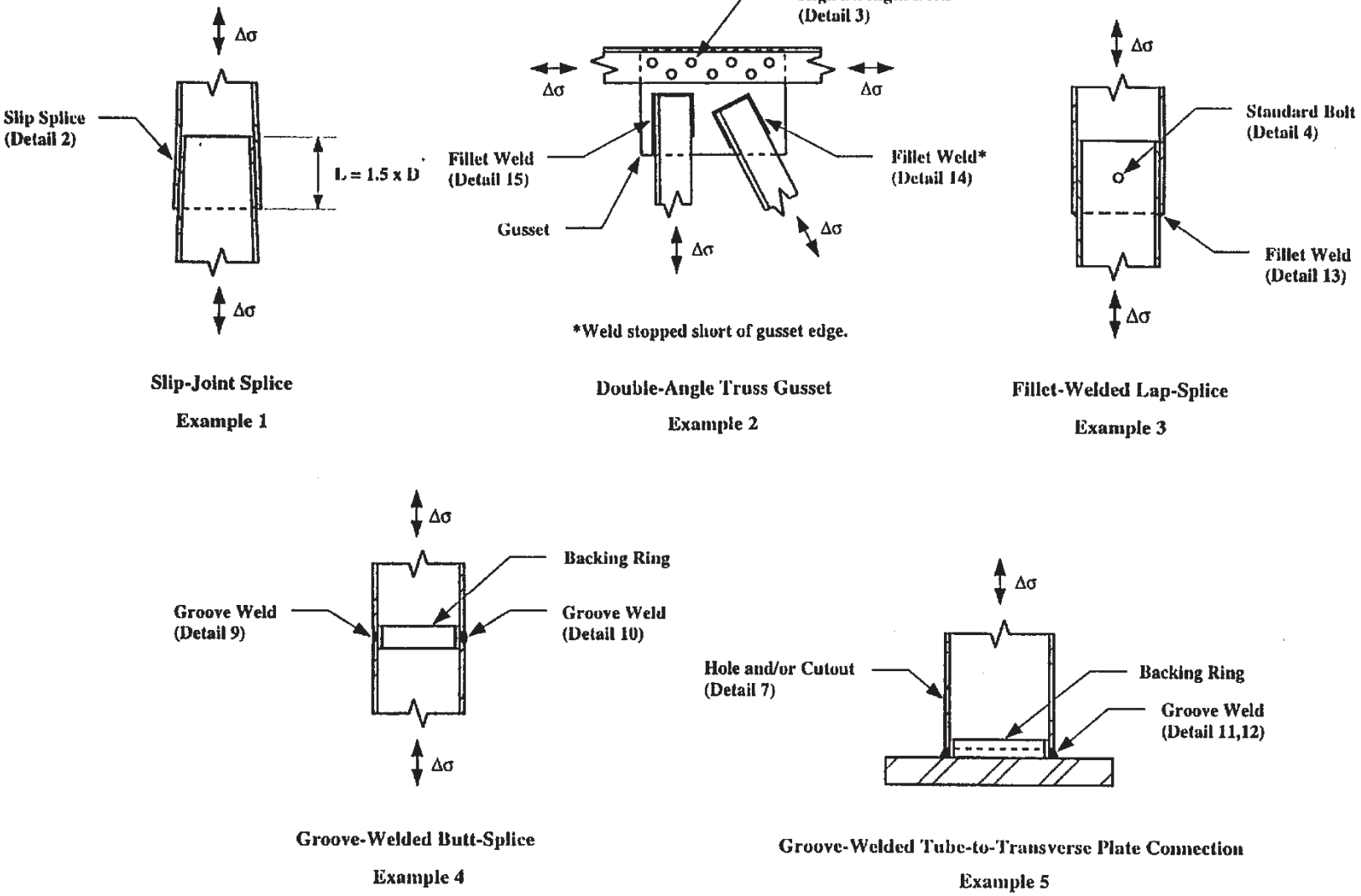

Continued on next page

Figure ~~11-1~~ 11-2—Illustrative Examples

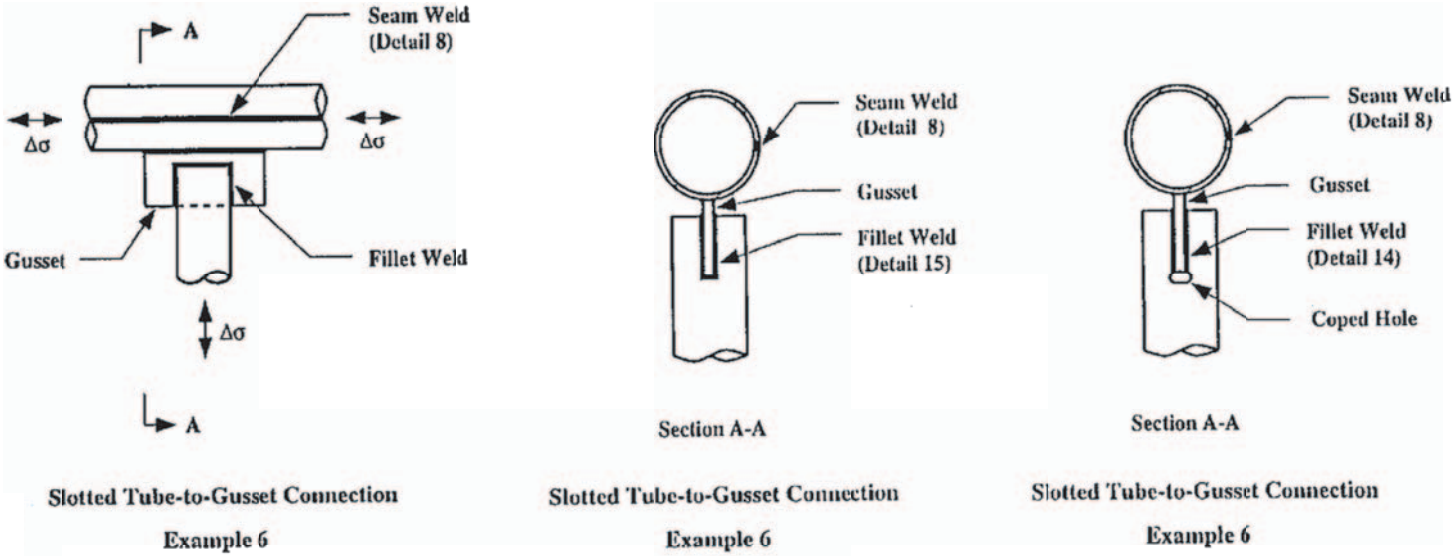

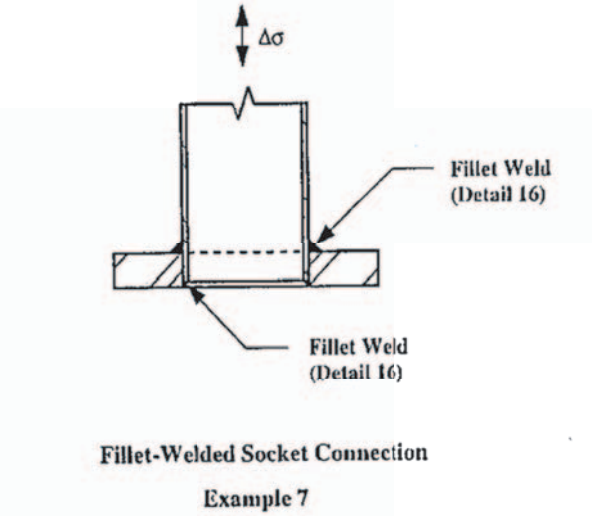

Continued on next page

Figure ~~11-1~~11-2—Illustr ative Examples— *Continued*

Fatigue Loading and Design Methodology for High-Mast Lighting Towers

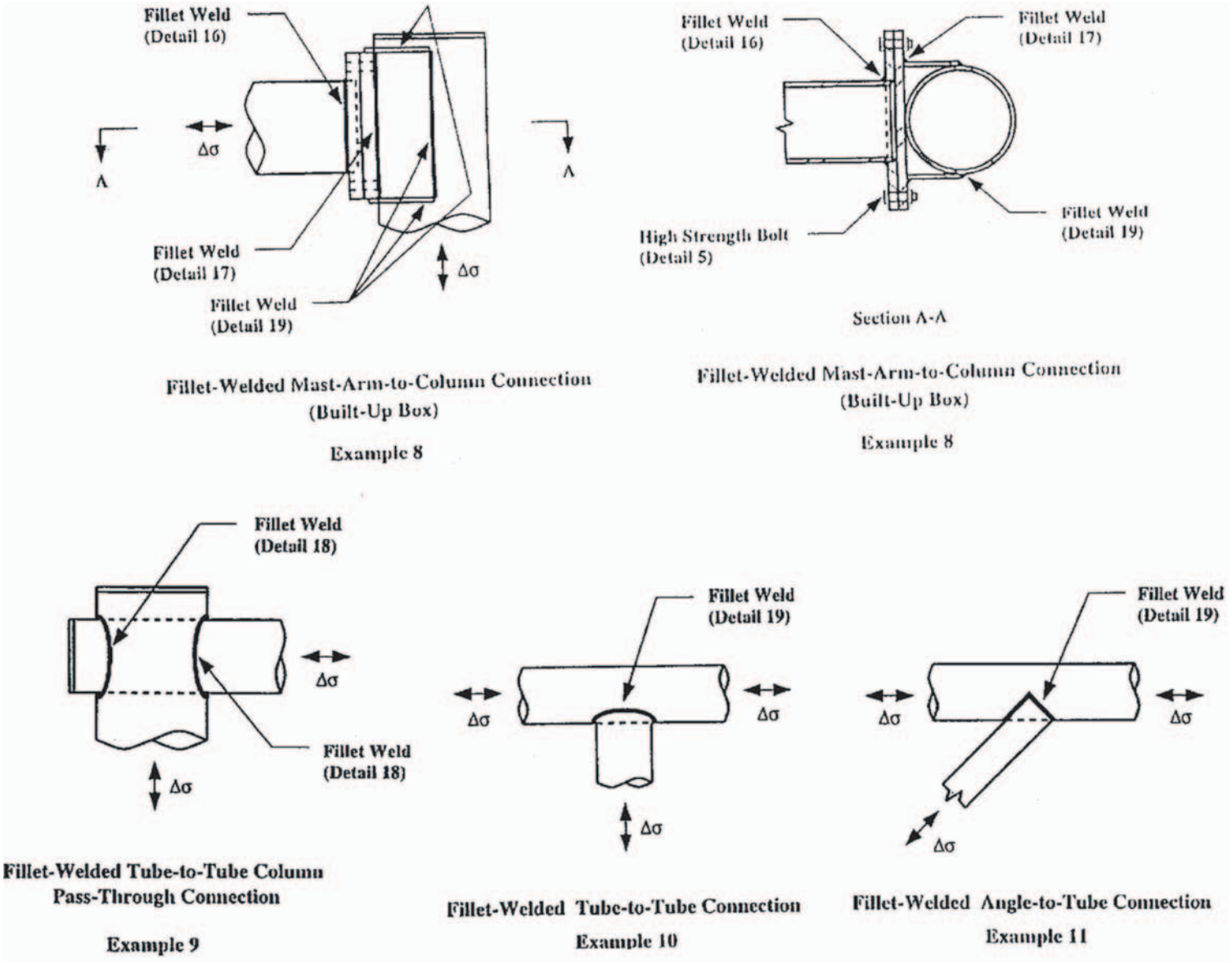

Continued on next page

Figure ~~11-1~~11-2—Illustrative Examples—*Continued*

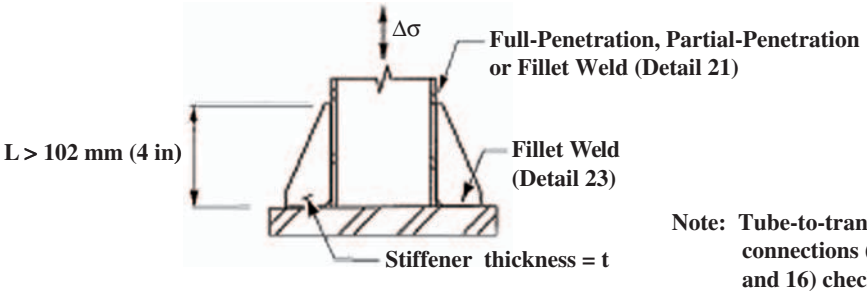

Longitudinal Attachment
Example 12

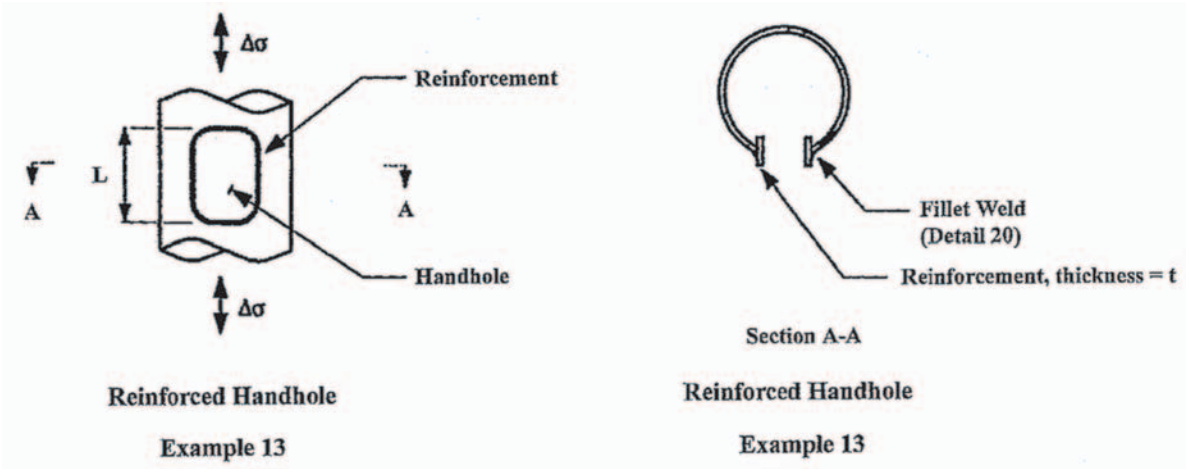

Reinforced Handhole
Example 13

Reinforced Handhole
Example 13

Continued on next page

Figure ~~11-1~~11-2—Illustrative Examples—*Continued*

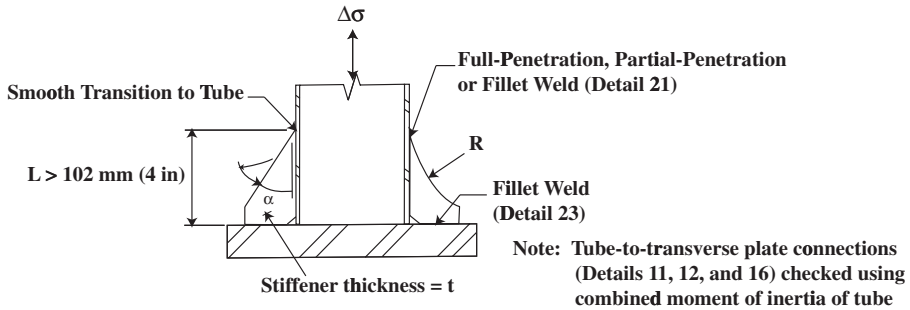

Longitudinal Attachment

Example 14

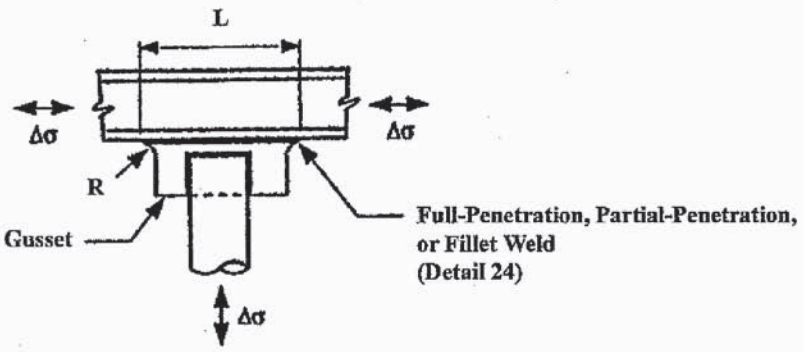

Transverse Load-Bearing Longitudinal Attachment

Example 15

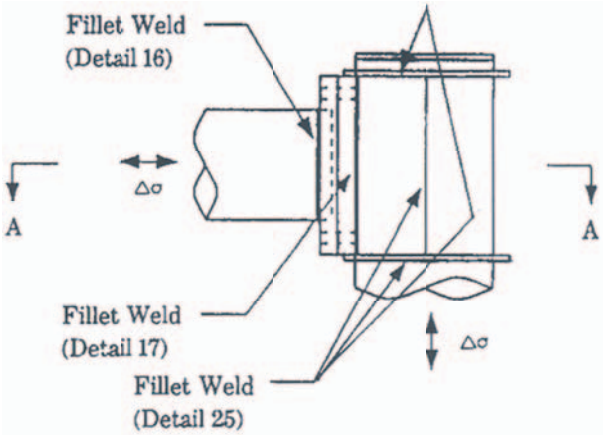

Fillet–Welded Mast–Arm–to–Column Connection
(Ring–Stiffened Built–Up Box)

Example 16

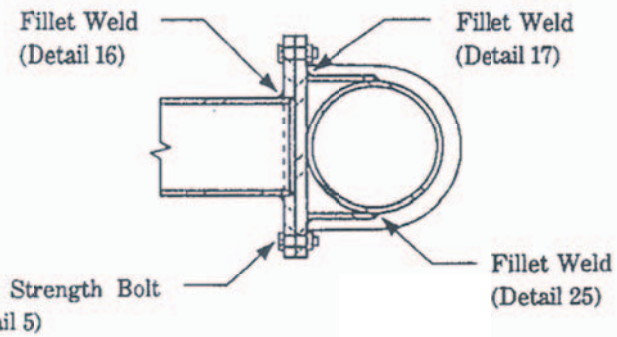

Section A–A

Fillet–Welded Mast–Arm–to–Column Connection
(Ring–Stiffened Built–Up Box)

Example 16

Figure ~~11-1~~11-2—Illustrative Examples—*Continued*

11.10—REFERENCES

AASHTO. 2002. *AASHTO Standard Specifications for Highway Bridges*, 17th Edition, HB-17. American Association of State Highway and Transportation Officials, Washington, DC.

Ahearn, E.B., and J.A. Puckett. 2010. "Reduction of Wind-Induced Vibrations in High-mast Light Poles," Report No. FHWA-WY-10/02F, University of Wyoming, Laramie, WY.

Albert M. N., L. Manuel, K. H. Frank, and S. L. Wood. 2007. *Field Testing of Cantilevered Traffic Signal Structures under Truck-Induced Gust Loads*, Report No. FHWA/TX-07/4586-2. Center for Transportation Research, Texas Department of Transportation, Austin, Texas.

Amir, G., and A. Whittaker. 2000. "Fatigue-Life Evaluation of Steel Post Structures II: Experimentation," *Journal of Structural Engineering*. American Society of Civil Engineers, New York, NY. Vol. 126, No. 3, Vol. 2 (March 2000), pp. 331–340.

Connor, R.J., S.H. Collicott, A.M. DeSchepper, R.J. Sherman, and J.A. Ocampo. "Development of Fatigue Loading and Design Methodology for High-Mast Lighting Towers," NCHRP Project 10-74. Purdue University, West Lafayette, IN (2011).

Cook, R. A., D. Bloomquist, A. M. Agosta, and K. F. Taylor. 1996. *Wind Load Data for Variable Message Signs*, Report No. FL/DOT/RMC/0728-9488. University of Florida, Gainesville, FL. Report prepared for Florida Department of Transportation.

Creamer, B. M., K. G. Frank, and R. E. Klingner. 1979. *Fatigue Loading of Cantilever Sign Structures from Truck Wind Gusts*, Report No. FHWA/TX-79/10+209-1F. Center for Highway Research, Texas State Department of Highways and Public Transportation, Austin, TX.

Dexter, R. J., and K. W. Johns. 1998. *Fatigue-Related Wind Loads on Highway Support Structures: Advanced Technology for Large Structural Systems*, Report No. 98-03. Lehigh University, Bethlehem, PA.

Dexter, R., and M. Ricker. 2002. *Fatigue-Resistant Design of Cantilever Signal, Sign, and Light Supports*, NCHRP Report 469. Transportation Research Board, National Research Council, Washington DC.

Fisher, J. W., A. Nussbaumer, P. B. Keating, and B. T. Yen. 1993. *Resistance of Welded Details Under Variable Amplitude Long-Life Fatigue Loading*, NCHRP Report 354. Transportation Research Board, National Research Council, Washington, DC.

Florea M. J., L. Manuel, K. H. Frank, and S. L. Wood. 2007. *Field Tests and Analytical Studies of the Dynamic Behavior and the Onset of Galloping in Traffic Signal Structures*, Report No. FHWA/TX-07/4586-1. Center for Transportation Research, Texas Department of Transportation, Austin, Texas.

Fouad, F., et al. 2003. *Structural Supports for Highway Signs, Luminaries, and Traffic Signals*, NCHRP Report 494. Transportation Research Board, National Research Council, Washington, DC.

Kaczinski, M. R., R. J. Dexter, and J. P. Van Dien. 1998. *Fatigue Resistant Design of Cantilevered Signal, Sign and Light Supports*, NCHRP Report 412. Transportation Research Board, National Research Council, Washington, DC.

Koenigs, M. T., T. A. Botros, D. Freytag, and K. H. Frank. 2003. *Fatigue Strength of Signal Mast Arm Connections*, Report No. FHWA/TX-04/4178-2. Center for Transportation Research, Texas Department of Transportation, Austin, TX.

McDonald, J. R., et al. 1995. *Wind Load Effects on Signals, Luminaires and Traffic Signal Structures*, Report No. 1303-1F. Wind Engineering Research Center, Texas Tech University, Lubbock, TX.

NOAA. 2010. "Comparative Climatic Data for the United States Through 2010," National Climatic Data Center, Asheville, NC.

Abbreviations and acronyms used without definitions in TRB publications:

AAAE	American Association of Airport Executives
AASHO	American Association of State Highway Officials
AASHTO	American Association of State Highway and Transportation Officials
ACI–NA	Airports Council International–North America
ACRP	Airport Cooperative Research Program
ADA	Americans with Disabilities Act
APTA	American Public Transportation Association
ASCE	American Society of Civil Engineers
ASME	American Society of Mechanical Engineers
ASTM	American Society for Testing and Materials
ATA	American Trucking Associations
CTAA	Community Transportation Association of America
CTBSSP	Commercial Truck and Bus Safety Synthesis Program
DHS	Department of Homeland Security
DOE	Department of Energy
EPA	Environmental Protection Agency
FAA	Federal Aviation Administration
FHWA	Federal Highway Administration
FMCSA	Federal Motor Carrier Safety Administration
FRA	Federal Railroad Administration
FTA	Federal Transit Administration
HMCRP	Hazardous Materials Cooperative Research Program
IEEE	Institute of Electrical and Electronics Engineers
ISTEA	Intermodal Surface Transportation Efficiency Act of 1991
ITE	Institute of Transportation Engineers
NASA	National Aeronautics and Space Administration
NASAO	National Association of State Aviation Officials
NCFRP	National Cooperative Freight Research Program
NCHRP	National Cooperative Highway Research Program
NHTSA	National Highway Traffic Safety Administration
NTSB	National Transportation Safety Board
PHMSA	Pipeline and Hazardous Materials Safety Administration
RITA	Research and Innovative Technology Administration
SAE	Society of Automotive Engineers
SAFETEA-LU	Safe, Accountable, Flexible, Efficient Transportation Equity Act: A Legacy for Users (2005)
TCRP	Transit Cooperative Research Program
TEA-21	Transportation Equity Act for the 21st Century (1998)
TRB	Transportation Research Board
TSA	Transportation Security Administration
U.S.DOT	United States Department of Transportation